Christopher Schierholz

# Rashba Spin-Orbit Interaction in Low and High Magnetic Fields

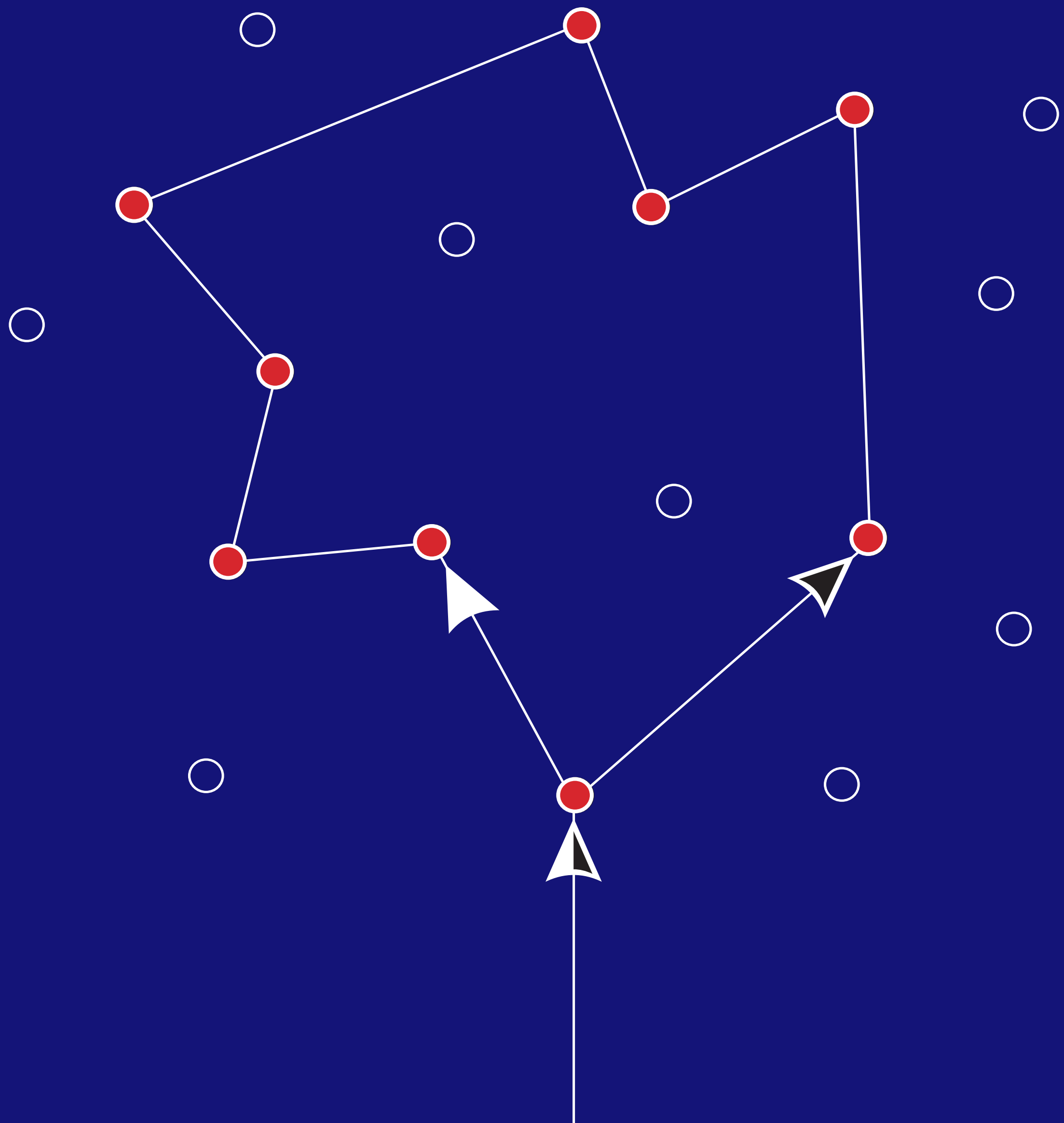

Cuvillier Verlag Göttingen

# Rashba Spin-Orbit Interaction in Low and High Magnetic Fields

Dissertation
zur Erlangung des Doktorgrades
des Fachbereichs Physik
der Universität Hamburg

vorgelegt von
Christopher Schierholz
aus Hamburg

Hamburg
2005

**Bibliografische Information Der Deutschen Bibliothek**
Die Deutsche Bibliothek verzeichnet diese Publikation in der Deutschen Nationalbibliografie; detaillierte bibliografische Daten sind im Internet über http://dnb.ddb.de abrufbar.
1. Aufl. - Göttingen : Cuvillier, 2005
Zugl.: Hamburg, Univ., Diss., 2005
ISBN 3-86537-449-2

| | |
|---|---|
| Gutachter der Dissertation: | Prof. Dr. U. Merkt<br>Prof. Dr. J. Nitta |
| Gutachter der Disputation: | Prof. Dr. U. Merkt<br>Prof. Dr. D. Heitmann |
| Datum der Disputation: | 4. Mai 2005 |
| Vorsitzender des Prüfungsausschusses: | Prof. Dr. H.-P. Oepen |
| Dekan des Fachbereichs Physik und Vorsitzender des Promotionsausschusses: | Prof. Dr. G. Huber |

© CUVILLIER VERLAG, Göttingen 2005
Nonnenstieg 8, 37075 Göttingen
Telefon: 0551-54724-0
Telefax: 0551-54724-21
www.cuvillier.de

Alle Rechte vorbehalten. Ohne ausdrückliche Genehmigung des Verlages ist es nicht gestattet, das Buch oder Teile daraus auf fotomechanischem Weg (Fotokopie, Mikrokopie) zu vervielfältigen.
1. Auflage, 2005
Gedruckt auf säurefreiem Papier

ISBN 3-86537-449-2

# Abstract


Rashba spin-orbit interaction in two-dimensional electron gases (2DEGs) of narrow-gap III-V semiconductors is studied in this thesis. Spin-orbit interaction in such systems is governed by structure inversion asymmetry: both potential gradients across the 2DEG and quantum-well boundaries significantly contribute to spin-orbit interaction, the strength of which is expressed by the Rashba parameter $\alpha$. Three experimental techniques are used to determine the values of $\alpha$: Shubnikov-de Haas (SdH) oscillations in high external magnetic fields, and weak antilocalisation (WAL) as well as Al'tshuler-Aronov-Spivak (AAS) oscillations in near-zero external magnetic fields. Control of $\alpha$ is effected by applied gate voltages.
High-field and low-field magnetotransport experiments are performed on inversion layers of p-type InAs single crystals and on InAs/$In_{0.75}Ga_{0.25}As$ heterostructures. SdH oscillations and WAL are observed for both material systems. The Rashba parameters obtained from the WAL are found to agree qualitatively and quantitatively with $k \cdot p$ theory calculations. The Rashba parameters determined from SdH oscillations in high magnetic fields disagree with those determined by WAL in low magnetic fields. In the inversion layers, the values of $\alpha$ determined by the two techniques are of the same order of magnitude, but the dependence on the carrier density differs: the results from SdH oscillations increase with increasing carrier density whereas the results from WAL decrease with increasing carrier density. In the heterostructures, the values of $\alpha$ determined by the two techniques show a similar dependence on the carrier density, but the values gained from SdH oscillations are an order of magnitude larger than those gained from WAL.
Both WAL and SdH oscillation experiments are performed on InAs/$In_{0.75}Ga_{0.25}As$ heterostructures with an ingrown back-gate. Application of voltages to the front-gate and the back-gate enable tuning of the strength of the Rashba parameter at a constant carrier density. A relative change in $\alpha$ of 17% is detected by WAL, and a change of over 100% is determined from SdH oscillations.
MOCVD grown $In_{0.53}Ga_{0.47}As$/$In_{0.52}Al_{0.48}As$ heterostructures are studied by the recently proposed technique of AAS oscillations. Samples with positive and negative potential gradients across the 2DEG, with and without an InP layer at one channel interface, are used to examine the interplay of the field and the boundary contributions to $\alpha$. Arrays of micrometer-sized ballistic square-loop interferometers are defined by electron-beam lithography. These exhibit distinct oscillations in the magnetoresistance at near-zero fields, the amplitude of which depends on $\alpha$. By combined use of WAL and AAS oscillations, the spin-orbit interaction strength in low magnetic fields is obtained for a wide range of carrier densities. Both additive and subtractive behaviour of the field and boundary contribution are observed in the $In_{0.53}Ga_{0.47}As$/$In_{0.52}Al_{0.48}As$ heterostructures.

# Inhaltsangabe

In dieser Arbeit wird die Rashba Spin-Bahn Wechselwirkung in zweidimensionalen Elektronengasen (2DEG) von III-V Schmalbandhalbleitern untersucht. Hauptursache der Spin-Bahn Wechselwirkung ist in diesen Halbleitern Strukturinversionsasymmetrie, deren Stärke durch den Rashba Parameter $\alpha$ beschrieben wird. Die Potentialgradienten senkrecht zum 2DEG und die Grenzflächen tragen zu $\alpha$ bei. In dieser Arbeit werden drei Messmethoden verwendet, um $\alpha$ zu bestimmen: Shubnikov-de Haas (SdH) Oszillationen in starken äußeren Magnetfeldern und Schwache Antilokalisierung (WAL) sowie Al'tshuler-Aronov-Spivak (AAS) Oszillationen in kleinen externen Magnetfeldern. Die Stärke von $\alpha$ wird durch Anlegen von Gatespannungen geregelt.
Messungen an Inversionsschichten von p-Typ InAs Einkristallen sowie an InAs/$In_{0.75}Ga_{0.25}As$ Heterostrukturen zeigen SdH Oszillationen und WAL. Für beide Materialsysteme stimmen die Ergebnisse aus WAL qualitativ und quantitativ mit durch $k \cdot p$ Theorie berechneten Werten überein. Aus den beiden Messmethoden der SdH Oszillationen und der WAL ergeben sich jedoch unterschiedliche Rashba Parameter. In den Inversionsschichten sind zwar die Größenordnungen von $\alpha$ vergleichbar, weisen aber eine gegensätzliche Abhängigkeit von der Ladungsträgerdichte $n_s$ auf: während die aus SdH Oszillationen bestimmten Werte mit ansteigendem $n_s$ zunehmen, nehmen die durch WAL bestimmten Werte ab. In den Heterostrukturen is die Abhängigkeit von $\alpha$ von $n_s$ für beide Meßmethoden vergleichbar, jedoch ergibt sich aus SdH Oszillationen ein um eine Größenordnung stärkerer Rashba Parameter, als aus WAL.
In InAs/$In_{0.75}Ga_{0.25}As$ Heterostrukturen mit eingewachsenem Back-Gate werden sowohl WAL als auch SdH Oszillationen beobachtet. Anlegen von Spannungen an ein Front-Gate oberhalb des 2DEG sowie an das Back-Gate ermöglicht die Stärke der Spin-Bahn Wechselwirkung bei unveränderter Ladungsträgerdichte zu regeln. Mittels WAL wurden Änderungen im Rashba Parameter von 17% bestimmt, und mittels SdH Oszillationen Änderungen von über 100%.
Die Spin-Bahn Wechselwirkung in $In_{0.53}Ga_{0.47}As$/$In_{0.52}Al_{0.48}As$ Heterostrukturen wird mit der vor kurzem vorgeschlagenen Methode der AAS Oszillationen untersucht. Das Zusammenspiel der Feld- und Grenzflächenbeiträge zu $\alpha$ wird an Proben untersucht, die positive bzw. negative Potentialgradienten senkrecht zum 2DEG aufweisen. Zusätzlich werden Proben mit und ohne an einer Kanalgrenzfläche eingewachsenen InP Schicht verwendet. Der Magnetowiderstand von Arrays ballistischer, quadratischer Interferometer weist Oszillationen in niedrigen Magnetfeldern auf, deren Amplitude von $\alpha$ abhängt. Durch Verwendung von WAL und AAS Oszillationen wird die Spin-Bahn Wechselwirkung in niedrigen Magnetfeldern über einen weiten Bereich von Ladungsträgerdichten untersucht. Sowohl additives wie auch subtraktives Verhalten der Feld- und Grenzflächeneffekte wird in den $In_{0.53}Ga_{0.47}As$/$In_{0.52}Al_{0.48}As$ Heterostrukturen beobachtet.

# Contents

**1 Introduction** **1**

**2 Basic concepts** **3**
2.1 Zero-field spin-splitting . . . . . 3
2.1.1 Bulk inversion asymmetry . . . . . 3
2.1.2 Structure inversion asymmetry . . . . . 4
2.1.3 Influence of boundary conditions . . . . . 7
2.2 Shubnikov-de Haas oscillations . . . . . 7
2.2.1 Common case . . . . . 8
2.2.2 Influence of spin-splitting . . . . . 8
2.3 Localisation phenomena . . . . . 10
2.3.1 Weak localisation . . . . . 10
2.3.2 Antilocalisation . . . . . 12
2.4 Al'tshuler-Aronov-Spivak oscillations . . . . . 14

**3 Processing and experimental techniques** **17**
3.1 Processing . . . . . 17
3.2 Low temperature magnetotransport experiments . . . . . 19

**4 p-type InAs single crystals** **20**
4.1 Material system . . . . . 20
4.2 Sample geometry . . . . . 21
4.3 Experiments . . . . . 21

**5 InAs heterostructures** **37**
5.1 Material system . . . . . 37
5.2 Sample geometry . . . . . 41
5.3 Experiments . . . . . 42
5.4 Low field experiments . . . . . 43
5.5 High field experiments . . . . . 46
5.6 Discussion . . . . . 51

**6 InAlAs/InGaAs heterostructures** **54**
6.1 Material system . . . . . 54
6.2 Sample geometries . . . . . 57
6.3 Experiments . . . . . 58

**7 Outlook and conclusions** **71**

**A Process parameters** **73**

**B Fit software** **79**

**C Contributions and publications** **80**

**Bibliography** **82**

**Acknowledgments** **89**

# 1 Introduction

The invention of the transistor in 1948 by Bardeen, Brattain, and Shockley marks the advent of the semiconductor age. In retrospect, however, the most significant step was taken in 1954, when Texas Instruments introduced silicon as a substrate. This paved the way for the production of field effect transistors, which had already been proposed by Lilienfeld in 1926 and by Heil in 1934[1]: the surface of silicon can easily be oxidised to $SiO_2$, the very good insulating properties of which make it an ideal gate oxide. In the late 1950s, Fairchild semiconductor placed several transistors on one piece of silicon: the first integrated circuit was devised. Since then, semiconductor technology has advanced rapidly, the number of transistors per chip being doubled every 18-24 months, while the price per transistor is halved [Moo65]. Current state-of-the-art microprocessors incorporate over 100 million transistors (in 2004) at feature sizes of about 100 nm, requiring extremely complex processing technology. In a few years time, the devices will be scaled down to the size of atoms, thus limiting further integration.

*Spintronics*, in which conventional charge-based electronics is augmented by use of the spin degree of freedom, provides many new applications and possibilities, and possibly also answers to some challenges of the semiconductor industry. Fuelled by the industrial success of metal-based spintronic systems, such as harddisk read heads based on the giant magnetoresistance effect [Bai88, Bin89], or magnetic memory based on magnetic tunnel junctions [Miy95, Moo95], interest in the behaviour of the electron spin in semiconductor systems has grown rapidly over the last decade. Many devices have been proposed, combining the advantages of metal-based spin systems with the tunability of semiconductors [Pri95, Bal00, Wol01, Aws02]. One prominent device is the spin-transistor proposed by Datta and Das in 1990 [Das90]. Here, two spin-aligners (e.g. ferromagnets) are positioned at either end of a semiconducting channel. One spin-aligner injects spin polarised current into the semiconductor channel, through which the current passes while experiencing tunable spin-precession. The second spin-aligner detects the spin orientation at the far side of the channel. All three processes involved, spin-injection, spin-control, and spin-detection, prove to be challenging on their own. However, insight into all three processes has been gained in the last few years: spin-polarised currents have successfully been injected into semiconductors from ferromagnetic metals [Ham99, Zhu01] and semiconductors [Ohn99, Fie99]. Calculations [Ras00] and experiments [Han02] even show that the injection efficiency can be significantly increased by placing tunnel barriers at the ferromagnet/semiconductor interface. In the experiments mentioned above, optical detection of spin-polarised currents was demonstrated. Recently, even successful electrical detection of spin-polarisation has been reported [Hu01, Mei02, Ham02].

In narrow-gap III-V semiconductors, spin-precession in the semiconductor channel can be

[1] Julius Lilienfeld proposed a metal-semiconductor based device (MES-FET), and Oskar Heil proposed the metal-oxide semiconductor device (MOS-FET) commonly used today.

controlled via the mechanism of so-called *Rashba spin-orbit interaction* [Ras60, Ras84]: breaking of symmetry results in lifted spin degeneracy in the semiconductor channel, and the spin states $|\uparrow\rangle$ parallel and $|\downarrow\rangle$ antiparallel to a local spin-basis $\vec{B}_R$ differ in energy. While moving through the channel, an electron in the state $|s\rangle=|\uparrow\rangle+|\downarrow\rangle$ precesses around the axis defined by $\vec{B}_R$ [Das90, Ž04]. The speed of the precession depends on the so-called Rashba parameter $\alpha$. Two major contributions to $\alpha$ can be identified, namely the electric field across the channel as well as the channel boundaries [Eng96, Eng97, Sch98]. By applying a gate voltage, the Rashba parameter can be tuned in various materials [Nit97, Hu99, Mat00, Kog02, Sch04]. In most cases, $\alpha$ was determined from Shubnikov-de Haas (SdH) oscillations in magnetic fields of several Tesla. However, these Rashba parameters do not necessarily agree with those at the near-zero magnetic fields, at which all proposed spintronic devices operate [Sch01, Sch02].
Weak antilocalisation (WAL) is well suited to determine the Rashba parameter at near-zero magnetic fields [Kna96, Kog02]. WAL originates from interference of time-reversed electron paths in two-dimensional electron systems. Applied magnetic fields destroy WAL, and a distinct signature in the magnetoconductance is observed which can be used to determine $\alpha$. As the time-reversed paths arise from scattering, weak antilocalisation is only observed in the regime of diffusive transport. However, the interference effects causing WAL can also be used to determine the Rashba parameter at higher electron mobilities: the low-field magnetoresistance of specifically designed interferometers exhibits Al'tshuler-Aronov-Spivak (AAS) oscillations, whose amplitude depends on the strength of $\alpha$ [Kog04].
Tuning of the Rashba parameter is usually accompanied by a change in carrier density. Devices that, in addition to a front-gate, feature a back-gate below the channel, may provide a solution to this problem. The combination of front-gate and back-gate should enable independent control of the carrier density and the Rashba parameter [Gru00].
The work of this thesis addresses four of the topics above. First, the effect of large external magnetic fields on the Rashba parameter is investigated: the value of $\alpha$ is determined both by WAL and by SdH oscillations for p-type InAs single crystals and for InAs/$In_{0.75}Ga_{0.25}As$ based heterostructures. Second, samples with ingrown back-gates are used to control the Rashba parameter independent of the carrier density. Third, the Rashba parameter is determined in low magnetic fields for a very wide range of carrier densities using WAL and AAS oscillations. Fourth, the interplay of the field and boundary contributions to the Rashba parameter are studied in samples with and without an intermediate layer at one boundary of a quantum well.
The thesis is structured as follows: the second chapter introduces spin-orbit interaction in III-V semiconductors, followed by an an overview of the effects used to determine and quantify this. Chapter 3 summarises the techniques used in sample processing and in transport experiments. Following this, Chapter 4 presents the results obtained in low and high magnetic fields on p-type InAs single crystals. Chapter 5 shows the measurements on heterostructures with an InAs channel and an ingrown back-gate. Then, in Chapter 6, measurements of AAS oscillations are shown, from which $\alpha$ is determined for a wide range of carrier densities. With these measurements, the interplay between the field and the boundary contribution is demonstrated for four different heterostructures with an InGaAs/InAlAs channels. This thesis closes with an outlook and conclusions in Chapter 7.

# 2 Basic concepts

In general, III-V semiconductors crystallise in the zinc-blende type lattice structure. Due to the inversion asymmetry of the crystal system, the spin degeneracy in the conduction band is lifted in the absence of external magnetic fields, and so-called zero-field spin-splitting occurs. This chapter gives an overview of both the physical origin of this zero-field spin-splitting in a two-dimensional electron gas (2DEG) and the phenomena used to quantify spin-splitting in transport experiments.

## 2.1 Zero-field spin-splitting

The spin degeneracy of electronic states in a 2DEG is lifted by breaking symmetry, either in time or in space [Rös89]. Time-reversal symmetry can be broken by an external magnetic field, resulting in the Zeeman effect [Zee97]. This thesis focusses on the breaking of spatial symmetry and the resulting so-called zero-field splitting that persists even in the absence of applied magnetic fields. The three main causes of this are the *bulk inversion asymmetry* (BIA), *structure inversion asymmetry* (SIA), and *interface inversion asymmetry* (IIA). The relative strengths of these depend on the choice of materials, dimensions, and boundaries of the channel and the 2DEG [Lom88, Ver97, Eng97].

### 2.1.1 Bulk inversion asymmetry

Unlike the diamond lattice structure of silicon, the zinc-blende lattice of III-V semiconductors lacks spatial inversion symmetry [Car88]. This inversion asymmetry leads to a spin-splitting that can be described by [Dre55, Pik95]:

$$\hat{H}_{BIA} = \gamma[\sigma_x k_x(k_y^2 - k_z^2) + \sigma_y k_y(k_z^2 - k_x^2) + \sigma_z k_z(k_x^2 - k_y^2)]. \quad (2.1)$$

Here, $\gamma$ is a material-dependent constant[1], $\sigma_i$ are the Pauli matrices and $k_i$ the wave vectors, for $i = x, y, z$. In the case of a 2DEG, electrons are confined to a two-dimensional plane of motion. This gives rise to linear terms, in addition to the cubic ones, in the in-plane wave vector $\vec{k}_\parallel$ . For confinement in direction of the z-axis this wave vector is given by $\vec{k}_\parallel = (k_x, k_y)$ and Eq.(2.1) results in [Kna96, Min04]:

$$\hat{H}_{BIA,2D} = \gamma\left[k_\parallel\left(\langle k_z^2\rangle - \frac{k_\parallel^2}{4}\right)(\sigma_x k_x - \sigma_y k_y) + \frac{k_\parallel^3}{4}(\sigma_x k_x^3 - \sigma_y k_y^3)\right], \quad (2.2)$$

with $\langle k_z^2\rangle$ being the mean square of the electron momentum in direction of the confinement.

[1] Some researchers refer to $\gamma$ as the Dresselhaus parameter.

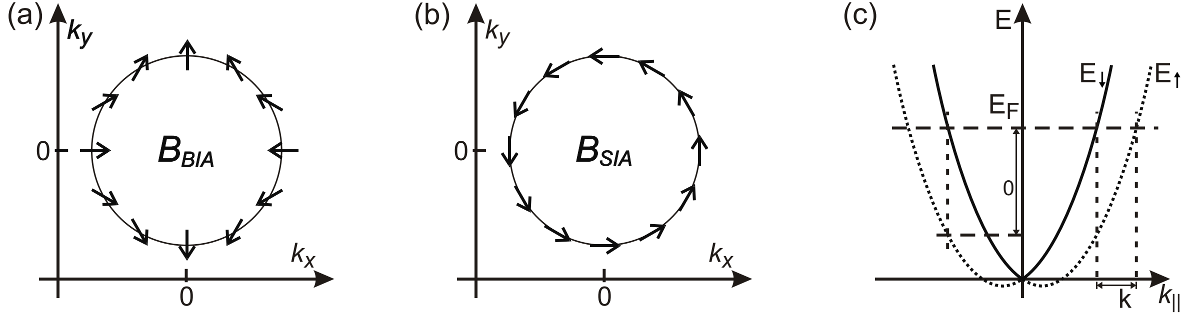


**Fig. 2.1:** Orientation of the local magnetic field caused by BIA for a 2DEG confined by a quantum well in [001] direction (a) and of the local magnetic field caused by SIA (b) according to [Win04]. Note that $\vec{B}_{BIA}$ is anisotropic in $\vec{k}_{||} = (k_x, k_y)$ while $\vec{B}_{SIA}$ is not. (c) Sketch of the dispersion relations $E_{\uparrow,\downarrow}(k_{||})$ in the presence of SIA. The indices $\uparrow$ and $\downarrow$ correspond to the two spin eigenstates of $\vec{B}_{SIA}$, and $E_F$ denotes the Fermi energy. The zero-field splitting $\Delta_0$ of the energy and $\Delta k$ of the wave vector between the two spin conduction-subbands are displayed.

The above contribution to zero-field spin-splitting is often called either *Dresselhaus term* after the author of the original publication [Dre55], or *bulk inversion asymmetry (BIA)* as it stems from the bulk semiconductor lattice, or simply $k^3$ *term* due to the cubic order dependency on the wave vector $k$ as is the case in bulk systems. Zero-field spin-splitting can be described by a local magnetic field that lifts spin degeneracy. The orientation of this local magnetic field is shown in Fig. 2.1(a) for the [001] plane of zinc-blende type semiconductors. From this and Eq.(2.2) it is easy to see that BIA is anisotropic in $\vec{k}_{||}$ and only affects electrons with finite $\vec{k}_{||}$, i.e. electrons in motion in the 2D plane.
The strength of the term linear in $\vec{k}_{||}$ is influenced by $\gamma$ but is also related to the thickness of the quantum well $d$ via $\langle k_z^2 \rangle \sim d^{-2}$. As only BIA shows an explicit dependence on the thickness of the quantum well, this can be used to determine the relative strength of BIA [Luo90]. BIA is the dominant origin of zero-field spin-splitting in wide-gap semiconductors such as AlAs. With decreasing bandgap, SIA becomes dominant and BIA can be neglected as is the case for InAs or InGaAs [Sch98, Mat00].

### 2.1.2 Structure inversion asymmetry

The confinement of electrons in a 2DEG is generally due to a quantum well. Usually, band offsets of the boundary materials or applied voltages lead to an asymmetry of this well. The breaking of spatial symmetry results in lifted spin degeneracy, which can be exemplified as follows: the asymmetric potential well effects an electric field $\vec{\mathscr{E}} = -\vec{\nabla}\varphi$, whereby $\varphi$ denotes the macroscopic electrical potential across the well. When passing through this field, the conduction electrons interact with $\vec{\mathscr{E}}$: however, due to the Lorentz transformation, $\vec{\mathscr{E}}$ appears as a magnetic field $\vec{B}_{SIA}$ when observed from the reference frame of a moving electron. The local magnetic field $\vec{B}_{SIA}$ is always perpendicular to both $\vec{\mathscr{E}}$ and to the vector of electron motion, as can be seen in Fig. 2.1(b). It can be understood as the origin of spin-splitting analogous to an external magnetic field causing the Zeeman effect. For a quantum well confined in the direction of the z-axis, the resulting spin-

splitting is described by [Ras60, Ras84]:

$$\begin{aligned}\hat{H}_{SO} &= \alpha[\vec{\sigma}\times\vec{k}]\cdot\hat{e}_z,\\ &= \alpha(\sigma_x k_y - \sigma_y k_x).\end{aligned} \tag{2.3}$$

In this equation $\vec{\sigma}$ denotes the vector of Pauli-matrices, $\vec{k}$ is the electron wave vector and $\hat{e}_z$ is a unit vector parallel to the electric field $\vec{\mathscr{E}}$. The spin-orbit interaction parameter $\alpha$, also called the Rashba parameter, indicates the strength of the spin-orbit interaction and depends on the asymmetry of the quantum well. Assuming parabolic conduction bands, Eq.(2.3) yields the following energy dispersion relations:

$$E_\uparrow(\vec{k}_\parallel) = E_i + \frac{\hbar^2 k_\parallel^2}{2m^*} - \alpha|\vec{k}_\parallel|, \qquad E_\downarrow(\vec{k}_\parallel) = E_i + \frac{\hbar^2 k_\parallel^2}{2m^*} + \alpha|\vec{k}_\parallel|, \tag{2.4}$$

where $E_i$ is the respective subband ground-state energy and the indices $\uparrow$ and $\downarrow$ correspond to the states $|\uparrow\rangle$ and $|\downarrow\rangle$ parallel to the two eigenvectors of the spin-basis system constituted by $\vec{B}_{SIA}$. Spin degeneracy is lifted in the absence of external magnetic fields, so SIA also contributes to zero-field spin-splitting. Fig. 2.1(c) shows a sketch of the two energy dispersions described by Eq.(2.4). The wave-vectors of the two spin orientations, $k_\uparrow$ and $k_\downarrow$, differ for any given energy, and their difference can be derived from Eq.(2.4) to be:

$$\Delta k = k_\uparrow - k_\downarrow = \frac{2m^*\alpha}{\hbar^2}. \tag{2.5}$$

The electron wave vector $\vec{k}$ is associated with the phase $\psi$ according to $\psi \sim e^{i\vec{k}\vec{r}}$. In the presence of SIA the spin eigenstates $|\uparrow\rangle$ and $|\downarrow\rangle$ will dephase with respect to each other, and mixed states will experience spin precession. An especially interesting case occurs when the spin is of an equal superposition of the two spin basis states, i.e. $\frac{1}{\sqrt{2}}(|\uparrow\rangle + |\downarrow\rangle)$. The spin then precesses in the plane defined by $\vec{\mathscr{E}}$ and $\vec{k}$, whereby the angle of precession is given by [Dat90]:

$$\theta = \Delta k\, L = \frac{2m^*\alpha L}{\hbar^2}, \tag{2.6}$$

with L being the channel length[2]. Because the spin's precession depends on the motion of the electron through the crystal lattice, the precession is often referred to as *spin-orbit interaction*. Tunable spin-orbit interaction is necessary for tunable spintronic devices such as the spin-transistor [Dat90]. In a given device, tunability can be achieved by changing $\alpha$, e.g. by changing the asymmetry of the potential well.

In the case of parabolic band structure, the Rashba parameter $\alpha$ also gives the correlation between the strength of zero-field spin-splitting $\Delta_0$ and $\Delta k$, as can be derived from Eq.(2.3):

$$\Delta_0 = 2\alpha\Delta k. \tag{2.7}$$

A graphic description of these parameters is included in Fig. 2.1(c). The Rashba parameter can be described as [dAeS94, Eng96, Sch98]:

$$\alpha = \frac{\hbar^2 E_p}{6m_e}\left\langle \Psi \middle| \frac{d}{dz}\left(\frac{1}{E - E_{\Gamma_7} - \varphi(z)} - \frac{1}{E - E_{\Gamma_8} - \varphi(z)}\right) \middle| \Psi \right\rangle, \tag{2.8}$$

[2] A more extensive description of the spin precession is given in reference [Sch01].

with the $k \cdot p$ interaction parameter $E_p$, the free electron mass $m_e$, the subband energy $E$ in the quantum well, the respective energies $E_{\Gamma_8}$ and $E_{\Gamma_7}$ of the valence band and the spin split-off band, and the electrical potential $\varphi(z)$. Here, the z-axis is defined as pointing from the sample surface to the substrate. When determining the derivative in Eq.(2.8), the regions of continuous potential and the boundaries between two materials must be considered separately. The so-called *field contribution* $\alpha_f$ to the Rashba parameter stems from the regions of continuous potential:

$$\begin{aligned} \alpha_f &= \underbrace{\frac{\hbar^2 E_p}{6m_e}\left(\frac{1}{[E-E_{\Gamma_7}(z)-\varphi(z)]^2}-\frac{1}{[E-E_{\Gamma_8}(z)-\varphi(z)]^2}\right)}_{C_f}\langle\Psi|\frac{d\varphi}{dz}|\Psi\rangle \\ &= -C_f(z)\, e\langle\Psi|\mathscr{E}_z|\Psi\rangle \end{aligned} \tag{2.9}$$

with the electrical field $\mathscr{E}_z = -\frac{1}{e}\frac{d\varphi}{dz}$ across the channel. Note that $C_f$ is always negative, as $E - E_{\Gamma_7}$ is larger than $E - E_{\Gamma_8}$ for all materials, so that the sign of the field contribution is set by $\langle\Psi|\mathscr{E}_z|\Psi\rangle$. Due to the changes in band structure, the derivative in Eq.(2.8) shows a discontinuity at interfaces between different materials. Separate treatment of this derivative for the interfaces yields the so-called *boundary contribution* $\alpha_{b,i}$ to the Rashba parameter, whereby the index $i$ indicates the respective interface at the position $z_i$:

$$\begin{aligned} \alpha_{b,i} &= \underbrace{\frac{\hbar^2 E_p}{6m_e}\left(\frac{\Delta E_{\Gamma_7}(z_i)}{[E-E_{\Gamma_7}(z_i)-\varphi(z_i)]^2}-\frac{\Delta E_{\Gamma_8}(z_i)}{[E-E_{\Gamma_8}(z_i)-\varphi(z_i)]^2}\right)}_{C_{b,i}}|\Psi(z_i)|^2 \\ &= C_{b,i}\,|\Psi(z_i)|^2 \end{aligned} \tag{2.10}$$

where $\Delta E_{\Gamma_7}(z_i) = E_{\Gamma_7}(z < z_i) - E_{\Gamma_7}(z > z_i)$ and $\Delta E_{\Gamma_8}(z_i) = E_{\Gamma_8}(z < z_i) - E_{\Gamma_8}(z > z_i)$ are the energetic changes of the $\Gamma_7$ and $\Gamma_8$ bands at the position of the boundary $i$ and $|\Psi(z_i)|^2$ is the probability density of the electron wave function . $E_{\Gamma_7}(z_i)$ and $E_{\Gamma_8}(z_i)$ are defined as the mean values of the respective band energies on both sides of the boundary. Both field and boundary contribution must be considered to properly describe spin-orbit interaction in semiconductor heterostructures [Eng96, Gru00]. The total Rashba spin-orbit interaction parameter results as the sum of the two:

$$\alpha_{tot} = \alpha_f + \sum_i \alpha_{b,i}, \tag{2.11}$$

in which the sum accounts for all boundaries $i$, at which the value of $|\Psi(z_i)|^2$ is not zero. The relative importance of the field and the boundary contribution can be clarified by analysing two basic potential designs, a square quantum well with differing boundary materials and $\mathscr{E}_z = 0$ as well as a quantum well with identical boundary materials but $\mathscr{E}_z \neq 0$. In the former case spin-orbit interaction can be exclusively attributed to the boundary contribution due to differing pre-factors $C_{b,u}$ and $C_{b,l}$ for the upper and lower channel boundaries [dAeS97]. In the latter case both field and boundary contributions contribute to spin-orbit interaction, whereby the field contribution dominates [Eng97, Sch98, Lin05]. In general, a full description of SIA requires consideration of both field and boundary contributions.

The description of spin-splitting becomes much more complex for non-parabolic bands. In the

simplest approach, band non-parabolicity is accounted for by using a wave-vector dependent effective mass $m^*(\vec{k})$. More refined approaches can be found e.g. in references [dAeS94, Mat00]. Zero-field spin-splitting due to an external asymmetric potential is commonly referred to as the *Rashba-effect*, caused by *structure inversion asymmetry* (SIA).
The relative strengths of the BIA and the SIA contributions to zero-field spin-splitting depend on the material system. In a rough approximation, the influence of the SIA term increases with decreasing bandgap: in III-V semiconductors with large bandgaps, e.g. AlAs[3], BIA is the main origin of zero-field splitting, whereas SIA dominates in materials with small bandgaps such as InAs[3]. For example, it has been shown theoretically that BIA is the main origin of zero-field splitting in AlGaAs/GaAs systems and that SIA dominates splitting in InAs-based heterostructures [Lom88, dAeS94]. However, of these two mechanisms, only SIA is tunable by an external parameter, e.g. a gate voltage, thus enabling control of spin-orbit interaction in a given semiconductor device.

### 2.1.3 Influence of boundary conditions

Recent experiments have shown that the boundaries of a quantum well have an additional influence on the strength of spin-orbit interaction. If the materials of the channel and its boundaries differ, the different compositions of constituents yield localized electric charges which are the source of *interface inversion asymmetry* (IIA) [Ver97, Kre98, Ole01]. For semiconductors with a zinc-blende lattice structure IIA is not distinguishable from BIA as the respective Hamiltonians are of the same shape [Gan03]. In fact, different strengths of IIA are observed as an enhancement or reduction of the effects typical to BIA. Therefore both effects are commonly described together using an effective combined Dresselhaus parameter $\gamma_c$ that incorporates both BIA and IIA contributions [Gan04].

## 2.2 Shubnikov-de Haas oscillations

When a magnetic field $B_\perp$ perpendicular to a high-mobility 2DEG is varied, oscillations in the magnetoresistance are observed. The carrier density distribution of the 2DEG can easily be determined from these so-called *Shubnikov-de Haas* (SdH) *oscillations* [Shu30]. Zero-field spin-splitting commonly leads to slightly different carrier densities of the two non-degenerate spin populations. Two distinct peaks are observed in the carrier density distribution, from which the strength of the splitting can be determined. In SdH experiments, the presence of two carrier densities manifests itself as beating patterns in the oscillations [Luo88, Nit97, Mat00].

[3]bandgap of AlAs: 2160 meV; bandgap of GaAs: 1514 meV; bandgap of InAs: 418 meV.

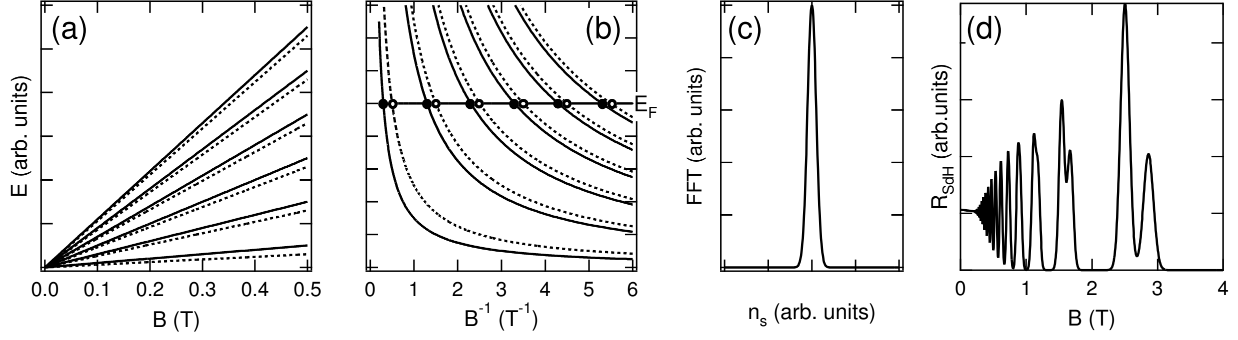


**Fig. 2.2:** Simulation of Zeeman effect: (a) Landau levels in dependence of the magnetic field for both spin orientations. (b) Landau levels plotted as a function of the reciprocal magnetic field. The intersections with the Fermi energy $E_F$ are marked by circles – note that the frequency of intersections in $B^{-1}$ is identical for both spin orientations. (c) simulated FFT of the SdH oscillations yielding the carrier density distribution. (d) SdH oscillations simulated as described in Ref. [Luo90].

### 2.2.1 Common case

In a finite perpendicular field $B_\perp > \mu^{-1}$ ($\mu$: mobility) the electrons of a 2DEG settle on so-called Landau levels[4], the energies of which are given by:

$$E_{j,n} = E_{j,0} + \left(n + \frac{1}{2}\right)\frac{\hbar e B_\perp}{m^*}, \qquad n \in \mathbb{N}\ . \tag{2.12}$$

where $E_{j,0}$ is the ground-state energy of the 2DEG subband. Varying $B_\perp$ changes the energies of the Landau levels, which pass through the Fermi energy with increasing magnetic field. As the total number of electrons is conserved, the reducing number of Landau levels with increasing $B_\perp$ are compensated by an increasing number of electron states per level. Due to scattering processes the Landau levels are broadened but do not overlap, so that the resistance of the 2DEG is high when a level passes through the Fermi energy and low when the Fermi energy lies between levels: an oscillatory magnetoresistance of the 2DEG is observed. This oscillation is periodic with the reciprocal magnetic field, and the carrier density $n_s$ can be determined from it as:

$$\Delta\left(\frac{1}{B_\perp}\right) = \frac{e}{\hbar\pi n_s} \quad \Rightarrow \quad n_s = \frac{e}{\hbar\pi\Delta(1/B_\perp)} \simeq \frac{4.839\cdot 10^{10}\mathrm{cm}^{-2}}{\Delta(1/\mathrm{B}_\perp)}. \tag{2.13}$$

Note that Eq.(2.13) assumes two-fold spin degeneracy[5]. A fast Fourier transform (FFT) of recorded SdH oscillations versus the reciprocal magnetic field yields the carrier density distribution.

### 2.2.2 Influence of spin-splitting

When an external magnetic field $B$ is applied to a 2DEG, time-reversal symmetry is broken. The electron spin can align parallel and antiparallel to $B$, whereby the energy differs between the two

[4] In a semiclassical picture, the Landau levels can be understood as closed circular orbits. Electrons will only condense on these if they can complete an orbit without scattering, which is the case for $B_\perp > \mu^{-1}$ [Dat95].

[5] To obtain the carrier densities of the spin-subbands in the case of lifted spin degeneracy, all values for $n_s$ must be multiplied with a factor of two.

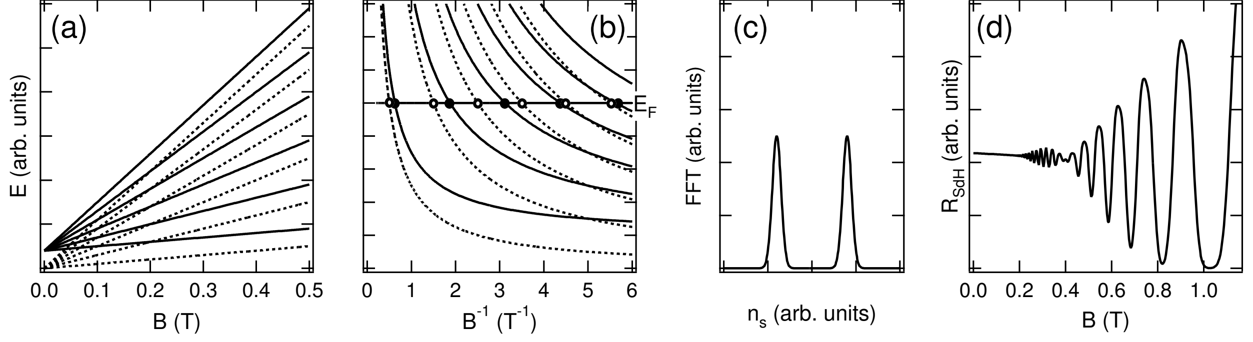


**Fig. 2.3:** Simulated zero-field spin-splitting: (a) Landau levels in dependence of the magnetic field for both spin orientations. (b) Landau levels plotted as a function of the reciprocal magnetic field. The passes through the Fermi energy $E_F$ are marked by circles. The frequency of the passes in $B^{-1}$ is not identical for the two spin orientations. (c) simulated FFT of the SdH oscillations yielding the carrier density distribution – note the presence of two different frequencies due to different carrier densities of the spin subbands. (d) simulated SdH oscillations, the beating pattern occurs due to the two differently occupied spin subbands. Simulations are performed as described in Ref. [Luo90].

spin orientations. Thus spin degeneracy is lifted, and so-called Zeeman spin-splitting occurs. The strength of Zeeman spin-splitting is proportional to the strength of the overall external magnetic field and can be accounted for by supplementing to Eq.(2.12) to obtain:

$$E_{j,n,s} = E_{j,0} + \left(n + \frac{1}{2}\right)\frac{\hbar e B_\perp}{m^*} + sg\mu_B B, \qquad n \in \mathbb{N}\,. \tag{2.14}$$

where $s = \pm 1/2$ denotes the spin quantum number, $g$ is the electron $g$-factor, and $\mu_B$ is the Bohr magneton. Simulated Landau levels and SdH oscillations for the case of Zeeman splitting are shown in Fig. 2.2. Two superimposed SdH oscillations, one for each of the spin-subbands, can be observed. As both oscillations are of the same frequency in the inverse magnetic field, the FFT yields only one carrier density.

When zero-field spin-splitting prevails and Zeeman splitting is ignored, Eq.(2.12) must be altered to:

$$E_{j,n} = E_{j,0} + \left(n + \frac{1}{2}\right)\frac{\hbar e B_\perp}{m^*} \pm \frac{1}{2}\Delta_0, \qquad n \in \mathbb{N}\,. \tag{2.15}$$

where $\Delta_0$ is the zero-field energy splitting. Simulated Landau levels for the case of zero-field spin-splitting are displayed in Fig. 2.3. The zero-field spin-splitting gives rise to two distinct carrier densities, one for each spin-subband, which result in two frequencies in $B^{-1}$ of the Landau levels passing through the Fermi energy. This is observable as a beating pattern in the SdH oscillations. The analysis of beating patterns in SdH oscillations is a standard procedure to determine the strength of spin-orbit interaction, i.e. the Rashba parameter $\alpha$. In a simple approach that only accounts for band non-parabolicity via the effective mass, the following relations can be used to

determine $\alpha$ from the spin subband carrier densities gained from SdH oscillations (cf. [Dat90]):

$$\begin{aligned} \Delta k &= k_\uparrow - k_\downarrow = \frac{2m^*\alpha}{\hbar^2} \\ \Leftrightarrow \quad \alpha &= \frac{\hbar^2 \Delta k}{2m^*} \qquad \Big| k_i = \sqrt{4\pi n_i} \\ \Rightarrow \quad \alpha &= \frac{\hbar^2(\sqrt{4\pi n_\uparrow} - \sqrt{4\pi n_\downarrow})}{2m^*} \end{aligned} \tag{2.16}$$

whereby $k_i$ and $n_i$ ($i = \uparrow, \downarrow$) denote the wave vectors and carrier densities of the respective spin subbands $\uparrow$ and $\downarrow$. More complex analyses accounting for band non-parabolicity ab initio can be found e.g. in Refs. [dAeS97, Hu99, Mat00].

## 2.3 Localisation phenomena

In diffusive transport the free length of path of the conduction electrons is limited by scattering processes. These allow for closed-loop paths along which the electrons are backscattered to their origin. Under certain conditions this backscattering gives rise to interference effects and thus causes conductance corrections. Two cases are distinguished: absence and presence of spin-orbit interaction. In the latter case, the strength of spin-orbit interaction in the system can be determined by approximating the conductance corrections with a model function. The quantum mechanical phenomena underlying the interference effects will now be introduced for the case of a 2DEG.

### 2.3.1 Weak localisation

In absence of spin-orbit interaction and spin-scattering, non-ballistic transport is governed by elastic and inelastic scattering. These processes are commonly described by $\tau_\varphi$ and $\tau_i$, the mean times between elastic and inelastic scattering processes, respectively. As shown in Fig. 2.4(a), multiple scattering can cause closed loop paths. Both directions of motion along such a path are equally probable, so that the point of origin of the closed loop path can be viewed as a beam-splitter providing one partial wave in each direction of motion. Abiding by the waveform model, backscattering can be described as follows: let $A$ be the amplitude of an electron wavefunction $\psi = A_0 \cdot e^{i\varphi}$ after having completed a given closed loop path C (and $A'$ the corresponding amplitude of the wavefunction $\psi' = A_0' \cdot e^{i\varphi'}$ of the path C' that follows the loop in the opposite direction). Then, the intensity of backscattering $I_{back}$ after one loop is given by [Dat95]:

$$I_{back} = |\psi|^2 + |\psi'|^2 = \psi^*\psi + \psi'^*\psi' = 2A_0^2 \qquad \Big| \text{with } |\mathrm{A}_0| = |\mathrm{A}_0'|. \tag{2.17}$$

An interesting case occurs if $\tau_i$ exceeds $\tau_\varphi$: multiple elastic scattering is possible between two inelastic scattering events so that electrons can complete closed loop trajectories in the 2DEG while maintaining phase coherence. The two partial waves (along C and C') interfere with each

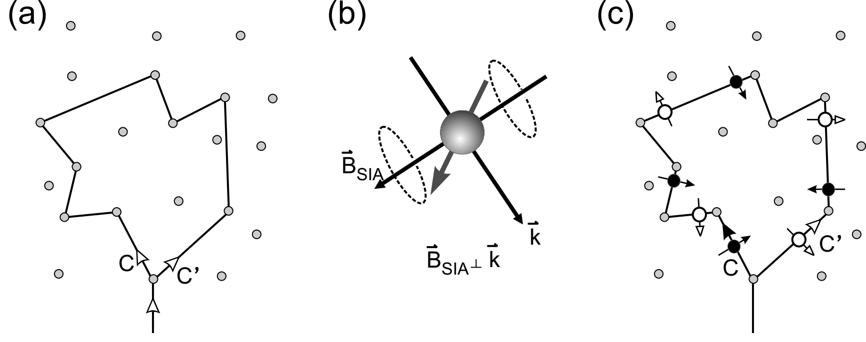


**Fig. 2.4:** (a) Scattering enables closed loop trajectories. Both possible paths of motion C and C' along a given trajectory are equally probable. In the case of coherent transport along the closed loop paths, interference of the partial waves travelling along C and C' occurs on return to the origin. (b) In the case of SIA, the local magnetic field $\vec{B}_{SIA}$ is perpendicular to both the electric field $\vec{E}$ of the confining potential (not depicted here) and the electron wave vector $\vec{k}$. $\vec{B}_{SIA}$ defines the local spin-basis. (c) Closed loop paths in presence of SIA and long spin-coherence lengths: the conduction electron's spin will follow the local spin-basis $\vec{B}_{SIA}$ quasi-adiabatically. The two paths C and C' are marked with black and white symbols and arrows. Note that the spins are rotated in opposite directions when following C and C'; by 180° in clockwise orientation when following C and by 180° in counterclockwise orientation when following C'. Therefore, the spins of the two partial waves are rotated by 360° with respect to each other.

other after having completed such a closed loop path. In this case, interference terms must be considered, so that the intensity results in:

$$\begin{aligned} I_{back} &= |\psi + \psi'|^2 = \psi^* \psi + \psi^* \psi' + \psi'^* \psi + \psi'^* \psi' \\ &= A_0^2 + A_0 A_0' + A_0' A_0 + A_0'^2 = 4A_0^2 \qquad \Big| \text{with } \mathrm{A}_0 = \mathrm{A}_0', \varphi = \varphi', \forall \text{ paths.} \end{aligned} \tag{2.18}$$

It can be seen from equations (2.17) and (2.18) that the backscattering amplitudes of incoherent and coherent closed-loop paths differ by a factor of two. The interference enhances backscattering which results in reduced conductivity. The reduction of conductivity by constructive coherent backscattering is called *weak localisation*.

Weak magnetic fields $B_\perp$ are applied perpendicular to the 2DEG to quantify the effect of weak localisation. The field quenches localisation in the following way: let $S_C$ be the area enclosed by the closed loop path C. With the magnetic field described as $\vec{B_\perp} = \vec{\nabla} \times \vec{D}$ ($\vec{D}$: vector potential), a charged particle moving along $C$ experiences a phase shift of [Sch90]:

$$\Phi_{mag}(B_\perp) = \frac{ie}{\hbar} \oint_C \vec{D} d\vec{r} = \frac{ie}{\hbar} B_\perp S_C. \tag{2.19}$$

The resulting phase shift $\Phi'_{mag}$ for a particle moving along $C'$ is identical in magnitude but opposite in sign. The total phase difference between the interfering partial waves $\Phi_{tot} = \Phi_{mag} - \Phi'_{mag} = 2|\Phi_{mag}|$ increases with increasing magnetic field so that the magnitude of the interference term oscillates with magnetic field. As all possible coherent closed-loop paths in the system, in particular those enclosing areas of different sizes and thus having different frequencies of oscillation, must be considered, an applied magnetic field effectively destroys the reduction of conductivity caused by

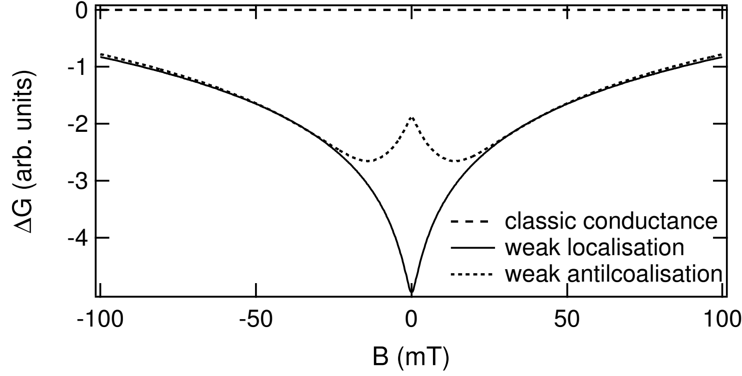


**Fig. 2.5:** Simulated magnetoconductances of a 2DEG in a perpendicular external magnetic field. Classical conductance (dashed line), weak localisation (solid line) and coexistance of weak localisation and antilocalisation (dotted line) are displayed.

weak localisation[6]. The probability of backscattering, and with it the conductance correction due to weak localisation, decreases monotonously with increasing magnetic field until it disappears completely at a field $B_{crit}$ [Dat95]. The destruction of weak localisation by magnetic fields leads to a characteristic magnetoconductance signature that is exemplarily depicted in Fig. 2.5.

### 2.3.2 Antilocalisation

Zero-field spin-splitting influences the effect of weak localisation: the constructive interference that promotes backscattering in the case of weak localisation can be turned into destructive interference that reduces backscattering. A reduced backscattering leads to an increase in conductance. If zero-field spin-splitting is caused by SIA, the reduction in backscattering can be described by a simple graphic approach: as shown earlier, the local magnetic field $\vec{B}_{SIA}$ induced by SIA is always perpendicular to both the electric field $\vec{E}$ of the confining potential and the in-plane wave vector $\vec{k}_{\parallel}$. $\vec{B}_{SIA}$ constitutes the local spin-basis, as can be seen in Fig. 2.4(b). In III-V semiconductors that lack inversion symmetry, e.g. in GaAs or InAs, the D'yakonov-Perel mechanism dominates spin dephasing [Ž04] so that the electron spin will follow the local spin-basis quasi-adiabatically[7]. After completion of a closed-loop path $C$, the spin of an electron is rotated by 180° with respect to its initial state, as can be seen in Fig. 2.4(c). However, the direction of spin rotation is opposite for electrons moving along the same path in opposite directions, i.e. following $C$ or $C'$, respectively. Thus, on return to the origin, the spins of the electrons following $C$ are rotated by 360° with respect to those following $C'$. If the paths are phase-coherent, i.e. contribute to weak localisation, then the rotation of the spins of the two paths will affect the interference: the spin-$\frac{1}{2}$ wave function is pe-

[6]This is contrary to the case of lithographically patterned interferometers with only one or a strictly limited number of possible paths (e.g. Aharonov-Bohm rings [Tim87, Nit02]) in which $B_{\perp}$ will lead to an oscillation of the conductance.

[7]The orientation of $\vec{B}_{SIA}$ changes with each change in direction of $\vec{k}_{\parallel}$. Quasi-adiabaticity implies quasi-instant and continuous following of the changes in $\vec{B}_{SIA}$ by the electron spin. For an overview of spin dephasing mechanisms see [Fab99].

riodic by 720° with respect to rotations in real space [Aha67] so that rotation of two interfering spins by 360° to each other effects a sign change of the interference [Ber84]. A sign change in the interference term corresponds to a change from constructive to destructive interference or, when considering the system as a whole, from an increase in backscattering to a decrease. The resulting increase in conductance is called *weak antilocalisation* (WAL).

A full description of WAL is achieved by considering zero-field spin-splitting as a spin dependent vector potential[8] as done by *Iordanski, Lyanda-Geller, and Pikus* (ILP). From this one obtains a full theoretical description of the magnetoconductance corrections caused by weak localisation and antilocalisation in the presence of zero-field spin-splitting [Ior94]:

$$\begin{aligned}\Delta\sigma(B_\perp) = & -\frac{e^2}{4\pi^2\hbar}\left\{\frac{1}{a_0}+\frac{2a_0+1+b_{so}}{a_1[a_0+b_{so}]-2b_{so}}\right.\\ & -\sum_{n=1}^{\infty}\left[\frac{3}{n}-\frac{3a_n^2+2a_nb_{so}-1-2b_{so}(2n+1)}{[a_n+b_{so}]a_{n-1}a_{n+1}-2b_{so}[(2n+1)a_n-1]}\right]\\ & \left.+\ 2ln(b_{tr})+\Psi\left(\frac{1}{2}+b_\varphi\right)\right\}, \end{aligned} \tag{2.20}$$

with:

$$\begin{aligned} a_n &= n+\frac{1}{2}+b_\phi+b_{so}, \\ \Psi(1+x) &= \sum_{n=1}^{\infty}\frac{x}{n(n+x)}, \\ b_{tr}=\frac{H_{tr}}{B_\perp}, \qquad b_\varphi &= \frac{H_\varphi}{B_\perp}, \qquad b_{so}=\frac{H_{so}}{B_\perp}. \end{aligned} \tag{2.21}$$

Here, $\Psi$ denotes the Digamma function[9] and $B_\perp$ is the component of the magnetic field perpendicular to the 2DEG. If Rashba spin-splitting is explicitly ignored, i.e. the cubic Dresselhaus term remains as only contribution to spin-splitting, then the ILP theory is reduced to the expression formerly obtained by Hikami, Larkin and Nagaoka (HLN) [Hik80]. This was, albeit incorrectly, used to analyse early WAL data in systems with zero-field spin-splitting [Dre92, Che93, Sch02].

The independent variables of Eq.(2.20) are $B_\perp$ and the characteristic magnetic fields $H_{tr}$, $H_\varphi$, and $H_{so}$. The values of $H_\varphi$ and $H_{so}$, which indicate the strengths of inelastic dephasing and spin-orbit interaction, effect the shape of $\Delta\sigma(B_\perp)$ whereas $H_{tr}$ only leads to an offset [Kog02].

If the linear contributions to zero-field spin-splitting dominate, then one obtains the following association with the respective scattering times $\tau_i$ $(i=\varphi, tr)$ and $\Delta_0$ [Ior94, Kna96]:

$$H_\varphi=\frac{\hbar}{4De\tau_\varphi}, \qquad H_{tr}=\frac{\hbar}{4De\tau_{tr}}, \qquad H_{SO}=\frac{1}{8\hbar De\Delta_0^2\tau_{tr}}, \tag{2.22}$$

where $D$ denotes the diffusion coefficient. Note that $\Omega_1$ in the references [Ior94, Kna96] is defined as half the zero-field splitting $\Delta_0 = 2\Omega_1$. Using the result for $H_{SO}$ from Eq.(2.22), the relation

[8] In analogy to the vector potential $\vec{D}$ of an external magnetic field, this vector potential yields a total effective magnetic field which can be understood as a superposition of $\vec{B}_{BIA}$ and $\vec{B}_{SIA}$.

[9] $\Psi(x)=\frac{d\Gamma(x)}{dx}=\frac{d}{dx}(\int_0^\infty e^{-t}t^{x-1}dt), \quad x>0.$

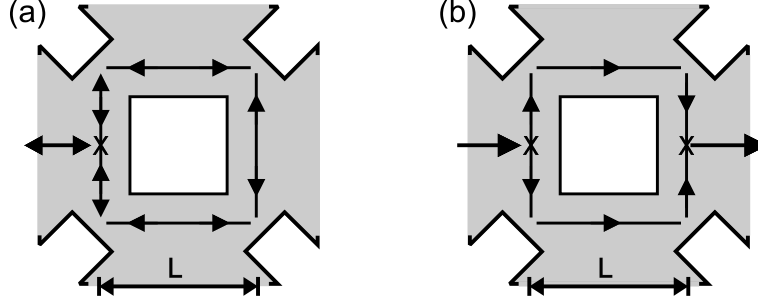


**Fig. 2.6:** Schematic of a square spin interferometer. (a) In the case of AAS oscillations, two paths of motion with equal probability but with electrons running in opposite directions exist. On return to the origin self-interference with the respective time-reversed path occurs. (b) Aharonov-Bohm type paths in an interferometer.

$\Delta_0 = 2\alpha k_F$ for the zero-field spin-splitting energy $\Delta_0$, and the diffusion coefficient given by

$$D = \frac{\tau_{tr} v_F^2}{2} \qquad \Big| \qquad v_F = \frac{\hbar k_F}{m^*}$$

$$\Rightarrow \quad D = \frac{\tau_{tr} \hbar^2 k_F^2}{2(m^*)^2}, \tag{2.23}$$

one can determine the spin-orbit interaction parameter $\alpha$ from fitting experimental weak antilocalisation data with Eq.(2.20) according to:

$$\alpha = \pm \frac{\sqrt{\hbar^3 e H_{SO}}}{m^*}. \tag{2.24}$$

Experimental data can be fit with Eq.(2.20) to yield the characteristic fields. In addition to these, the only information required to determine the strength of spin-orbit interaction is the effective electron mass, as can be seen in Eq.(2.24). The effective mass is obtained from temperature-dependent SdH oscillations or cyclotron resonance [And82, Neh95].

## 2.4 Al'tshuler-Aronov-Spivak oscillations

The two previously presented methods to quantify spin-orbit interaction require either diffusive transport, as is the case for WAL, or high-mobility samples and high magnetic fields, as is the case for SdH oscillations. In contrast, specifically designed interferometers provide a system well suitable to determine the strength of spin-orbit interaction in high-mobility samples at low magnetic fields. Closed loop spin-interferometers have been proposed for both circular [Nit99] and square [Kog04] geometries. Experiments on circular interferometers prove to be difficult, as electrons are required to complete a full circular loop ballistically and without scattering. Square loop systems, as depicted in Fig. 2.6, are more simple to implement: ballistic electron transport along the sides of the interferometer and spin-preserving scattering at each corner are sufficient prerequisites to observe interference effects.

In a designed interferometer the same effects prevail as in a 2DEG plane. Concerning closed-loop

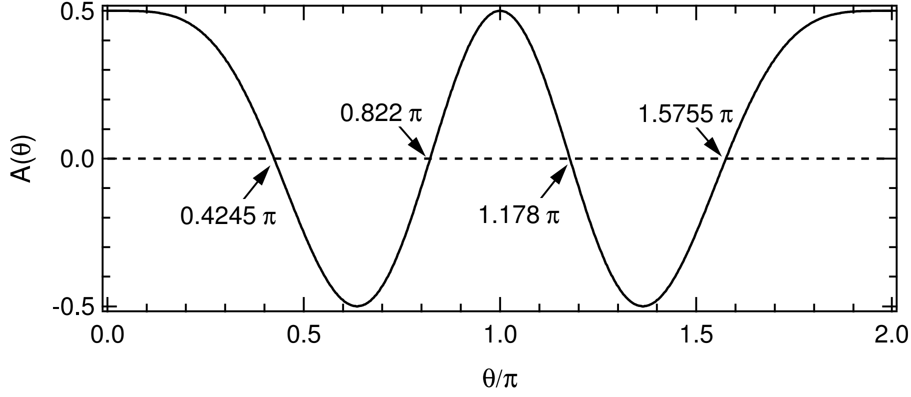


**Fig. 2.7:** Calculated amplitude of AAS oscillations as a function of the spin precession angle $\theta$ along one side of the length $L$ of the interferometer (cf. Eq.(2.25)). The passes through zero are marked. They can easily be distinguished in experimental data and thus are very suitable to determine the Rashba parameter.

trajectories, the shape of the interferometer ideally limits the number of possible paths to one. Thus, the effects underlying weak localisation and antilocalisation in a disordered system now lead to oscillations of the magnetoresistance in an external magnetic field $B_\perp$: the entry point to the loop can again be considered as a beam splitter, creating two equally probable partial waves that travel around the interferometer in opposite directions. After completing a full path around the loop they interfere.
When a magnetic field $B_\perp$ is applied perpendicular to the loop, the partial waves experience a phase shift $\Phi_{mag}$ as described by Eq.(2.19). The sign of the phase shift is opposite for the two partial waves so that the interference oscillates with a period of $\frac{h}{2eL^2}$ ($L^2$: loop area). These are the so-called *Al'tshuler Aronov Spivak* (AAS) oscillations [Al'81]. In single interferometers, Aharonov-Bohm type oscillations with a period of $\frac{h}{eL^2}$ can be observed [vdW03]. These originate from the interference of two partial waves that each complete half a passage through the interferometer on *different* paths (cf. Fig. 2.6(b)). However, Aharonov-Bohm type effects are suppressed in arrays of interferometers [Dol86] and will thus be neglected here.
Spin-orbit interaction influences both sign and strength of the interference that leads to AAS oscillations: the spin of an electron moving through the interferometer precesses, whereby the precession angle $\theta$ for transport along one side of the interferometer of length $L$ is given by Eq.(2.6). The stronger the spin-orbit interaction is, the greater the angle of precession. Thus the angle between the spins of the electrons on time-reversed paths at return to the origin is dependent on the strength of spin-orbit interaction. This results in an oscillatory dependence of the backscattering amplitude $A$ on the precession angle and thus on the spin-orbit interaction strength [Kog04]:

$$A(\theta) = \frac{1}{4}(cos^4\theta + 4\, cos\theta\, sin^2\theta + cos2\theta). \tag{2.25}$$

Ideally, the resistance of an interferometer is proportional to the backscattering amplitude. Therefore, considering the magnetic field applied perpendicular to the interferometer, the total resistance

of the system results in:

$$R \propto \frac{1}{2} + A(\theta)\, cos\left(\frac{hB_{\perp}}{2eL^2}\right). \tag{2.26}$$

Experimentally, one observes both an oscillation with varied magnetic field $B_{\perp}$ and an oscillation with varied Rashba parameter $\alpha$. The actual value of $\alpha$ can be determined from the latter by using both Eq.(2.6) and Eq.(2.25). A plot of Eq.(2.25) in dependence of the precession angle $\theta$ is shown in Fig. 2.7. When determining the Rashba parameter, three points must be considered: first, traces must be recorded at various values of $\alpha$ so as to determine at least two maxima, minima or passes through zero. Second, a point of reference is required for $\alpha$, as AAS oscillations only provide relative values: a possible offset of $n \cdot \pi$ ($n$: signed integer) in $\theta$ cannot be ascertained. Third, a second point of reference for $\alpha$ is required to determine the *direction* of the dependence of $\alpha$ on an external value. As the amplitude of AAS oscillations as a function of the spin precession angle has many symmetry points, an increase or a decrease of $\alpha$ in dependence of an external parameter can only be ascertained with a second reference point. In gated samples, the points of reference can be obtained by means of WAL by depleting the sample into the regime of diffusive transport.

# 3 Processing and experimental techniques

To perform transport experiments, semiconductor systems in defined geometry are required. Samples in such defined geometries are made in a complex sequence of processing steps. This chapter briefly introduces the basic processing steps used in making samples and gives an overview of the experimental techniques used in low-temperature transport experiments.

## 3.1 Processing

The individual processing steps taken in the sequence of sample fabrication are simple. Most of these processing steps are common clean-room procedures, so that their description will be kept to a minimum here. Detailed parameters of all steps as well as full processing sequences can be found in Appendix A.

### Surface treatment

In heterostructures, the properties of the channel and the 2DEG are defined by the choice of materials and the sequence of layers. This is not possible in bulk p-type InAs, in which the 2DEG is located at the surface of the semiconductor (for details, see Section 4.1). However, the properties of the channel and 2DEG show a clear dependence on the condition of the surface [Mat94]. In its pristine state, the surface of p-type InAs is rough and dirtied with impurities. Due to this, the mobility of the 2DEG is reduced, and interface scattering occurs when current is passed to the semiconductor from metal surface-electrodes. Surface treatment is performed to reduce both roughness and the number of impurities at the surface. A two-step polishing process is used: first, the sample is mechanically polished with a suspension of 1 $\mu$m $Al_2O_3$ grains in $H_2O$. Then, chemical polishing with a solution of 0.025‰ Bromine in Methanol is performed. The polishing results in an average roughness of the interface of approximately one nm, excluding occasional grooves [Kür02].

### Lithography

At many different stages of sample processing, selective access to regions of a semiconductor is necessary. Lithography is the common method of patterning: the sample is coated with a sensitised resist which is subsequently exposed, either in an electron beam lithography system or with ultraviolet light in a mask aligner. In the former case, the exposure follows a CAD-designed mask according to which a computer controls the electron beam. In the latter case the sample is brought into contact with a shadow-mask, that contains a positive image of the desired pattern, and then is

exposed through the mask. In both cases the resist is developed after exposure. After developing, the sample surface is uncovered in the areas that were previously illuminated, while a protective layer of resist covers the remainder of the sample. However, despite developing, traces of resist remain in the illuminated areas. These are ashed by an oxygen plasma in a barrel reactor or by ozone in a UV ozone stripper. Processing steps following lithography only affect the areas of the sample not covered by the protective layer of resist. The resists used were NTT-AT's Φ-MAC for electron beam lithography and Shipley's S1813 for optical lithography.

## Deposition

Electrodes, leads, annealed contacts, and gates require materials to be deposited on samples. Two common techniques are available for deposition, thermal evaporation and DC-sputtering: in the former case, the required material is heated up to evaporation temperature in high vacuum. Heating is effected either by passing a current through a tungsten boat or by means of a high-power electron beam. Vapour of the material is then emitted from the heated source and condenses on the surface of the sample. In the case of sputter deposition, an Argon plasma is ignited above a fixed target of the required material. A DC electric field is used to accelerate $Ar^+$ ions towards the target. On impact, the ions cause material to sputter off the target and onto the sample surface[1]. Following deposition, a so-called lift-off procedure is performed: an organic solvent is used to wash away the resist remaining on the sample surface after lithography. This also washes away the deposited material on the resist, that is not in direct contact with the sample surface. In the regions previously illuminated in lithography, the desired material remains on the sample.
Both thermal deposition and sputtering can also be used to deposit gate oxides. However, a third method called Plasma Enhanced Chemical Vapour Deposition (PECVD) yields oxides of higher quality. To deposit e.g. $SiO_2$, a plasma of $SiH_4$ and $N_2O$ gas is ignited, from which $SiO_2$ condensates onto a heated sample surface. The plasma can be ignited either by a radio frequency electric field or by electron cyclotron resonance.

## Etching

When materials must be removed in a controlled way, as e.g. necessary to define a 2DEG into Hall-bar geometry, etching is used. The two commonly used methods are wet chemical etching and Reactive Ion Etching (RIE). Arsenide-based III-V semiconductors are wet-chemically etched by means of acidic solutions of either $H_3PO_4$:$H_2O_2$:$H_2O$, 1:10:100 or $C_6H_8O_7$(20%):$H_2O_2$(30%), 20:1. The latter solution is material-selective, as it does not etch InP[2]. In contrast, HCl:$H_3PO_4$:$CH_3COOH$:$H_2O$, 2:2:5:2 is used to selectively etch InP, as it does not affect As-based III-V semiconductors. $SiO_2$ gate oxides are wet chemically etched with diluted HF. In RIE, a gas plasma of etchant is ignited by a radio-frequency electric field. The ions of the plasma are then accelerated towards the sample surface by an additional DC field. Etching then functions as a combination of physical and chemical processes. A plasma of $BCl_3$ and $N_2$ gas is used to etch

[1] A good introduction to sputter processes can be found in [Pel03].
[2] Characterisation of the etch rates of $H_3PO_4$:$H_2O_2$:$H_2O$, 1:10:100 can be found in [dB03]

III-V semiconductors, and a plasma of $CHF_3$ gas is used to etch $SiO_2$. In contrast to wet chemical etching, RIE is a anisotropic technique that produces straight edges with no undercut. RIE is commonly used when precision is required, such as for small-dimensional structures like Hall-bars or interferometers. Wet chemical etching is used for larger structures such as connecting leads and bondpads.

### Connection of backgates

Ingrown backgates are difficult to connect. Care must be taken to prevent short-circuits with the channel positioned above the back-gate. Thus, direct connection by annealing is not possible. Some heterostructures used in this thesis feature a backgate that is located about 1.3 $\mu$m below the sample surface, i.e. about 1.2 $\mu$m below the channel. Wet chemical etching is used to remove the top 1.1 $\mu$m of the heterostructure in a corner of the sample, leaving about 200 nm of semiconductor remaining above the backgate. Then, using a second photolithographic step to prevent overlap with the channel, a mixture of gold, germanium, and nickel is deposited above the etched area. Finally, an ohmic contact to the backgate is made by annealing.

## 3.2 Low temperature magnetotransport experiments

In this thesis, the electronic properties of a 2DEG are studied in so-called *transport experiments*: a current is passed through the system and the resistance is measured in dependence of various externally applied conditions. All experiments are performed at temperatures of 4.2 K and below, using the following cooling systems: a conventional $^4$He cryostat with a variable temperature inset (VTI), reaching temperatures down to 1.5 K, a $^3$He cryostat, reaching temperatures down to 300 mK, and a $^3$He-$^4$He dilution refrigerator with a base temperature of about 15 mK.
Electrical contact to the samples is made in a standard four-point setup[3]: a small AC bias current is applied across the sample by means of two terminals. The voltage drop across two other terminals is recorded, using Stanford Research Systems SRS830 lock-in amplifiers. To observe small variations in voltage on a large background, such as in the measurements of WAL in heterostructures, the 'offset' and 'expand' functions of the lock-in amplifier are used. These subtract a background from the input signal before A/D conversion is performed, and then expand the measurement range [Sys]. The sample's resistance can be determined from the bias current and the voltage drop by means of Ohm's law. Magnetic fields $B$ of up to 12 Tesla are applied perpendicular to the sample surface, using superconducting magnets. In high field measurements, i.e. for $B > 200$ mT, the magnets are controlled by Oxford Instruments' IPS120 power supplies. In low field measurements, the magnets are driven either by an Advantest or by a Keithley 2400 low-noise current source. The latter two allow for resolutions better than 10 $\mu$T. Gate voltages are applied using either Yokogawa or Knick low-noise voltage sources. All equipment is controlled by means of software running within the framework of the *Object Bench* package by Oxford Instruments.

[3]Samples in Corbino geometry feature only two metallic contacts to the channel, source and drain. As these must simultaneously function as current leads and voltage probes, use of a four-point setup is not possible. However, starting from these contacts, separate wiring is used for current and voltage.

# 4 p-type InAs single crystals

Acceptor doped crystalline p-type InAs is an interesting material system for spin-related transport experiments: a 2DEG is formed at the crystal surface that exhibits no Schottky barrier to normal metal contacts. In addition, p-type InAs exhibits strong spin-orbit interaction. This chapter briefly introduces the material system and the sample geometry and then presents the results of transport experiments performed in low and high magnetic fields to determine the strength of spin-orbit interaction.

## 4.1 Material system

The p-type InAs single crystals used[1] are Zn doped at a nominal acceptor concentration of $2.0 \cdot 10^{17}$ cm$^{-3}$. A so-called electronic inversion layer is formed at the crystal surface. In this layer, the conduction band is below the Fermi energy so that electrons are the majority carriers. As is displayed in Fig. 4.1(a), this leads to a quantum well of approximately triangular shape [And82]. A roughly 10 nm deep 2DEG is formed, containing quantised energy levels arising from the confinement. For the doping concentrations and the gate voltages used, only the lowest subband in the quantum well is occupied. Higher subbands can be excited by applying high gate voltages, as is demonstrated in reference [Kür02]. The 2DEG is insulated from the bulk crystal by a depletion region of about 60 nm depth.
The large spin split-off of the p-type InAs valence band of $\Delta$=380 meV allows for strong spin-orbit interaction in the conduction band. Spin-orbit interaction arises from both SIA and BIA, whereby the former dominates and the latter can be neglected, as will be done in the following [dAeS94, Sch98]. The large SIA is caused both by the strong potential gradient and the unequal boundaries of the triangular quantum well [dAeS94, dAeS97].
Due to the small band gap of 418 meV (at T=4.2 K), the conduction band of InAs exhibits strong non-parabolicity. This non-parabolicity must be taken into account when determining the strength of spin-orbit interaction as it reduces the Rashba parameter, especially for higher carrier densities [Hu99]. In the simple approach used here, this can be achieved by means of a wave-vector dependent effective electron mass $m^*(k)$ [Sch04]. More extensive descriptions of band non-parabolicity, using a two level $k \cdot p$ approach, can be found in [Mer87, Mat00, Kür02].

[1] Samples supplied by Crystec, Berlin.

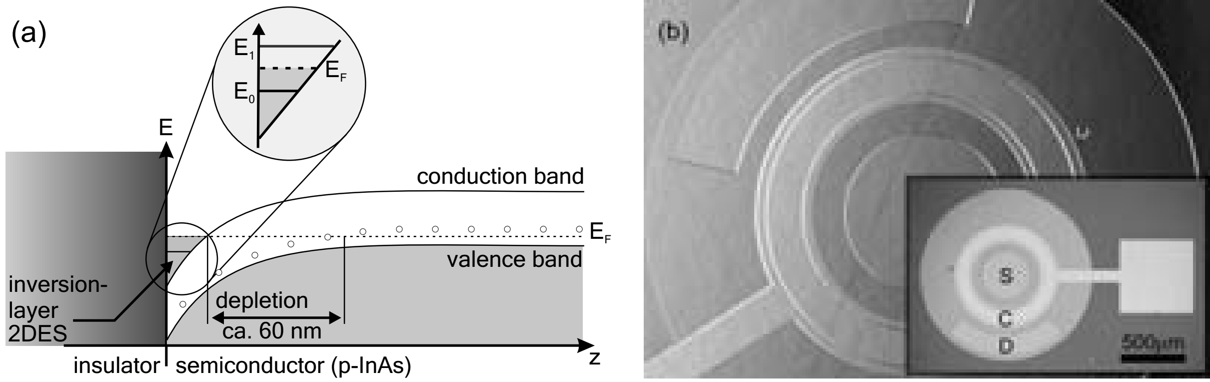


**Fig. 4.1:** (a) Band structure at the interface region of p-type InAs and an insulator. The blow-up shows the inversion layer, approximated by a triangular potential well, whereby $E_0$ and $E_1$ denote the lowest two electronic subbands in the well and $E_F$ denotes the Fermi energy. (b) Micrograph of the Corbino sample #1095-43. The main image shows the center section, the inset an overview of the transistor with source (S) and drain (D) electrodes, the ring-shaped channel (C) and the square gate bondpad. The inner source electrode has a radius of 300 $\mu$m, and the channel and the drain electrode have widths of 100 $\mu$m and 300 $\mu$m, respectively.

## 4.2 Sample geometry

A defined channel geometry as required for transport experiments cannot be obtained by etching of p-type InAs, as the entire surface is covered by a 2DEG. Instead of using Hall-bars, field-effect transistors are fabricated in so-called Corbino geometry [Cor11]. A circular inner source (radius: 300 $\mu$m) and a ring-shaped outer drain electrode (inner radius: 400 $\mu$m, outer radius: 700 $\mu$m) enclose a ring-shaped electron channel. This geometry gives rise to parabolic magnetoresistance in fields $B_\perp$ perpendicular to the device, described by[2]:

$$R_{geo}(B_\perp) = R_0(1+\mu^2 B_\perp^2). \tag{4.1}$$

A ring shaped metallic gate, interspaced by 350 nm of $SiO_2$, is positioned above the channel. By means of the field-effect, the potential gradient of the quantum well can be modified[3]. This allows for control of the strength of SIA, but also affects the carrier density. An image of a sample in Corbino geometry is shown in Fig. 4.1(b).

## 4.3 Experiments

The mobility of samples in Corbino geometry can be determined from their low-field magnetoresistance. In the classical regime, i.e. for magnetic fields $B_\perp < \mu$, and neglecting effects of weak localisation and antilocalisation, the low field magnetoresistance follows Eq.(4.1). By fitting experimental low-field magnetoresistance results with Eq.(4.1), the electron mobility $\mu$ was determined

[2] A derivation of this dependence can be found in reference [Sch01].
[3] A good graphic description of this is found in Fig. 2.2 in reference [Baa04].

to peak at 5000 cm$\frac{2}{\text{Vs}}$: the high concentration of acceptors as well as the roughness of the p-type InAs surface are the origin of the low mobility. This low mobility makes p-type InAs very suitable for weak localisation and antilocalisation experiments. However, measurements of SdH oscillations prove to be more challenging: oscillations can only be observed in high magnetic fields where they are wider spaced. Ideally, a full period of a beating pattern, i.e. the range between two nodes, is necessary to precisely obtain the spin-subband carrier densities by means of FFT. This is only the case at very high carrier densities, and only at these can the spin-splitting and thus the strength of spin-orbit interaction be gained by means of SdH. The methods used to determine the strength of spin-orbit interaction from SdH oscillations and from WAL are described in sections 2.2.2 and 2.3, respectively.
Low temperature magnetoresistance experiments are performed on field effect transistors patterned on p-type InAs in Corbino geometry. A voltage applied between gate and channel is used to modify the strength of SIA in the inversion layer. The associated inevitable change in carrier density is used to match the results of different samples studied. Both SdH oscillations and WAL are observed within the same cooling cycle for various gate voltages.
The SdH oscillations exhibit distinct beating patterns for higher carrier densities. By means of FFT analysis, non-zero Rashba spin-splitting is observed for carrier densities above $1.1{\cdot}10^{12}$ cm$^{-2}$. At lower carrier densities, the number of oscillations recorded is not sufficient for the FFT to yield a carrier density distribution, in which two peaks can be identified. Effects of WAL are observed for carrier densities as low as $4{\cdot}10^{11}$ cm$^{-2}$, whereby the strength of spin-orbit interaction parameter $\alpha$ can be determined for the entire carrier density range studied [Sch01].
The WAL traces are analysed by fitting the magnetoconductances with the theory of Hikami, Larkin, and Nagaoka [Hik80], which was the common theory for analysis of weak localisation effects at the time the experiment was performed. As briefly mentioned before, this theory only incorporates contributions to spin-splitting that are of the order of $k^3$, where $k$ is the electron wave vector. It does not correctly quantify effects linear in k, such as SIA, which are the dominant cause of spin-orbit interaction in InAs systems. However, relative changes in the Rashba parameter $\alpha$ are sufficiently described.
Comparison of the values for $\alpha$ obtained by analysis of SdH oscillations with those obtained by analysis of WAL with the theory by Hikami, Larkin, and Nagaoka show reverse trends: while the SdH data yields an increase in $\alpha$ with increasing carrier density, WAL gives the opposite dependence. These results are presented on the following pages in Paper A, which has been published in *Physica Status Solidi B* **233**, 436 (2002)[4].

[4]Reprinted with permission from Physica Status Solidi B **233**, 436 (2002), ©2002 by Wiley-VCH.

## Paper A

phys. stat. sol. (b) **233**, No. 3, 436–444 (2002)

# Weak Localization and Antilocalization in the Two-Dimensional Electron System on p-Type InAs

CH. SCHIERHOLZ[1]), R. KÜRSTEN, G. MEIER, T. MATSUYAMA, and U. MERKT

*Institut für Angewandte Physik und Zentrum für Mikrostrukturforschung, Universität Hamburg, Jungiusstr. 11, 20355 Hamburg, Germany*

(Received June 12, 2002; accepted July 22, 2002)

PACS: 72.20.–i; 73.20.Fz; 73.23.–b; 73.63.–b

We have performed low temperature magnetoresistance measurements of the two-dimensional electron system (2DES) in an inversion layer on p-type InAs. In high magnetic fields perpendicular to the 2DES beating patterns in Shubnikov–de Haas oscillations are observed from which the Rashba spin–orbit interaction parameter is determined. In the low-field regime we perceive weak localization and antilocalization. By fitting to the gathered localization data the elastic, inelastic, and spin relaxation times as well as coherence lengths for diffusive transport are determined for different applied gate-voltages. The Rashba parameter determined from these relaxation times is compared to the values obtained from the high-field Shubnikov–de Haas oscillations.

**1. Introduction** Use of the electron spin is a hot topic in the field of quantum computing as well as in spin electronics. The spin is used either as an additional degree of freedom or to substitute the charge degree of freedom [1, 2]. Many applications have been proposed, ranging from magnetic memory [3] over the spin-transistor proposed in 1990 by Datta and Das [4] to quantum computing with coupled spin-states [5]. The former has already been successfully demonstrated and industrial production is near. The implementation of the latter devices is one of the major fields of basic research in today's solid state physics.

The Datta and Das spin-transistor is a semiconductor spin analog to the electro-optical modulator. It is built up as a semiconductor–ferromagnet hybrid system, using ferromagnetic electrodes as spin-polarization injectors and detectors. Hereby the magnetization vector of the electrodes is parallel to the direction of electron transport as is depicted in Fig. 1a. Between the ferromagnetic source and drain contact the electrons ballistically pass through a semiconductor channel, their spin precessing due to spin–orbit interaction originating from the Rashba effect [6]. The source–drain current should be modulated by control of the spin orientation at the end of the semiconductor channel with respect to the magnetization vector of the drain electrode. The spin-precession angle $\Delta\theta = 2m^*\alpha L/\hbar^2$ between the source and drain electrode is a function of the gate-voltage dependent Rashba parameter $\alpha$, the effective electron mass $m^*$, and the channel length $L$ [4].

Current research activities contributing to the development of such a device include improvements in growth and design of high-mobility 2DES, especially in narrow-band III–V semiconductors [7–9] as well as the investigation of spin-polarization control via the Rashba effect in the 2DES channel [10–12]. Theoretical considerations stress the role of the ferromagnet/semiconductor boundary [13–15]. The prevalent experimental means to analyze spin-control are either optically or transport at high external magnetic

[1]) Corresponding author; e-mail: cschierh@physnet.uni-hamburg.de

phys. stat. sol. (b) **233**, No. 3 (2002) 437

fields. Optical experiments include the investigation of spin-injection from ferromagnets into semiconductor channels [16–18] as well as measurements of spin coherence lengths [19, 20] in the semiconductor. In transport measurements, a widely-used method to determine spin–orbit interaction in semiconductors currently is the evaluation of beating patterns in Shubnikov–de Haas (SdH) oscillations.

In addition to SdH measurements we have recorded weak localization and antilocalization as a function of an applied gate-voltage in inversion layers on p-type InAs single crystals. We use the localization to determine elastic, inelastic, and spin relaxation times as well as the strength of spin–orbit interaction, expressed in form of the Rashba-parameter $\alpha$ in the limit of low external fields ($B_{\text{ext}} \leq 400$ mT). We compare the data with that determined from high-field Shubnikov–de Haas measurements on the same sample. At this point we would like to mention the difficulties concerning the parameter $\alpha$. A distinct model of the semiconductor band structure must be assumed to extract the coupling strength from experimental data, thus giving rise to an uncertainty. For example, the consideration of non-parabolicity in the band structure can result in a change of the Rashba-parameter by approximately a factor of two [10]. However, since this parameter is the established means of comparison for spin–orbit coupling in semiconductors in the presence of asymmetric macroscopic potentials, we will use it to discuss and compare our experimental low- and high-field results.

Weak localization originates from interference between time-reversed trajectories of the conduction electrons and leads to a negative magnetoresistance in low fields [21]. In the presence of spin-dephasing the constructive interference is transformed into destructive interference and so weak localization is turned into antilocalization, causing a positive magnetoresistance for near-zero fields followed by the negative magnetoresistance of localization with increasing field (cf. the solid curve in Fig. 2). Analysis of

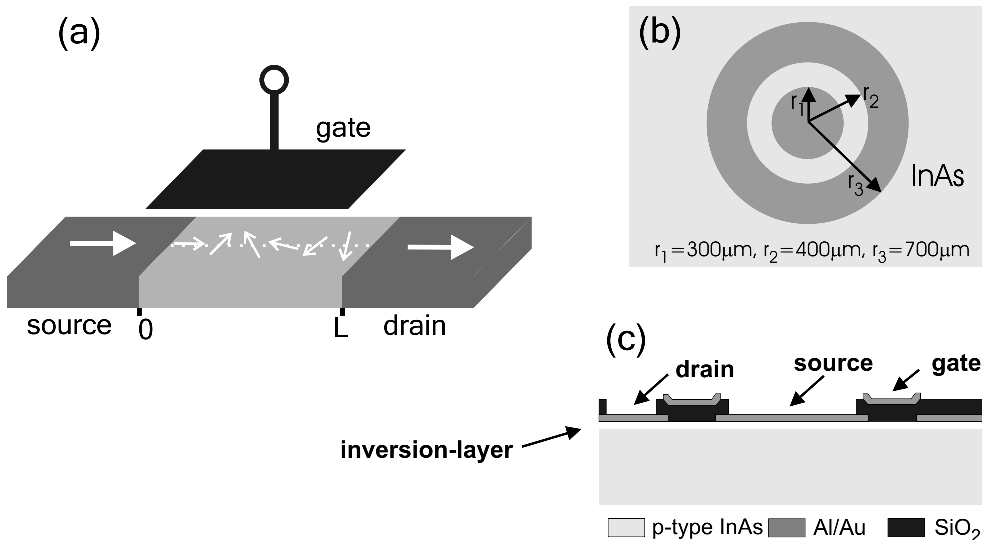


Fig. 1. a) Ballistic spin transistor as proposed by Datta and Das [4]. Two ferromagnetic electrodes at either end of a 2DES act as spin-polarization injector and detector. The spin precesses in the 2DES channel of length $L$ due to the Rashba effect with a gate-voltage dependent frequency. Scheme b) and cross-section c) of the sample in Corbino geometry used in the localization experiments. The inner circle represents the source contact, the outer ring the drain

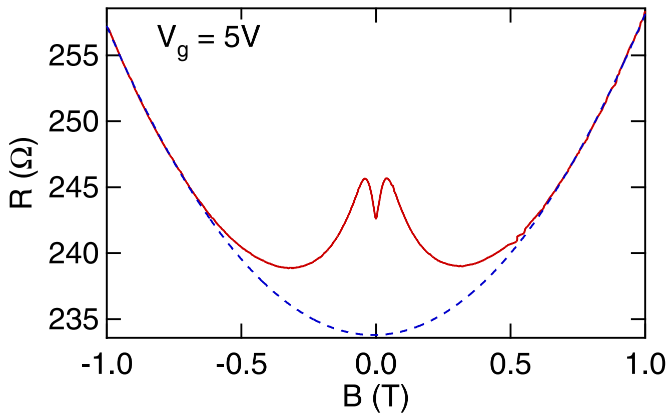


Fig. 2. (online colour). Raw experimental data (solid line) for a gate-voltage of $V_g = 5$ V is fitted with the classical Drude-magnetoresistance parabola (dashed line)

localization according to [22] has been used to characterize spin–orbit interaction in GaAs- and InAs-heterostructures [23, 24] as well as in InAs single crystals [25], whereby at the time of writing of the latter article the observed effects could not be understood sufficiently in theory.

In this paper we show measurements of SdH oscillations, including beating patterns as well as measurements of weak localization and antilocalization, then compare the Rashba-parameters obtained by the two methods. Finally we present an outlook.

**2. Samples** The samples used to measure weak localization and antilocalization are based on p-type InAs (100) single crystals doped with Zn at a concentration of $2.0 \times 10^{17}$cm$^{-3}$. A two-dimensional electron system (2DES) that does not form a Schottky-barrier to metals [26, 27] exists at the surface of this material [28]. The 2DES is confined in an approximately triangular potential well, the inclination of which, and thereby the surface electric field, is controllable by a gate-voltage. The Rashba spin–orbit coupling parameter is expected to be proportional to the surface electric field, thus permitting control of the spin–orbit interaction via a gate-voltage [29].

After mechanical and 'bromine in methanol' chemical polishing of the InAs surface the electrodes of a field-effect transistor (FET) in Corbino geometry are patterned by optical lithography and thermal evaporation in a so-called 'lift-off' process. The electrodes consist of a 35 nm Al layer protected by a 10 nm Au cap, whereby the circular source electrode has a diameter of 300 μm, the ring shaped drain electrode inner and outer diameters of 400 μm and 700 μm, respectively, as can be seen in Figs. 1b and c. The semiconductor channel between the electrodes has a length of 100 μm. An Al/Au gate electrode is placed above the channel, insulated from this by a 340 nm thick $SiO_2$ layer deposited by plasma-enhanced chemical vapor deposition (PECVD).

All measurements are performed in a $^4$He evaporation cryostat at a temperature of 2.65 K. In the localization measurements the sample is biased with a constant current $I_{bias} = 10$ μA. The lock-in response to a superposed modulated bias current of amplitude 10 μA and frequency 3.33 kHz is recorded for various gate-voltages. In the SdH measurements the response to a gate-voltage modulation of amplitude 0.5 V and frequency 377 Hz at a constant bias current of 10 μA provided better results.

Samples in Corbino principally geometry exhibit a parabolic Drude magnetoresistance of $R_D(B) = R_0(1 + \mu^2 B^2)$ with $R_0$ being the zero-field resistance and $\mu$ the mobility. To specify the quantum corrections to the magnetoresistance caused by weak localization and antilocalization, this Drude term must be determined and subtracted from the experimental data. This is performed by fitting parabolas with the characteristics described by the equation above to the measured magnetoresistance under consideration of data taken at external magnetic fields of $B_{ext} \geq 0.6$ T only, so as to exclude localization effects. A so determined parabola as well as the corresponding raw experimental data are depicted in Fig. 2. Subsequently the obtained $R_D(B)$ is subtracted from the experimental data so that only the contributions of weak localization and antilocalization remain.

**3. Shubnikov–de Haas Measurements** The Rashba Hamiltonian $\hat{H}_R = \alpha(\sigma \times \mathbf{k}) \cdot \hat{e}_z$ includes the Rashba parameter $\alpha$, the Pauli spin matrices $\sigma$, the electron wave vector $\mathbf{k}$, and the unit vector $\hat{e}_z$ perpendicular to the plane of the 2DES [6]. It causes a splitting of the degenerate conduction electrons into spin subbands occupied by electrons with densities $n_s^+$ and $n_s^-$, respectively. The distinct densities cause beating patterns in the SdH oscillations in quantizing magnetic fields perpendicular to the plane of the 2DES. Fast Fourier Transforms (FFT) reveal the densities $n_s^\pm$ from which the Rashba parameter can be deduced [10, 12, 30].

Beating patterns in the SdH oscillations can clearly be observed in Fig. 4a for gate-voltages of $V_g = 28$ V and above. The corresponding carrier concentrations are depicted in Fig. 4b, the double-peaks representing twice the carrier concentrations $n_s^\pm$. As mentioned before, the spin-splitting can be tuned by an external gate-voltage $V_g$. It is directly connected with the subband carrier concentration according to $\Delta k = k_F^+ - k_F^- = \sqrt{2\pi n_s^+} - \sqrt{2\pi n_s^-}$, assuming only the ground subband to be populated, so that an increase of spacing between the separate peaks of the double-peak structure corresponds to an increase in spin-splitting. Such an increase of peak spacing in dependence of the gate-voltage can be observed in Fig. 4b.

The difference of the wave vectors $\Delta k$ of the two Fermi circles of the two populations $n_s^\pm$ has been evaluated for various samples and sample geometries under consid-

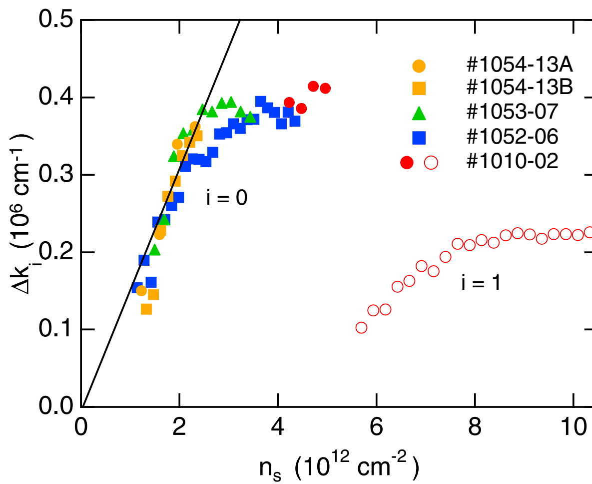


Fig. 3. (online colour). Splitting $\Delta k_i$ of the wave vectors of the Fermi circles due to the Rashba effect as a function of the total carrier density, determined by analysis of SdH beating patterns. The index $i$ denotes the electron subband

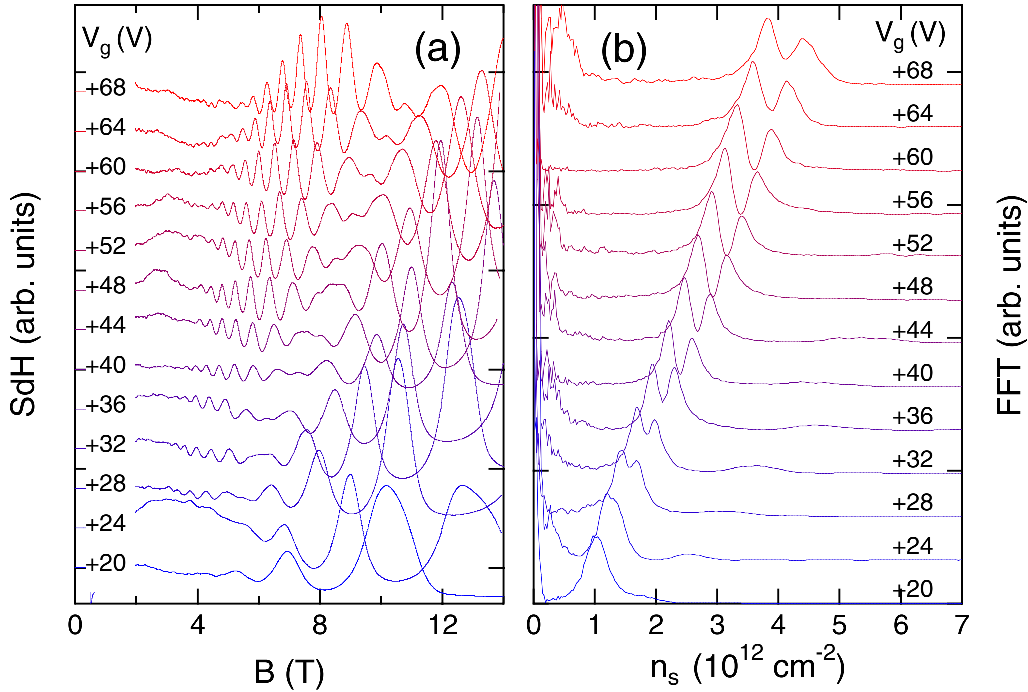


Fig. 4. (online colour). a) Shubnikov–de Haas measurements at various gate-voltages $V_g$ at $T = 2.65$ K measured as derivatives of the magnetoresistance (offset for clarity). Beating patterns can be observed for voltages of $V_g = 28$ V and above. b) Fast Fourier Transforms (FFT) of the data in a) versus the total electron density $n_s$

eration of subband nonparabolicity [10, 31] as is displayed in Fig. 3. The spin-splitting increases for carrier densities up to approximately $n_s \cong 2.5 \times 10^{12}$ cm$^{-2}$ and then approaches a maximum value $\Delta k \cong 0.37 \times 10^6$ cm$^{-1}$. The solid line indicates the linear approximation of $\Delta k$ vs. $n_s$ with a slope of $1.55 \times 10^{-7}$ cm valid in the regime of low carrier concentration. At high gate-voltages the first excited subband ($i = 1$) is populated in the sample #1010-02 with an acceptor concentration of $N_A = 2.0 \times 10^{17}$ cm$^{-3}$, qualitatively exhibiting the same behavior as the $i = 0$ subband.

**4. Localization Measurements** Beating patterns in the SdH oscillations can only be observed at high magnetic fields due to the then strong splitting $\Delta k$. Weak localization and antilocalization provide a method to determine spin-splitting at low magnetic fields and without the restrictions imposed by a technically limited magnetic field strength in SdH measurements.

Weak localization occurs due to constructive interference between time-reversed closed electron paths. In the absence of spin-related phenomena this interference is constructive, thus enhancing the probability of electron backscattering and leading to an increase in resistance. In the presence of spin-dephasing this constructive interference is turned into destructive interference which in return decreases the resistance. External magnetic fields applied orthogonally to the plane of transport destroy time-reversal symmetry as the phase picked up by electrons moving along the closed paths

in opposite directions have opposing signs. As a consequence, when increasing the magnetic field strength from zero one at first observes an increasing resistance stemming from the suppression of antilocalization followed by an decreasing resistance due to the destruction of localization. This can be observed for the raw experimental data in Fig. 2 (solid line).

The quantum corrections to the conductance caused by weak localization and antilocalization can be described by [22].

$$\Delta G(B) = \frac{-e^2}{2\pi^2\hbar}\left\{\Psi\left(\frac{1}{2}+\frac{B_e}{B}\right) - \Psi\left(\frac{1}{2}+\frac{B_2}{B}\right) + \frac{1}{2}\left[\Psi\left(\frac{1}{2}+\frac{B_i}{B}\right) - \Psi\left(\frac{1}{2}+\frac{B_4}{B}\right)\right]\right\}, \quad (1)$$

whereby $B$ denotes the external magnetic field and $\Psi$ the digamma function. The fields $B_2$ and $B_4$ are $B_2 = B_i + B_{so}$ and $B_4 = B_i + 2B_{so}$ for a 2DES [23]. The characteristic fields of the elastic, inelastic, and spin–orbit dephasing processes $B_\alpha$ ($\alpha$ = e, i, so) are connected with the respective scattering times $\tau_\alpha$ as

$$B_\alpha = \frac{\hbar}{4De\tau_\alpha} = \frac{\hbar}{2v_F^2 e\tau_e\tau_\alpha}, \quad (2)$$

$D = \frac{1}{2}v_F^2\tau_e$ being the diffusion constant and $v_F$ the Fermi-velocity. The measured conductance corrections were fit with Eq. (1), accounting for parallel conductances not influenced by localization by adding an additional constant $G_0$. Furthermore, in the fitting procedure a weighting that decreases the significance of the experimental data with increasing magnetic field-strength is performed. The result of this procedure is shown in Fig. 5 for six different gate-voltages. Under the condition, that the dominant spin-dephasing mechanism is Dyakonov–Perel scattering [32], the Fermi-surface average of the conduction-band spin splitting is given by [23]

$$\langle \Delta E_c^2 \rangle = \frac{4\hbar^2}{\tau_{so}\tau_e}. \quad (3)$$

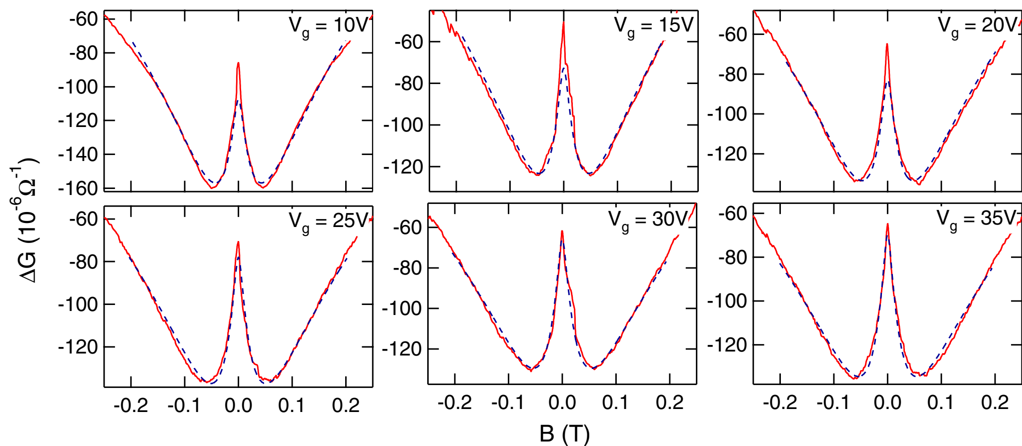


Fig. 5. (online colour). Magnetoconductance measurements of weak localization for various gate-voltages (solid lines) and fits according to Eq. (1) (dashed lines). The Drude contribution to the conductivity has already been subtracted

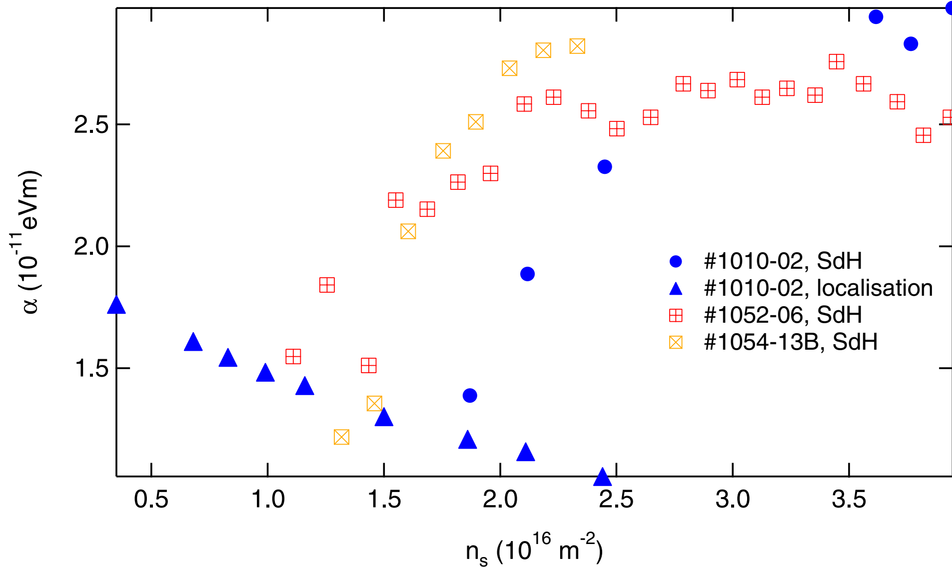


Fig. 6. (online colour). Rashba spin–orbit parameter $\alpha$ as a function of the total carrier density $n_s$. The square and circular symbols represent parts of data obtained via the analysis of SdH beating patterns using a non-parabolic subband approach [31], whereby the circular data is for the sample on which the localization measurements are performed. The triangular symbols represent data obtained from localization analysis. The SdH data for sample #1010-02 seems to be shifted to higher carrier densities as opposed to the SdH data of the other samples. This is probably due to a threshold-shift of the inversion layer

Using the approximation $\Delta E_c = \sqrt{\langle \Delta E_c^2 \rangle}$, the equation [4] $\Delta E_c = 2\alpha k_F$, and the relation $k_F = \frac{m^* v_F}{\hbar}$ with the Fermi velocity $v_F = \frac{1}{\hbar}\frac{\partial E}{\partial k}$, the Rashba parameter can be determined. For this purpose carrier-concentration dependent effective electron masses $m^*$ determined by cyclotron resonance [33] were used. Rashba parameters obtained by analysis of SdH beating patterns and by localization analysis are displayed in Fig. 6 as functions of the carrier density. An in principle opposite dependence of $\alpha$ on the carrier density can be observed for the low-field data obtained by localization analysis as opposed to the high-field data obtained by SdH measurements. Since the Rashba parameter describes the strength of the spin–orbit interaction, its decrease with increasing carrier density is a surprising feature. We also note, that the extrapolation of the parameters determined by SdH analysis for $n_s \to 0$ even leads to negative values. The most probable origin of these results is due to reaching the limitations of the linear approximation $\Delta E_c = 2\alpha k_F$. For the strongly non-parabolic semiconductor InAs higher order terms should be taken into account to achieve a more reliable evaluation of experimental data [34].

The determined relaxation times are in the range of $\tau_e \simeq 0.09 \times 10^{-12}$ s, $\tau_i \simeq 2.4 \times 10^{-12}$ s, and $\tau_{so} \simeq 0.8 \times 10^{-12}$ s for a gate-voltage of $V_g = 10$ V. We find a decrease of $\tau_e$ and $\tau_{so}$ as well as an approximately constant $\tau_i$ with the gate-voltage. The decrease of $\tau_e$ can be understood in terms of enhanced scattering at the InAs/$SiO_2$ boundary [35], the decrease in $\tau_{so}$ at the same time due to an increase in spin–orbit interaction concomitant with the strength of the surface electric field. The ballistic co-

phys. stat. sol. (b) **233**, No. 3 (2002) 443

herence length is estimated as $L_e \simeq 55$ nm as product of the elastic relaxation time $\tau_e$ and the Fermi-velocity, the latter calculated according to the subband structure described in [31]. The diffusive coherence lengths are calculated according to [21] and result as $L_{e,diff} \simeq 40$ nm, $L_{i,diff} \simeq 206$ nm, and $L_{so,diff} \simeq 123$ nm at $V_g = 10$ V.

**5. Conclusion and Outlook** We have presented a method to determine relaxation times and coherence lengths at near-zero magnetic fields. As all proposed spintronic devices operate at low or zero external magnetic fields the spin–orbit interaction in this case is important. We note and discuss the discrepancy to SdH beating pattern analysis, which are high-field measurements. The spin–orbit interaction parameter $\alpha$ was determined with both methods, and the results were compared. In both cases a tunability of $\alpha$ was observed, confirming that spin–orbit interaction in 2DES in InAs can be tuned by applying a gate-voltage. A spin-transistor with ferromagnetic permalloy electrodes based on the semiconductor discussed in this article hints at tunable spin–orbit interaction in a hybrid device [36], thus supporting our findings.

***Acknowledgements*** The authors would like to thank T. Koga, J. Nitta, and H. Takayanagi at NTT basic research laboratories for valuable discussions and R. Winkler at the University Erlangen for theoretical support. We gratefully acknowledge financial support from the DFG via SFB 508 “Quantenmaterialien” and from the NEDO joint research program.

## References

[1] G. Prinz, Phys. Today **48** (4), 58 (1995).
[2] S.A. Wolf et al., Science **294**, 1488 (2001).
[3] P. Ball, Nature **404**, 918 (2000).
[4] S. Datta and B. Das, Appl. Phys. Lett. **56**, 665 (1990).
[5] D. Loss and D.P. DiVincenzo, Phys. Rev. A **57**, 120 (1998).
[6] E.I. Rashba and Yu. A. Bychkov, J. Phys. C **17**, 6039 (1984).
[7] H. Hardtdegen et al., J. Appl. Phys. **73**, 4489 (1993).
[8] T. Akazaki, J. Nitta, H. Takayanagi, T. Enoki, and K. Arai, Appl. Phys. Lett. **65**, 1263 (1994).
[9] A. Richter, M. Koch, T. Matsuyama, Ch. Heyn, and U. Merkt, Appl. Phys. Lett. **77**, 3227 (2000).
[10] T. Matsuyama, R. Kürsten, C. Meissner, and U. Merkt, Phys. Rev. B **61**, 15588 (2000).
[11] J. Nitta, T. Akazaki, H. Takayanagi, and T. Enoki, Phys. Rev. Lett. **78**, 1335 (1997).
[12] G. Engels, J. Lange, Th. Schäpers, and H. Lüth, Phys. Rev. B **55**, 1958 (1997).
[13] D. Grundler, Phys. Rev. Lett. **86**, 1058 (2001).
[14] D. Grundler, Phys. Rev. B **63**, 161307 (2001).
[15] T. Matsuyama, C.-M. Hu, D. Grundler, G. Meier, and U. Merkt, Phys. Rev. B **65**, 155322 (2002).
[16] H.J. Zhu, M. Ramsteiner, H. Kostial, M. Wassermeier, H.-P. Schönherr, and K.H. Ploog, Phys. Rev. Lett. **87**, 016601 (2001).
[17] A.T. Hanbicki, B.T. Jonker, G. Itskos, G. Kioseoglou, and A. Petrou, Appl. Phys. Lett. **80**, 1240 (2002).
[18] V.F. Motsnyi et al., Appl. Phys. Lett. **81**, 265 (2001).
[19] D. Hägele, M. Oestreich, W.W. Rühle, N. Nestle, and K. Eberl, Appl. Phys. Lett. **73**, 1580 (1998).
[20] I. Malajovich, J.J. Berry, N. Samarth, and D.D. Awschalom, Nature **411**, 770 (2001).
[21] S. Datta, Electron Transport in Mesoscopic Systems, Cambridge University Press, 1995.
[22] S. Hikami, A.I. Larkin, and Y. Nagaoka, Prog. Theor. Phys. **63**, 707 (1980).
[23] P.D. Dresselhaus, C.M.A. Papavassiliou, R.G. Wheeler, and R.N. Sacks, Phys. Rev. Lett. **68**, 106 (1992).

[24] G.L. Chen, J. Han, T.T. Huang, S. Datta, and D.B. Janes, Phys. Rev. B **47**, 4084 (1993).
[25] Y. Kawaguchi, I. Takayanagi, and S. Kawaji, J. Phys. Soc. Jpn. **56**, 1293 (1987).
[26] C.A. Mead and W.G. Spitzer, Phys. Rev. **134A**, 713 (1964).
[27] U. Kunze, Z. Phys. B **76**, 463 (1989).
[28] T. Ando, A. Fowler, and F. Stern, Rev. Mod. Phys. **54**, 437 (1982).
[29] E.A. de Andrada e Silva, G.C. la Rocca, and F. Bassani, Phys. Rev. B **50**, 8523 (1994).
[30] D. Grundler, Phys. Rev. Lett. **84**, 6074 (2000).
[31] U. Merkt and S. Oelting, Phys. Rev. B **35**, 2460 (1987).
[32] M.I. Dyakonov and V.I. Perel, Sov. Phys. — JETP **33**, 1053 (1971).
[33] J. Nehls, Thesis, University of Hamburg, Shaker Verlag, 1996.
[34] R. Winkler and U. Rössler, Phys. Rev. B **48**, 8918 (1993).
[35] T. Matsuyama, Thesis, University of Hamburg, Shaker Verlag, 1994.
[36] G. Meier, T. Matsuyama, and U. Merkt, Phys. Rev. B **65**, 125327 (2002).

## Paper B

Lamari and Winkler calculated the strength of zero-field spin-splitting $\Delta_0$ and the Rashba spin-orbit interaction parameter $\alpha$ for inversion layers on p-type InAs single crystals with multi-band $k \cdot p$ theory [Lam01, Win01]. The doping concentrations and carrier densities that were used are comparable to those of our samples. An increase of $\Delta_0$ and a decrease of $\alpha$ are predicted for increasing carrier density. Qualitatively, the calculations agree with the values obtained in the previous section by analysis of WAL with the Hikami, Larkin, and Nagaoka theory. The absolute values however differ, as the experimentally determined Rashba parameter is smaller and shows a stronger dependence on the carrier density than the calculated one.

When SIA is the dominant origin of zero-field spin-splitting, WAL is correctly described by the theory of Iordanskii, Lyanda-Geller, and Pikus (ILP) introduced in Section 2.3.2. This is achieved by accounting for linear terms in the wave-vector $k$. ILP theory was used to analyse the WAL data and implemented into the IGOR Pro data analysis package by means of an XOP, the source code of which can be found in Appendix B. Experimental data was fit with this, using the least-squares method. The resulting values for $\Delta_0$ and $\alpha$ coincide very well with the results of Lamari and Winkler.

As mentioned in the previous section, Rashba parameters determined by SdH and by WAL show opposite dependence on the carrier density. The Rashba parameter is determined from the SdH oscillations by means of the two spin-split subband carrier densities, as described in Eq. (2.16). When performing this with the spin-subband carrier densities calculated by Lamari, agreement with the directly calculated value for $\alpha$ is obtained. Doing so with the spin-subband carrier densities gained from SdH oscillations yields not only a larger value for the Rashba parameter, but also a stronger dependence on the total carrier density. The cause is currently not understood, but may lie in the high carrier densities found in single crystals. Possibly, the high external magnetic fields applied to observe SdH oscillations also affect the strength of zero-field spin-splitting [Lom88, Luo90]: experiment and theory have been found to agree well for some heterostructures, in which carrier densities are lower than in single crystals and beating patterns can be observed at lower magnetic fields due to the high mobility [Nit97, Eng97]. The results of these investigations are presented in Paper B which has been published in *Physical Review B* **70**, 233311 (2004)[5].

[5]Reprinted with permission from Physical Review B **70**, 233311 (2004), ©2004 by the American Physical Society.

PHYSICAL REVIEW B **70**, 233311 (2004)

# Weak localization and spin splitting in inversion layers on *p*-type InAs

Christopher Schierholz,* Toru Matsuyama, Ulrich Merkt, and Guido Meier
*Institut für Angewandte Physik und Zentrum für Mikrostrukturforschung, Universität Hamburg, Jungiusstrasse 11, D-20355 Hamburg, Germany*
(Received 2 August 2004; published 21 December 2004)

We report on the magnetoconductivity of quasi-two-dimensional electron systems in inversion layers on *p*-type InAs single crystals. In low magnetic fields pronounced features of weak localization and antilocalization are observed. They are almost perfectly described by the theory of Iordanskii, Lyanda-Geller, and Pikus. This allows us to determine the spin splitting and the Rashba parameter of the ground electric subband as a function of the electron density.

DOI: 10.1103/PhysRevB.70.233311 PACS number(s): 72.20.Fr, 72.25.Rb

The multitude of new applications promised by use of the electron's spin as a degree of freedom in addition to its charge has led to growing interest in the area of spintronics.[1] For semiconductor based spintronics, the required control of the electron spin is expected to be achieved via spin-orbit interaction. In single crystals this interaction originates from two terms: the bulk inversion asymmetry of the crystal lattice[2] and the structure inversion asymmetry.[3] The latter term includes contributions from the electric field and from the boundary conditions and is commonly called Rashba term. For many heterostructures good agreement between calculated Rashba parameters and experimentally deduced values is reached.[4,5] In the case of two-dimensional electron systems (2DES) in surface inversion layers the spin-orbit interaction and the Rashba parameter are still under debate.[6–8]

Theoretical considerations[9,10] have shown that the Rashba term is the main cause of the spin splitting of electric subbands in InAs structures. This is supported by the experiments of Luo *et al.* on InAs quantum wells.[11] It has been demonstrated for various heterostructures[4,12,13] as well as for inversion layers on *p*-type InAs single crystals[6] that the Rashba term can be influenced by an external gate voltage. This was concluded from beating patterns in Shubnikov-de Haas (SdH) oscillations at various gate voltages. However, contrary to SdH experiments, all proposed spintronic devices operate at zero or low magnetic fields. Calculations by Lommer *et al.* showed that not only the magnitude but even the sign of the spin splitting can change between low and high magnetic fields for AlGaAs/GaAs heterostructures.[9] For spintronic applications it is thus necessary to determine the spin splitting at near-zero magnetic fields.

Dresselhaus *et al.*[14] showed that the destruction of weak antilocalization by small magnetic fields can be used to determine the strength of the spin-orbit interaction in GaAs. These authors analyzed their data with the theory of Hikami, Larkin, and Nagaoka.[15] Kawaguchi *et al.*[16] found that this theory could not correctly reproduce the weak antilocalization observed in inversion layers on *p*-type InAs. Koga *et al.*[5] showed that a quantitative description of weak antilocalization in InAlAs/InGaAs/InAlAs heterostructures is possible with the model developed by Iordanskii, Lyanda-Geller, and Pikus (ILP).[17,18] Analyses of weak antilocalization using ILP theory have been performed on AlGaAs/AlInAs quantum wells,[18] AlGaAs/GaAs *p*-type quantum wells,[19] and AlInAs/GaInAs/AlInAs quantum wells.[5] However, this approach so far has not been used to analyze the magnetoconductance of 2DES on bulk narrow-gap semiconductors.

We have performed measurements on Zn doped *p*-type InAs (100) single crystals with an acceptor concentration of approximately $N_A = 2 \times 10^{17}$ cm$^{-3}$. Band bending leads to a 2DES confined in the approximately triangular asymmetric potential well characteristic of a natural surface inversion layer.[20] The narrow band gap of InAs results in strong spin-orbit interaction, with the Rashba term that originates from the asymmetry of the potential well dominating the spin splitting of the electric subbands.[9] Our samples are field-effect transistors in Corbino geometry. The electrodes are defined by optical lithography and deposited by thermal evaporation. They consist of 35 nm thick aluminum passivated by 10 nm of gold. The entire structure is covered by a 340 nm thick $SiO_2$ insulator onto which a gate covering the semiconductor channel is patterned. All measurements are performed in lock-in technique at a temperature of 2.65 K in a $^4$He cryostat.

The measured magnetoconductances show strong parabolic signatures as can be seen for fields above 300 mT in Fig. 1(a). This classical Drude magnetoconductivity $G(B) = G_0(1+\mu^2 B^2)^{-1}$ stems from the Corbino geometry

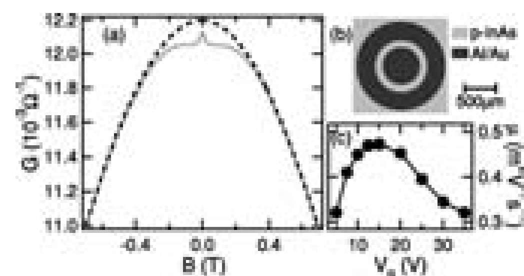


FIG. 1. (a) Experimental magnetoconductance for a gate voltage of $V_g = 15$ V at $T = 2.65$ K (solid line) as well as a calculated Drude parabola (dashed line). (b) Schematic of the sample geometry. The radius of the inner electrode is 300 $\mu$m, the channel length 100 $\mu$m, and the radius of the outer electrode 700 $\mu$m. (c) Electron mobility versus gate voltage.

 ©2004 The American Physical Society

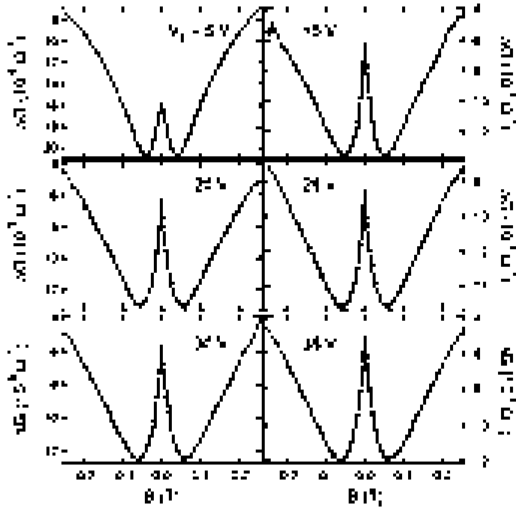

FIG. 2. Experimental magnetoconductances recorded at 2.65 K for various gate voltages (solid lines). The classical Drude conductance is subtracted. Theoretical conductances (dashed lines) are calculated from the theory of Iordanskii, Lyanda-Geller, and Pikus (Refs. 17 and 18).

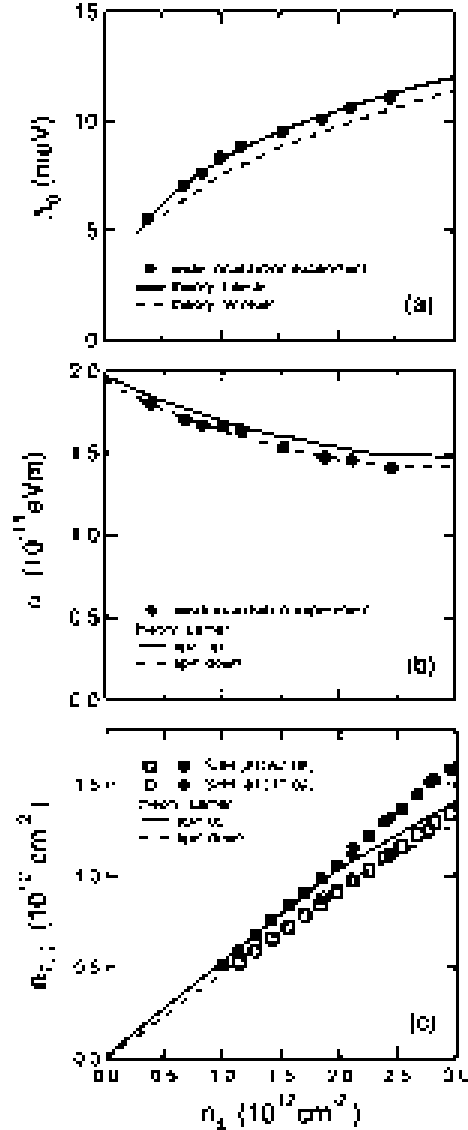


FIG. 3. (a) Spin-splitting energy at the Fermi level. Theoretical data are taken from Lamari (Ref. 22) and Winkler (Ref. 23). (b) Rashba parameter. Dashed and solid lines are calculated for the spin-split subbands at the Fermi level (Ref. 22). (c) Occupation of the spin-split subbands. Open and closed symbols are data for spin-down and spin-up states of the two different samples indicated by circles and squares. Theoretical curves are taken from Lamari (Ref. 7).

depicted in Fig. 1(b). A parabola fit to the experimental data yields the zero-field conductivity $G_0$ as well as the electron mobility $\mu$. The mobility as a function of the applied gate voltage is shown in Fig. 1(c). It is characteristic for a metal-oxide-semiconductor (MOS) transistor: surface scattering at low gate voltages and ionized impurity scattering at high gate voltages lead to reduced mobilities.[20] The inversion threshold of the sample lies at a gate voltage of $V_g \cong 1.8$ V. The total electron density $n_s$ is determined from SdH oscillations of the source-drain resistance. We find a linear dependence $n_s[\text{cm}^{-2}] = 1.46 \times 10^{11} + 6.70 \times 10^{10}\, V_g[\text{V}]$ on the gate voltage.

The Drude parabola is subtracted from the magnetoconductance to leave the quantum corrections originating from weak localization and antilocalization remaining. Starting from zero-field, these corrections at first exhibit a negative magnetoconductance originating from spin-orbit interaction based weak antilocalization followed by a positive magnetoconductance due to weak localization. Figure 2 shows results for various gate voltages. The conductance corrections $\Delta G(B)$ are fit according to the ILP theory which provides an excellent description. Considering the structure inversion asymmetry as dominant origin of the zero-field spin splitting in our system and thus neglecting the bulk inversion asymmetry ($\Omega_3 = 0$ in Refs. 17 and 18), only the characteristic magnetic fields of inelastic and of spin-orbit scattering,

$$H_\phi = \frac{\hbar}{4De\tau_\phi} \quad \text{and} \quad H_{\text{SO}} = \frac{\Delta_0^2 \tau_{\text{tr}}}{8\hbar De} = \frac{1}{8\hbar^3 e\pi} \frac{(m^* \Delta_0)^2}{n_s} \tag{1}$$

are relevant in the fitting procedure.[18] In these relations $D$ is the diffusion coefficient, $\tau_\phi$ and $\tau_{\text{tr}}$ are the inelastic and transport relaxation times, respectively, and $\Delta_0$ is the spin-splitting energy in zero magnetic field. The characteristic field $H_{\text{tr}}$ of transport scattering can be ignored in the fit as it only results in a shift in $\Delta G(B)$.[5,18] The diffusion coefficient is given by $D = \tau_{\text{tr}} v_F^2/2$ with the Fermi velocity $v_F = \hbar k_F/m^*$, the Fermi wave vector $k_F$, and the electron effective mass $m^*$.

We calculate the zero-field spin splitting $\Delta_0$ from Eq. (1) and the Rashba parameter from the relation[5]

$$\alpha = \frac{\sqrt{\hbar^3 e H_{SO}}}{m^*}. \quad (2)$$

Note that only the absolute value of the Rashba parameter can be determined, not its sign. In the case of inversion layers we do not expect a change of sign as their asymmetric surface potentials do not change their overall shape. The analysis is performed for the effective mass $m^*$ of the ground electric subband at the Fermi energy. For high carrier densities $n_s$ this mass is determined from temperature dependent SdH oscillations. At the inversion threshold the band edge mass of the ground subband of $m_0^* = 0.026 \cdot m_e$ is used.[21] Hence we find

$$m^* = (0.026 + 0.012 \times 10^{-12}\, n_s - 0.001 \times 10^{-24}\, n_s^2) \cdot m_e, \quad (3)$$

with the electron density $n_s$ in units of $cm^{-2}$.

Figure 3(a) shows the carrier-density dependence of the spin-splitting energy $\Delta_0$. The splitting increases monotonically with the electron density $n_s$ and is in good agreement with band-structure calculations[7,22,23] displayed in the same figure. The Rashba spin-orbit parameter $\alpha$ is shown in Fig. 3(b). The analysis of weak localization experiments with the ILP theory yields one Rashba parameter for each carrier density. Band-structure calculations yield different Rashba parameters for the two spin subbands because of the slight difference between the Fermi wave vectors for spin-up and spin-down states. However, this difference is small and can be neglected in the comparison with the weak localization data. A decrease of the Rashba parameter with increasing carrier density is observed. Again, the experimental results are in good agreement with the values obtained from the calculations. Figure 3(c) shows the occupations of the spin-split subbands as determined from SdH oscillations.[6,24] At carrier densities below $2.0 \times 10^{12}$ $cm^{-2}$ a good agreement between theory and experiment is observed. The first excited subband is only populated for carrier densities above about $2.3 \times 10^{12}$ $cm^{-2}$.[25] In the theory for a doping concentration of $1.8 \times 10^{17}$ $cm^{-3}$, population of the first excited subband occurs for carrier densities above $2.0 \times 10^{12}$ $cm^{-2}$, leading to kinks in the plots. This can be seen most easily in Fig. 3(c) for the spin-up electrons.

Values of the Rashba parameter determined from SdH oscillations in high magnetic fields[6,24] do not agree with the multiband calculations of Lamari[7,22] and Winkler[23] and the results from weak localization reported here. While they are of the same order of magnitude, they increase with increasing carrier density.

Using the effective mass from Eq. (3) and the subband carrier densities of Lamari displayed in Fig. 3(c) the simple relation[25] $\alpha = \hbar^2[\sqrt{4\pi n_\uparrow} - \sqrt{4\pi n_\downarrow}]/m^*$ yields Rashba parameters that agree well with those in Fig. 3(b). Hence the effective mass cannot be responsible for the discrepancy between the results in low and high magnetic fields. We currently do not understand why the splitting of the spin-subband densities from SdH oscillations as well as the increase thereof with growing carrier density are larger than theoretically predicted.

The situation in heterostructures of low carrier density is different, as a good agreement between theory and high-field experiments is found.[13] This indicates that the simple evaluation of beating patterns in SdH oscillations is not sufficient for the high carrier densities in 2DES inversion layers on $p$-type InAs crystals. In the carrier-density range well above $10^{12} cm^{-2}$ the spin-split energies no longer exhibit linear dispersion. Then band nonparabolicity and higher order terms in the expansion of the Rashba parameter become decisive. Hence it is important to consider the Rashba parameter as a function of both the electric field as well as of the in-plane wave vector.[10,26] The wave vector dependence exceeds the electric field contribution at high electron densities and leads to a decrease of the Rashba parameter. Obviously, for inversion layers on $p$-type InAs the evaluation of the weak localization measurements provides more reliable values for the Rashba parameter than that of SdH oscillations.

To conclude, we have studied spin-orbit interaction in the surface inversion layer on $p$-type InAs single crystals using weak localization at near zero magnetic field. Excellent description of the experimental data could be achieved through the theory of Iordanskii, Lyanda-Geller, and Pikus.[17,18] We find the carrier-density dependence of the spin-splitting energy $\Delta_0$ and the Rashba parameter $\alpha$ of the ground electric subband to be in very good agreement with multiband calculations, but to differ from previous analyses in which SdH beating patterns were evaluated.

We thank Saadi Lamari and Roland Winkler for valuable discussions and for providing detailed theoretical data, and Alexander Thieme for software development. The authors gratefully acknowledge financial support from the BMBF via the Verbundprojekt 13N8281 and from the Deutsche Forschungsgemeinschaft via SFB 508.

*Electronic address: cschierh@physnet.uni-hamburg.de

[1] S. A. Wolf, D. D. Awschalom, R. A. Buhrman, J. M. Daughton, S. von Molnár, M. L. Roukes, A. Y. Chtchelkanova, and D. M. Treger, Science **294**, 1488 (2001).
[2] G. Dresselhaus, Phys. Rev. **100**, 580 (1955).
[3] Yu. A. Bychkov and E. I. Rashba, J. Phys. C **17**, 6039 (1984).
[4] D. Grundler, Phys. Rev. Lett. **84**, 6074 (2000).
[5] T. Koga, J. Nitta, T. Akazaki, and H. Takayanagi, Phys. Rev. Lett. **89**, 046801 (2002).
[6] T. Matsuyama, R. Kürsten, C. Meißner, and U. Merkt, Phys. Rev. B **61**, 15 588 (2000).
[7] S. Lamari, Phys. Rev. B **64**, 245340 (2001).
[8] P. Pfeffer and W. Zawadzki, J. Supercond. **16**, 351 (2003).
[9] G. Lommer, F. Malcher, and U. Rössler, Phys. Rev. Lett. **60**, 728 (1988).
[10] E. A. de Andrada e Silva, G. C. La Rocca, and F. Bassani, Phys.

Rev. B **50**, 8523 (1994).
[11] J. Luo, H. Munekata, F. F. Fang, and P. J. Stiles, Phys. Rev. B **38**, 10 142 (1988); **41**, 7685 (1990).
[12] J. Nitta, T. Akazaki, H. Takayanagi, and T. Enoki, Phys. Rev. Lett. **78**, 1335 (1997).
[13] G. Engels, J. Lange, Th. Schäpers, and H. Lüth, Phys. Rev. B **55**, R1958 (1997).
[14] P. D. Dresselhaus, C. M. A. Papavassiliou, R. G. Wheeler, and R. N. Sacks, Phys. Rev. Lett. **68**, 106 (1992).
[15] S. Hikami, A. Larkin, and Y. Nagaoka, Prog. Theor. Phys. **63**, 707 (1980).
[16] Y. Kawaguchi, I. Takayanagi, and S. Kawaji, J. Phys. Soc. Jpn. **56**, 1293 (1987).
[17] S. V. Iordanskii, Y. B. Lyanda-Geller, and G. E. Pikus, JETP Lett. **60**, 206 (1994).
[18] W. Knap, C. Skierbiszewski, A. Zduniak, E. Litwin-Staszewska, D. Bertho, F. Kobbi, J. L. Robert, G. E. Pikus, F. G. Pikus, S. V. Iordanskii, V. Mosser, K. Zekentes, and Yu. B. Lyanda-Geller, Phys. Rev. B **53**, 3912 (1996).
[19] S. Pedersen, C. B. Sørensen, A. Kristensen, P. E. Lindelof, L. E. Golub, and N. S. Averkiev, Phys. Rev. B **60**, 4880 (1999).
[20] T. Ando, A. B. Fowler, and F. Stern, Rev. Mod. Phys. **54**, 437 (1982).
[21] U. Merkt and S. Oelting, Phys. Rev. B **35**, 2460 (1987).
[22] S. Lamari, Phys. Rev. B **67**, 165329 (2003).
[23] R. Winkler (private communication).
[24] Ch. Schierholz, R. Kürsten, G. Meier, T. Matsuyama, and U. Merkt, Phys. Status Solidi B **233**, 436 (2002).
[25] R. Kürsten, Ph.D. thesis, Universität Hamburg, 2002 (ISBN 3-89873-388-2). The spin-splitting of the first excited subband is of the same order of magnitude as that of the ground subband.
[26] E. A. de Andrada e Silva, G. C. La Rocca, and F. Bassani, Phys. Rev. B **55**, 16 293 (1997).

# 5 InAs heterostructures

Spin-orbit interaction is studied in heterostructures with an InAs channel. The structures feature an ingrown back-gate, which allows for independent tuning of the carrier density and of the channel asymmetry. The effects of this are investigated in low and high magnetic fields by means of transport experiments. This chapter first introduces the heterostructures and the geometries of the samples used. Simulations and measurements are then presented, in which the strength of spin-orbit interaction is determined under influence of various applied gate voltages. The chapter closes with an overview and discussion of the results.

## 5.1 Material system

The material system used in this chapter is a heterostructure with an InAs channel, simply referred to as an *InAs-HEMT*. It is grown on a (001) GaAs substrate by molecular beam epitaxy (MBE[1]) in Prof. Hansen's group at the University of Hamburg. A 20 nm thick layer of GaAs, donor doped with silicon at a concentration of $1.7\cdot10^{17}$ $cm^{-3}$, is grown directly onto the substrate. The doped layer features both good conductivity and low mobility, making it well suited as a back-gate. Atop this back-gate, an $In_xAl_{1-x}As$ buffer layer of 765 nm thickness is grown, in which x is increased from 5% to 75% in increments of 10% every 100 nm. In this way, the lattice constant of the GaAs substrate (5.6533 Å) is matched to that of the InAs/$In_{0.75}Ga_{0.25}As$ system (6.0584 Å), which constitutes the channel. Above the buffer an $In_{0.75}Al_{0.25}As$ layer of 442 nm thickness is grown. The actual quantum well, designed by Richter *et al.* [Ric00], consists of a 4 nm wide InAs channel that is embedded in an asymmetric rectangular $In_{0.75}Ga_{0.25}As/In_{0.75}Al_{0.25}As$ well. The upper $In_{0.75}Ga_{0.25}As/In_{0.75}Al_{0.25}As$ boundary is spaced 13.5 nm from the InAs channel, the lower boundary 2.5 nm. Part of the $In_{0.75}Al_{0.25}As$ layer below the quantum well is donor doped with silicon at a concentration of $1.7\cdot10^{17}$ $cm^{-3}$. It functions as a carrier supply layer and is spatially separated from the quantum well by 5 nm. This spatial separation is necessary, as the ionized dopants would otherwise reduce the mobility of the electrons in the well. The quantum well is covered by a 36 nm thick $In_{0.75}Al_{0.25}As$ cap layer. The layer sequence of the InAs-HEMT is displayed in Fig. 5.1(a).

Due to electron confinement in the growth direction, a 2DEG is formed in the quantum well. The 2DEG exhibits quantised subbands, of which only the ground subband is occupied for carrier densities below approximately $1\cdot10^{12}$ $cm^{-2}$ [Ric00]. The effective mass of the ground subband is $m^*=0.036\cdot m_e$, as is determined from temperature dependent SdH oscillations. Band-structure calculations of the channel region were performed using the Schrödinger-Poisson solver nextnano[3]

[1]MBE is used to fabricate custom-designed quantum wells with a virtually perfect lattice structure.

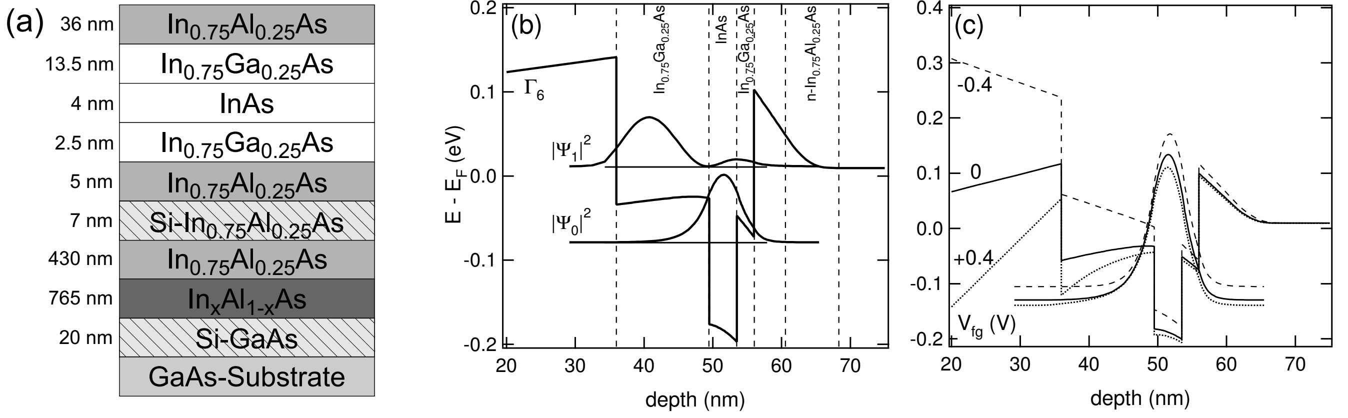


**Fig. 5.1:** (a) Layout of the InAs-HEMT with an ingrown back-gate. The channel region is displayed in white and the doped regions are hatched. The doped GaAs region above the substrate functions as back-gate. (b) Shape of the $\Gamma_6$ conduction band in the channel region for a front gate voltage of -0.1 V. The electron probabilities $|\Psi_0|^2$ and $|\Psi_1|^2$ of the ground and first excited subband in the quantum well are also displayed. (c) $\Gamma_6$ conduction band and electron probability $|\Psi_0|^2$ for three gate voltages. The band structures and electron probabilities are calculated with nextnano$^3$ [Vog].

[Vog]. Fig. 5.1(b) shows the resulting profile of the $\Gamma_6$ conduction band as well as the electron probabilities of the ground subband and the first excited subband of the quantum well for a front gate voltage of $V_{fg}$=-0.1 V.

The dominant origin of spin-orbit interaction in narrow-gap semiconductors can be attributed to SIA [Lom88, Das90, Eng97]. In previous transport experiments, strong spin-orbit interaction was identified in heterostructures with $InAs/In_{0.75}Ga_{0.25}As$ quantum wells alike those of the InAs-HEMTs [Gru00, Möl03, Hu03]. However, in these publications, the resulting spin-orbit interaction parameters were compared to rough estimates and not to values calculated from the band structure of the samples. In the following, the Rashba parameters of the InAs-HEMT will thus be calculated from the band structure. When calculating the total Rashba parameter $\alpha_{tot}$ of the InAs-HEMTs, both the field and the boundary contributions must be considered [Gru00]. The confining potential exhibits a strong gradient in the region of the quantum well, which leads to a significant field contribution $\alpha_f$. In symmetric quantum wells with a symmetric choice of materials, the boundary contribution $\alpha_b$ is negligible [dAeS97, Sch98]. The quantum well of the InAs-HEMT is symmetric with respect to the choice of materials but asymmetric with respect to the layer thicknesses. Therefore, a significant boundary contribution to the total Rashba parameter $\alpha_{tot}$ is expected. As was shown in Section 2.1.2, all interfaces at which the electron probability is non-zero must be considered when determining $\alpha_b$. As can be seen in Fig. 5.1(b), the electron probability $|\Psi_0|^2$ of the ground subband is non-zero at both boundaries of the InAs channel as well as at the $In_{0.75}Ga_{0.25}As/In_{0.75}Al_{0.25}As$ interface below the channel. The values of $\alpha_f$ and $\alpha_b$ are determined from the band structure and electron probability according to Eqs. (2.9) and (2.10), and the total Rashba parameter is determined as described in Eq.(2.11).

When a gate voltage $V_{fg}$ is applied between a front-gate and the InAs channel of the InAs-HEMT,

it influences both the carrier density and the asymmetry of the quantum well. Fig. 5.1(c) shows calculated band structures for three different front-gate voltages $V_{fg}$. In the calculations, the gate voltages are applied directly to the semiconductor surface, but current flow to and from the gate electrode is inhibited. Limitations of the simulation software prevent pinning of the conduction band in the region of the InAs channel, as would be required to correctly reproduce experiments. Instead, the conduction band is pinned directly below the carrier supply layer, the effects of which are however negligible: the 2DEG shields the semiconductor layers below the channel from most of the electric field caused by $V_{fg}$. Thus, $V_{fg}$ only effects small changes in the $In_{0.75}Ga_{0.25}As$ layer below the channel, slightly affecting the field contribution. If the conduction band would be pinned in the channel region, the electron probability $|\Psi|^2$ would be shifted slightly more towards the sample surface. This would lead to a slightly altered boundary contribution. Estimates show that the changes in the field and the boundary contribution cancel each other out almost entirely for all carrier densities, at which only the first subband is occupied. Thus, the Rashba parameters resulting from band-structure calculations can be directly compared to experiments for the first subband. The effect of $V_{fg}$ on the strength of spin-orbit interaction in the quantum well shall now be clarified by considering the three gate voltages displayed in Fig. 5.1(c): when a negative voltage $V_{fg}$=-0.4 V is applied, the conduction band is raised at the sample surface. This leads to a strong potential gradient across the quantum well, which results in a strong field contribution to $\alpha_{tot}$. Due to the potential gradient, the probability density $|\Psi_0|^2$ of electrons in the ground state is not centered in the quantum well, but shifted towards the substrate. The boundary contribution of a single interface $i$ at the position $z_i$ depends on a material dependent parameter $C_{b,i}$ and $|\Psi_0(z_i)|^2$. Thus, a distribution of $|\Psi_0|^2$ positioned towards the bottom of the quantum well, increases the importance of the lower interfaces in the quantum well for the boundary contribution. In the InAs-HEMTs, the parameters $C_{b,i}$ are positive for the two interfaces above the channel and negative for the interfaces below the channel. The magnitudes of the $C_{b,i}$ are comparable for the two InAs/$In_{0.75}Ga_{0.25}As$ interfaces and for the two $In_{0.75}Ga_{0.25}As$/$In_{0.75}Al_{0.25}As$ interfaces, respectively. Therefore, if the lower interfaces in the quantum well dominate the boundary contribution, $\alpha_b$ will be strongly negative.

When $V_{fg}$ is increased towards more positive voltages, the conduction band is lowered at the sample surface. The potential gradient across the channel decreases with increasing $V_{fg}$, thus reducing the field contribution. However, as can be seen in Fig. 5.1(c) for $V_{fg}$=0 and $V_{fg}$=+0.4 V, small negative contributions to $\alpha_f$ arise from the upper $In_{0.75}Ga_{0.25}As$ region. Nonetheless, the overall value of $\alpha_f$ remains positive, as the major part of $|\Psi_0|^2$ is in the region of the InAs channel. Due to the decreasing potential gradient across the channel, the electron probability $|\Psi_0|^2$ is shifted further towards the sample surface with increasing increasing $V_{fg}$. Concerning the boundary contribution, this results in a decreasing importance of the two lower interfaces in the quantum well and an increasing importance of the two upper interfaces in the quantum well. Thus, increasing $V_{fg}$ from the original value of $V_{fg}$=-0.4 V shifts the boundary contribution from negative values to zero and then to positive values.

The above considerations for the field and boundary contributions can also be applied to the first subband. As can be seen in Fig. 5.1(b), the electron probability of the first excited subband $|\Psi_1|^2$ is concentrated in the $In_{0.75}Ga_{0.25}As$ region above the channel. For gate voltages, at which

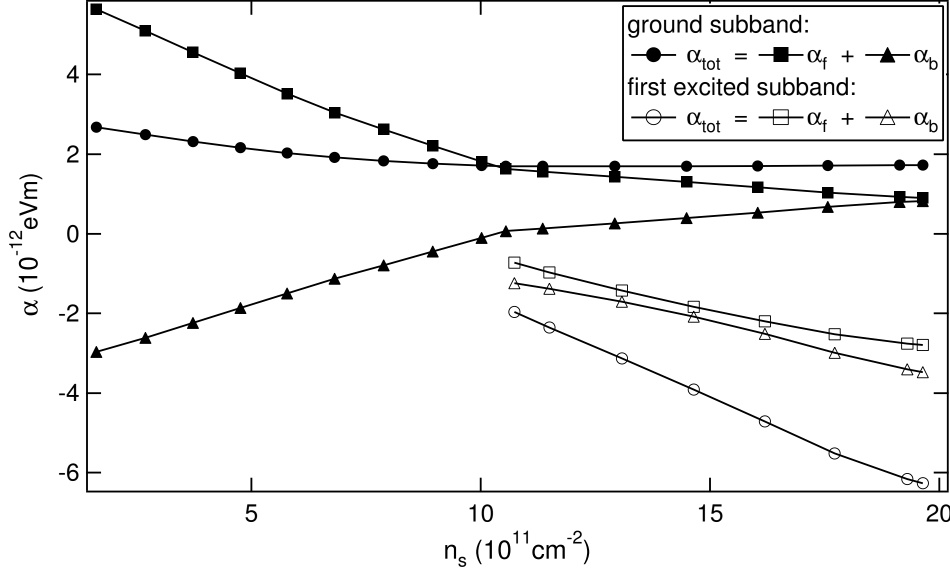


**Fig. 5.2:** Calculated Rashba parameters in dependence of the total carrier density $n_s$. The field and boundary contributions, $\alpha_f$ and $\alpha_b$, as well as the total Rashba parameter $\alpha_{tot}$ are displayed both for the ground subband (closed symbols) and the first excited subband (open symbols) of the quantum well. The values are calculated according to Equations (2.9) and (2.10). The Rashba parameters are calculated from probability densities and band structures simulated with the Schrödinger-Poisson solver nextnano[3] [Vog].

the first excited subband is occupied, the potential gradient in this region is opposite to that of the InAs channel. As the potential gradient in the upper $In_{0.75}Ga_{0.25}As$ layer increases with increasing $V_{fg}$, the field contribution is expected to become more negative. Determining the boundary contribution for the first excited subband is more difficult, due to the complex shape of $|\Psi_1|^2$: it would be expected, that the upper $In_{0.75}Ga_{0.25}As/In_{0.75}Al_{0.25}As$ interface dominates the boundary contribution due to the large value of $|\Psi_1|^2$. However, the material dependent boundary parameters $C_{b,i}$ of the $InAs/In_{0.75}Ga_{0.25}As$ interfaces are about a factor of five larger than those of the $In_{0.75}Ga_{0.25}As/In_{0.75}Al_{0.25}As$ interfaces. Thus, the difference of $|\Psi_1|^2$ at the two $InAs/In_{0.75}Ga_{0.25}As$ dominates the boundary contribution. Due to the significantly larger value of $|\Psi_1|^2$ at the lower $InAs/In_{0.75}Ga_{0.25}As$ interface, this results in a negative boundary contribution of the first excited subband. The carrier density in the quantum well also depends on the gate voltage $V_{fg}$: when the conduction band is raised at the sample surface due to negative $V_{fg}$, the quantum well is raised with respect to the Fermi energy, resulting in a low carrier density. When $V_{fg}$ is increased, the quantum well is lowered and the carrier density increases.
The band structures of the InAs-HEMT as well as the electron probabilities in the quantum well are calculated for surface gate voltages ranging from $V_{fg}$=-0.9 V to +0.5 V, which correspond to carrier densities from $n_s$=1.5·$10^{11}$ cm$^{-2}$ to 2·$10^{12}$ cm$^{-2}$. Both the field and the boundary contributions $\alpha_f$ and $\alpha_b$ are calculated, as well as the total Rashba parameter $\alpha_{tot}$. Fig. 5.2 shows the results as a function of the total carrier density $n_s$, both for the ground subband and for the first excited subband. The total carrier density is a well suited reference parameter, as it can easily be determined experimentally. Both $\alpha_f$ and $\alpha_b$ show the expected dependence on the carrier

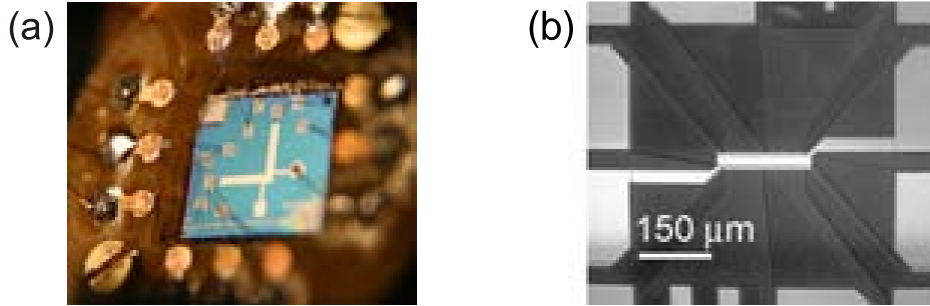


**Fig. 5.3:** Hall-bars processed on InAs-HEMTs. (a) Photograph of an L-shaped Hall-bar which is used to perform simultaneous transport experiments in both the $[\bar{1}10]$ and the $[110]$ directions. The width of the Hall-bar is 20 $\mu$m, the distance between voltage probes is 400 $\mu$m. In the image, the sample is mounted on a copper/pertinax chip-carrier, ready for experiments. The wire bonds used to make electrical contact to the sample can be observed. (b) Micrograph of a Hall-bar aligned in $[110]$ direction. The width of the structure is 20 $\mu m$, and the spacing between voltage probes is 80 $\mu m$.

density: the field contribution is reduced with increasing carrier density (i.e. with increasingly positive gate voltage) due to the reduced potential gradient across the channel. The boundary contribution is reduced from its initial negative value as a result of $|\Psi_0|^2$ being shifted more towards the top of the quantum well. A sign change of $\alpha_b$ occurs at a carrier density of approximately $1{\cdot}10^{12}$ cm$^{-2}$, above which $\alpha_b$ increases with increasing carrier density. The total Rashba parameter $\alpha_{tot} = \alpha_f + \alpha_b$ is found to decrease with increasing $n_s$, until occupation of the first subband occurs at $n_s \geq 1 \cdot 10^{12}$ cm$^{-2}$. Then, a slight increase of $\alpha_{tot}$ with increasing $n_s$ is observed. At the onset of occupation of the first excited subband, kinks are observed in $\alpha_f$, $\alpha_b$, and thus also in $\alpha_{tot}$ as functions of the carrier density. The electrons in the first excited subband partially shield the electric field effected by $V_{fg}$, lessening its effect on the electrons in the ground subband[2].

## 5.2 Sample geometry

The strength of spin-orbit interaction is determined in samples in Hall-bar geometry. Hall-bars are advantageous, as they not only provide a defined geometry of the 2DEG, but enable simultaneous recording of longitudinal and transversal voltage drops across the sample. Processing of the Hall-bars on the InAs-HEMTs was performed both at the University of Hamburg and at the NTT basic research laboratories in Atsugi, Japan. The process technologies common to each location were used, the respective process parameters are presented in Appendix A.
It is well known that the transport properties of MBE-grown III-V semiconductors depend on the crystal orientation [Sch91, Ram96, Ric00, Löh04]. L-shaped Hall-bars aligned in the $[\bar{1}10]$ and the $[110]$ direction were employed to study both crystalline directions of the InAs-HEMTs. Transport experiments on several L-shaped Hall-bars under a variety of experimental conditions only showed

[2] In part, the kinks are also due to being displayed as a function of the total carrier density. However, the kinks can still be observed, when $\alpha_f$, $\alpha_b$, and $\alpha_{tot}$ are displayed as a function of the subband carrier density.

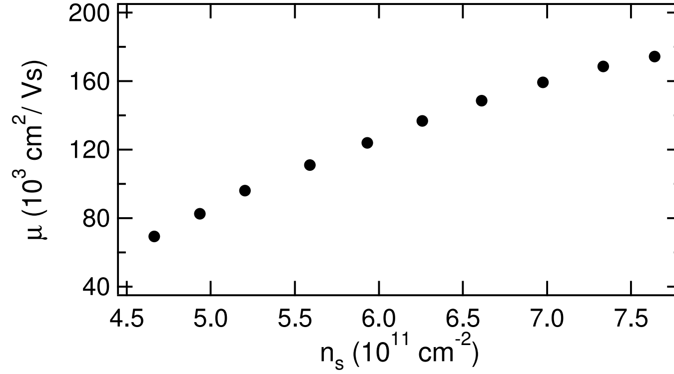


**Fig. 5.4:** Hall mobility $\mu$ in [110] direction as a function of the carrier density $n_s$.

analysable results for current flow in the [110] direction. Thus, only conventional Hall-bars in [110] orientation were made in later processing.
The processing of the Hall-bars is conducted as follows: first, the ingrown back-gate of the InAs-HEMT is connected, as described in Chapter 3. Then, the actual Hall-bars are defined by means of optical lithography and subsequent wet chemical or RIE etching. Afterwards, the 2DEG is contacted by consecutively patterning metal contacts onto the bond pads and annealing at 275 °C. Following this, a $SiO_2$ gate oxide is grown by PECVD. The $SiO_2$ is 350 nm thick for samples processed in Hamburg and 115 nm thick for samples processed in Atsugi. A metallic front-gate electrode is patterned on the oxide above the Hall-bar. In a final step, the gate oxide is removed above both the bond pads and the back-gate by etching. Fig. 5.3 shows two completed Hall-bars, one in 'L' geometry and one in conventional geometry. The L-shaped Hall-bars are 20 $\mu$m wide and the voltage probes are spaced by 400 $\mu$m. They feature two Hall-crosses in each direction. The conventional Hall-bars also have a width of 20 $\mu$m and the voltage probes are spaced 80 $\mu$m apart. They feature three equally spaced Hall-crosses.

## 5.3 Experiments

Two different transport experiments are performed to determine the strength of spin-orbit interaction in InAs-HEMTs: WAL and SdH oscillations. All experiments are conducted either in an Oxford Instruments' Heliox $^3$He cryostat or in a Kelvinox $^3$He-$^4$He dilution refrigerator at nominal temperatures ranging from 300 mK to 30 mK. Both cooling systems feature integrated superconducting magnets that can generate magnetic fields in excess of 8 T. Low noise voltage sources with floating ground are used to apply gate voltages. The samples are contacted in four-point geometry and biased with an AC current. Standard lock-in technology[3] is used to record both longitudinal and transverse voltage drops. Control of experiments and recording of data is fully automated.
The carrier density in the 2DEG is controlled by a voltage $V_{fg}$ applied between the front-gate and the InAs channel. The response of the semiconductor system to a specific front gate depends on

[3] All experiments are performed with Stanford Research Instruments' SRS830 lock-in amplifiers. The 'offset' and 'expand' modes are used to resolve the fairly small signals of WAL over a large background.

both the thickness and growth parameters[4] of the gate oxide. Therefore, to enable comparison of different samples, results must be analysed in dependence of the carrier density rather than as a function of the gate voltage. A second voltage $V_{fbg}$ can be applied between the front-gate and the back-gate.
L-shaped Hall-bars are used to determine the influence of the current direction with respect to the crystalline axes. Magnetotransport was studied in parallel for both the $[\bar{1}10]$ and the $[110]$ direction in various samples and under various conditions. Analysable was only obtained in the $[110]$ direction, so that the $[\bar{1}10]$ was not considered in further experiments. All results presented in this chapter are from experiments with current flow parallel to the $[110]$ axis.
The Hall mobility $\mu$ is determined from the resistance in zero-magnetic field and the Hall-voltage across the sample[5] [Dat95]. The Hall mobility displayed in Fig. 5.4 as a function of the carrier density is obtained by varying $V_{fg}$. One finds $\mu$ to increase with increasing carrier density. At the highest recorded carrier density of $n_s$=7.6·10$^{11}$ cm$^{-2}$ the Hall mobility is determined to be $\mu$=175.000 cm$^2/Vs$. Qualitatively, these values agree well with those determined by Richter *et al.* [Ric00] for samples with identical InAs/$In_{0.75}Ga_{0.25}As$ quantum wells. However, quantitatively, the Hall-mobility of the samples studied by Richter *et.al* is only approximately half that of the InAs-HEMTs studied here.
Pronounced features of WAL are observed in magnetoconductance experiments at fields of a few mT. In magnetic fields above 0.9 T, SdH oscillations are observed. Both experimental methods are used to determine the strength of the spin-orbit interaction parameter $\alpha$ for a carrier density range from 3.5·10$^{11}$ cm$^{-2}$ to 7.5·10$^{11}$ cm$^{-2}$. The dependence of $\alpha$ on applied gate voltages is studied in two series of experiments, each of which are performed in low and high magnetic fields: first, WAL and SdH oscillations are recorded for various values of $V_{fg}$. The back-gate is not connected in these experiments. Second, WAL and SdH oscillations are recorded for various values of $V_{fbg}$. In these experiments, WAL can be observed without an applied front gate voltage $V_{fg}$, so that the channel is left to float. In contrast to this, distinct SdH oscillations can only be observed when a voltage $V_{fg}$ is applied. In the following, the experiments in low and high magnetic fields will be presented separately. The results will be compared in the last section of this chapter.

## 5.4 Low field experiments

All experiments in low magnetic fields are performed under an AC-current bias of 2.5 $\mu$A, modulated at a frequency of 33.37 Hz. The samples used are conventional Hall-bars, processed in Atsugi. Both the voltage drop in longitudinal direction and the Hall-voltage across the structure are measured simultaneously. Experiments are performed by sweeping the magnetic field at set gate voltages $V_{fg}$ and $V_{fbg}$. The magnetic field is swept at a rate of 5 $\mu$T per second, driven by a Keithley 2400 source-meter. The gate voltages are changed after each sweep of the magnetic field. A subsequent delay[6] allows the system to reach equilibrium before the next sweep of the magnetic

[4]The growth parameters of the $SiO_2$ influence the dielectric constant.

[5]$\mu = \frac{I/|e|}{n_s V_x W/L}$, with $I$: bias current, $V_x$: longitudinal voltage drop, and the width $W$ and length $L$ of the Hall-bar.

[6]The delay time is determined as a trade-off between the total duration of the experiment and the time for the system to reach equilibrium. Typical delay times range from 15 minutes to 1 hour.

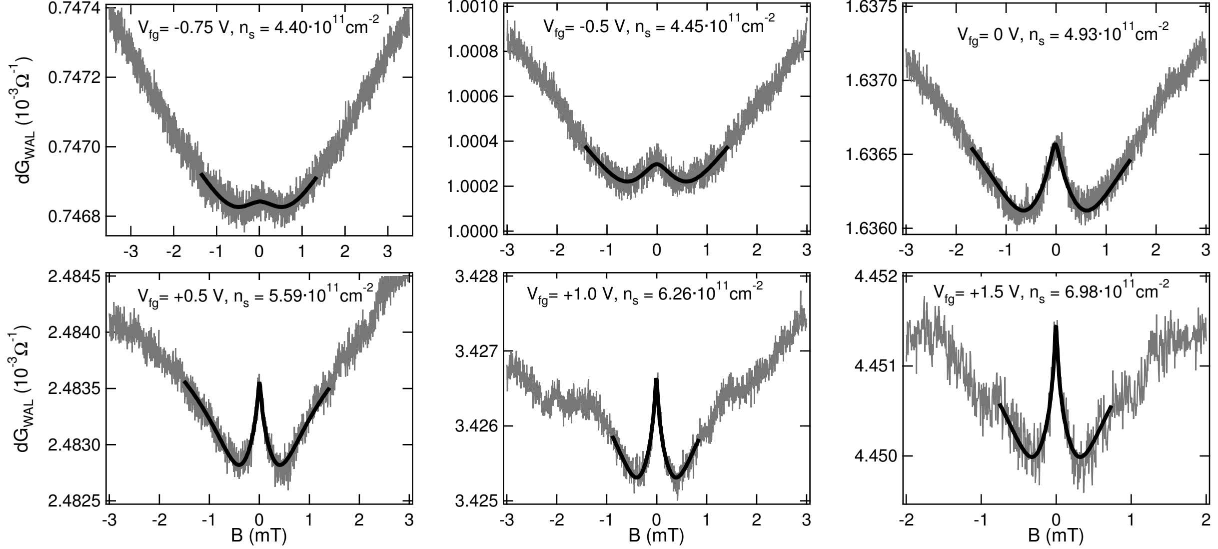


**Fig. 5.5:** Low-field magnetoconductance recorded at a mixing chamber temperature of 35 mK. Pronounced WAL can be observed for various voltages $V_{fg}$ applied between the front-gate and the InAs channel. Experiments are performed under an AC bias current of 2.5 $\mu$A at a frequency of 33.37 Hz. The best fits with ILP theory are shown as solid lines. The carrier densities are determined from Hall voltages recorded simultaneously with the magnetoconductances.

field. The superconducting magnet used exhibits a remanent magnetic field in the order of a few mT. This can easily be determined, as WAL is a sensitive detector for zero magnetic fields. The remanence is removed by shifting the values of the magnetic field in such a way, that the recorded WAL is symmetric with respect to the zero-point of the magnetic field. The remanence has been removed for all data presented in the following.
In the first experiment, the influence of a front-gate voltage $V_{fg}$ on the spin-orbit interaction is studied. Magnetoconductances recorded in fields below 5 mT show WAL for various front-gate voltages $V_{fg}$. Data is recorded for all values of $V_{fg}$, at which WAL can be observed, i.e. from $V_{fg}$=2 V to $V_{fg}$=-1.5 V. This corresponds to carrier densities from approximately 7.5·$10^{11}$ cm$^{-2}$ to 4.5·$10^{11}$ cm$^{-2}$. Fig. 5.5 exemplarily shows the recorded magnetoconductances for six gate voltages. WAL can clearly be observed for all displayed values of $V_{fg}$, even though the magnitude of the conductance corrections is less than 1‰ of the conductance. The strength of the spin-orbit interaction is determined by fits to the experimental data with the theory by Iordanski, Lyanda-Geller, and Pikus (ILP) described by Eq.(2.20). The actual fitting is carried with the 'curve fit' package of Igor Pro, into which the ILP theory is included by means of an XOP, as is described in Appendix B. The best fits show very good agreement with the experimental data and are displayed as solid lines in Fig. 5.5. The Rashba parameters $\alpha$ are determined from the fit results according to Eq.(2.24). Fig. 5.6 shows the resulting values for $\alpha$ as a function of the carrier density $n_s$. In addition, the Rashba parameter $\alpha_{tot}$ obtained from band-structure simulations in Section 5.1 is displayed as a solid line. These results will be discussed in the last section of this chapter.
The second experiment studies the influence of a voltage $V_{fbg}$ applied between the front-gate and the back-gate on the strength of the spin-orbit interaction. Magnetoconductances are recorded in

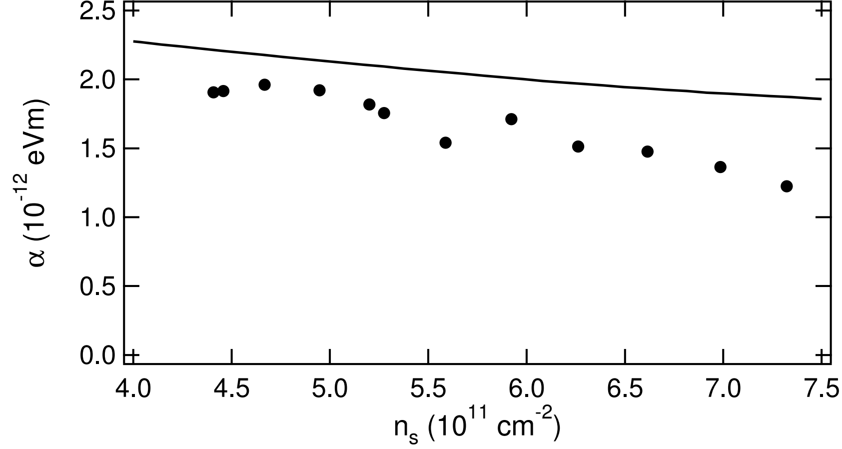


**Fig. 5.6:** Rashba parameter $\alpha$ as a function of the carrier density. The round symbols represent results from WAL experiments for various values of $V_{fg}$, as presented in Fig. 5.5. The solid line results from the band structure calculations presented in Section 5.1.

fields below 5 mT for various values of $V_{fbg}$. When the InAs channel is fixed to a defined potential, i.e. when a gate voltage is biased against the channel, no WAL is observed. Thus, data is recorded for $V_{fbg}$=+2.5 V to -10.5 V, while the channel remains floating. Fig. 5.7 exemplarily shows the recorded magnetoconductances for nine different values of $V_{fbg}$. Distinct features of WAL are observed for all values of $V_{fbg}$, despite the magnitude of the conductance corrections being less than 1‰ of the classical magnetoconductance. The strength of spin-orbit interaction is determined by fits to the experimental data according to ILP theory, as is described above. The best fits are superimposed as solid lines in Fig. 5.7, where very good agreement can be observed. It should be noted that the experimental data exhibited disturbances at near-zero magnetic fields for $V_{fbg}$=+1.25 V, -0.75 V, -2 V, -2.5 V, and -3.25 V. Despite only fitting part of the recorded data in these cases, consistent results are obtained. The carrier density $n_s$, determined from the Hall voltage across the sample, shows a remarkable dependence on $V_{fbg}$, as can be seen in Fig. 5.8(a). Numbered arrows mark the measured sequence of $V_{fbg}$ starting from +1.75 V and moving to -7 V. The region from $V_{fbg}$=+2 V to -1.25 V is represented by arrow 1, the region from $V_{fbg}$=-1.25 V to -2 V is represented by arrow 2, and the region from $V_{fbg}$ $\leq$-2 V is represented by arrow 3. Starting from positive values of $V_{fbg}$ and moving towards negative values, $n_s$ at first increases to a maximum of about $4.6{\cdot}10^{11}$ cm$^{-2}$ at $V_{fbg}$=-1.25 V (arrow 1), then decreases (arrow 2) and finally saturates at $n_s \simeq 4.45{\cdot}10^{11}$ cm$^{-2}$ for $V_{fbg} \leq$ -2 V (arrow 3). A possible cause of the saturation may be diffusion of electrons from the 2DEG to the back-gate. The Rashba parameters $\alpha$ are calculated from the results of the fits to the magnetoconductance according to equation Eq.(2.24). They are displayed in Fig5.8(b) and (c) as functions of the voltage $V_{fbg}$ and the carrier density $n_s$, respectively. Starting again from positive values of $V_{fbg}$ and moving towards negative values, $\alpha$ increases linearly from $\alpha \simeq$1.6 eVm at $V_{fbg}$=+1.75 V to $\alpha \simeq$1.9 eVm at $V_{fbg}$=-2 V, and then linearly decreases to $\alpha \simeq$1.6 eVm at $V_{fbg}$=-7 V. The dependence of $\alpha$ on the carrier density $n_s$ is more complex, due to the complicated dependencies of $n_s$ and $\alpha$ on $V_{fbg}$. The numbered arrows in Fig. 5.8(c) show the sequence of Rashba parameters for values of $V_{fbg}$ starting from +1.75 V and moving to -7 V. The

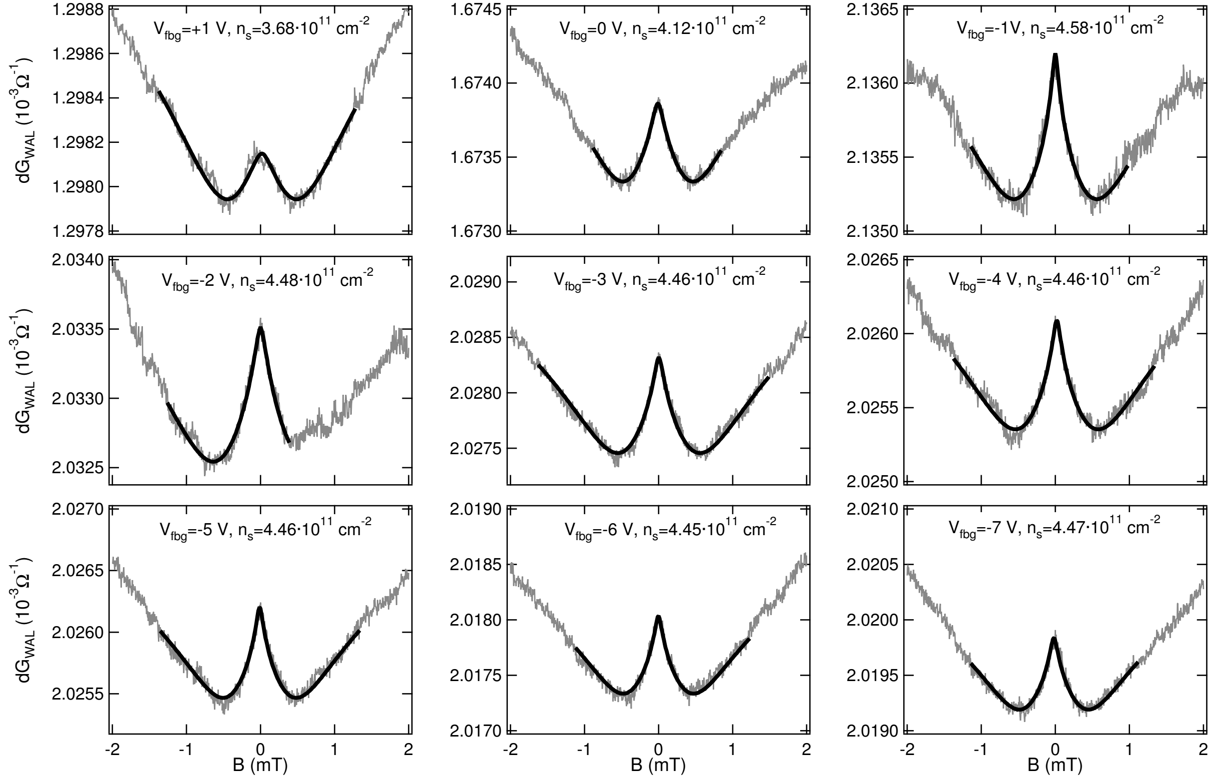


**Fig. 5.7:** Low-field magnetoconductances recorded at a mixing chamber temperature of 35 mK. Distinct WAL is observed for various voltages $V_{fbg}$ applied between the front-gate and the back-gate. The channel remains floating. Experiments are performed under an AC bias current of 2.5 $\mu$A at a frequency of 33.37 Hz. The best fits with ILP theory are shown as solid lines. The carrier densities are determined from Hall voltages recorded simultaneously with the WAL.

section marked by arrow 3 shows a most interesting behaviour of the Rashba parameter: tunability that is independent of the carrier density. The Rashba parameter is tuned from approximately $\alpha_{max}$=1.9·10$^{-12}$ eVm to $\alpha_{min}$=1.6·10$^{-12}$ eVm at a constant carrier density of $n_s \simeq$4.45·10$^{11}$ cm$^{-2}$. Expressed in relative terms, $\alpha$ is changed by about 17%.

## 5.5 High field experiments

Transport experiments in high magnetic fields are performed on both L-shaped and conventional Hall-bars. The magnetoresistance is recorded at set gate voltages $V_{fg}$ and $V_{fbg}$ by sweeping the magnetic field at rates between 3 and 5 mT per second. After each sweep the gate voltages are changed, followed by a delay that allows the semiconductor system to reach equilibrium before the next sweep is started. Depending on the sample, experiments are performed either under an AC current bias, or under a DC current bias with an AC voltage superimposed on the gate voltage. Both modulation techniques yield the same pattern of SdH oscillations, so the technique resulting in the better signal is used. SdH oscillations were recorded for many samples. Beating patterns in the oscillations were only observed in a few samples, and, in agreement with reference [Gru00],

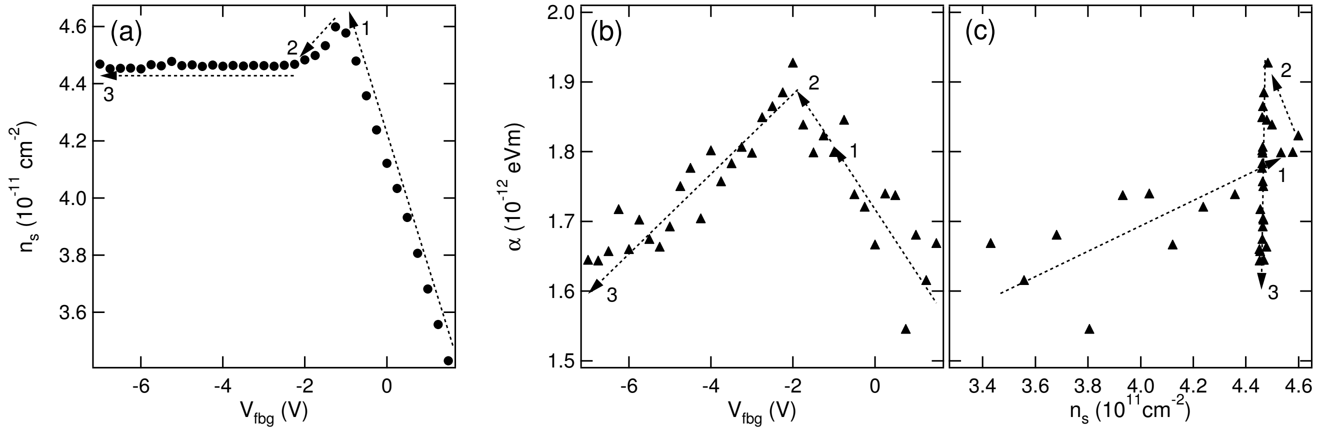


**Fig. 5.8:** (a) Dependence of the carrier density $n_s$ on the voltage $V_{fbg}$ between the front-gate and the back-gate. Experiments were performed for decreasing $V_{fbg}$, starting from $V_{fbg}$=+1.75 V. The InAs channel remains floating. A saturation of the carrier density can be observed for $V_{fbg} \leq$-2 V. (b) Rashba parameter $\alpha$ in dependence of $V_{fbg}$. (c) Rashba parameter $\alpha$ as a function of the carrier density $n_s$. A sequence of numbered arrows shows the dependence of $\alpha$ on decreasing $V_{fbg}$.

only when positive voltages $V_{fg}$ were applied between the front-gate and the InAs channel [dB03]. In the first high field experiment, the influence of the front-gate voltage $V_{fg}$ on the spin-orbit interaction is studied. The magnetoresistance of an L-shaped Hall-bar processed in Hamburg was measured at a temperature of 60 mK. A DC current bias of 200 nA was applied and $V_{fg}$ was overlaid with an AC voltage of 500 mV (peak to peak) at a frequency of 337.3 Hz. Fig. 5.9 shows both the experimental magnetoresistance and the carrier density distribution for front-gate voltages ranging from $V_{fg}$=+0.2 V to +6.2 V. The results show clear SdH oscillations for all displayed values of $V_{fg}$. For gate voltages from $V_{fg}$=+1 V to +5.6 V, which correspond to carrier densities ranging from $4{\cdot}10^{11}$ cm$^{-2}$ to $6.5{\cdot}10^{11}$ cm$^{-2}$, distinct beating patterns can be observed in the SdH oscillations, the nodes of some of which are marked by crosses in Fig. 5.9. The carrier density distributions displayed on the right side of Fig. 5.9 are determined from the experimental data by Fast Fourier Transform (FFT)[7]. For $V_{fg}$ <5.8 V, a clear splitting of the carrier density distribution into two peaks can be observed. The peaks correspond to the two slightly different carrier densities $n_\uparrow$ and $n_\downarrow$ of the spin non-degenerate subbands. The exact values of $n_\uparrow$ and $n_\downarrow$ are determined by fitting Gauss functions to the respective peaks. They are displayed as a function of the total carrier density $n_s = n_\uparrow + n_\downarrow$ in Fig. 5.10(a). Linear fits to the carrier densities of the spin non-degenerate subbands are displayed as guides to the eye. A decrease in the splitting $\Delta n_s$ of $n_\uparrow$ and $n_\downarrow$ is observed for increasing carrier density $n_s$. Using the parabolic approximation given by Eq.(2.16), the strength of the Rashba spin-orbit interaction parameter $\alpha$ can be determined from $n_\uparrow$ and $n_\downarrow$. Fig. 5.10(b) shows the resulting values for $\alpha$ versus the carrier density $n_s$. The Rashba parameter is found to decrease with increasing carrier density, which is in agreement with both the results calculated from the band structures and with the results obtained from WAL. A quantitative comparison follows in the final section of this chapter.

[7] A good introduction to determining the carrier density from SdH oscillations can be found in reference [Kür02].

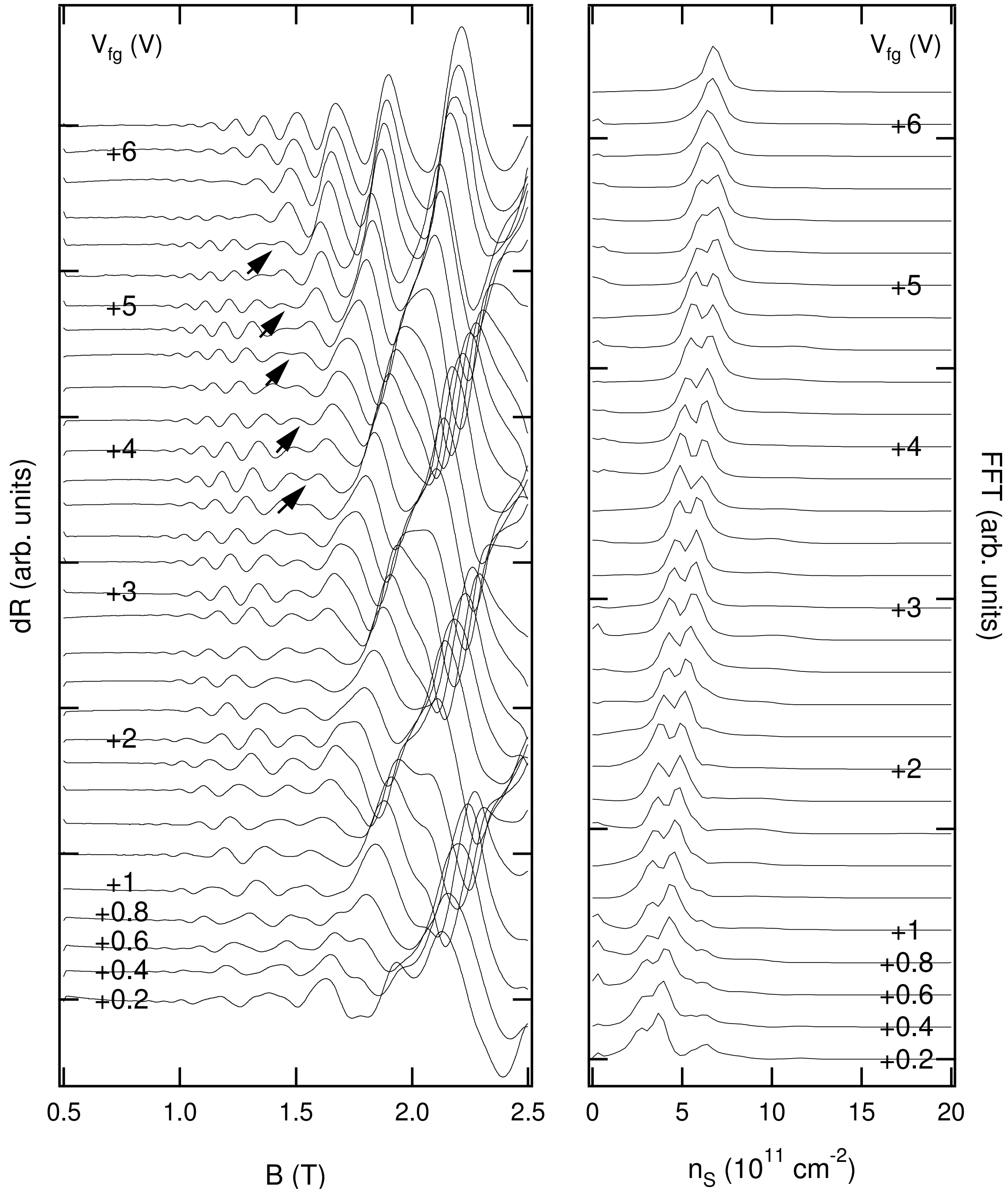


**Fig. 5.9:** Magnetoresistance of an L-shaped Hall-bar at a nominal temperature of T=60 mK. SdH oscillations are observed for all displayed voltages $V_{fg}$ applied between the front gate and the InAs channel. Experiments were performed under a DC current bias of $I_{bias}$=200 nA and a modulation of $V_{fg}$ of 500 mV. The SdH oscillations exhibit beating patterns, the nodes of some of which are marked by arrows. The carrier density distribution, as determined by FFT, is displayed on the right side. Two separate peaks, each belonging to one spin non-degenerate subband, are resolved for values of $V_{fg}$ below 5 V. Note that the x-axis of the carrier density distribution is scaled for spin-degenerate subbands and must be halved to obtain the carrier densities $n_\uparrow$ and $n_\downarrow$ of spin non-degenerate subbands. All traces are normalised in amplitude and offset for clarity.

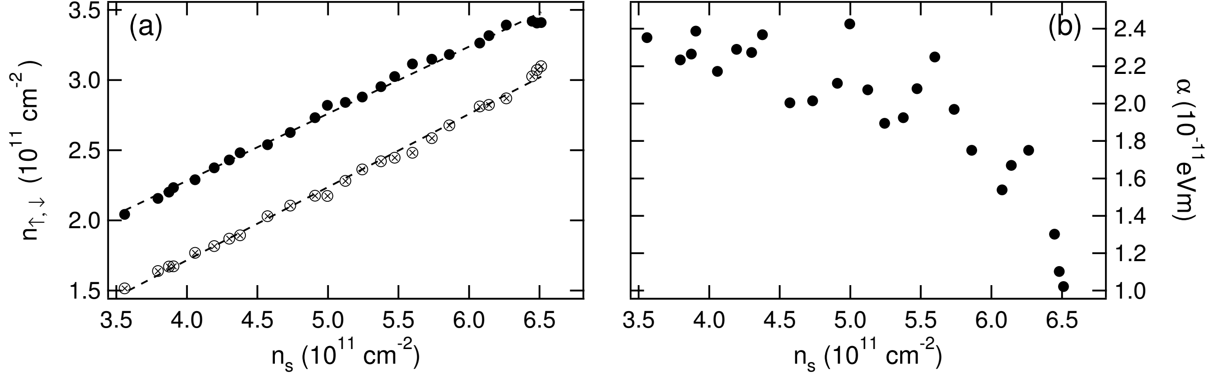


**Fig. 5.10:** Spin-splitting determined from SdH oscillations for various front-gate voltages $V_{fg}$ as displayed in Fig. 5.9. (a) Carrier densities $n_{\uparrow}$ and $n_{\downarrow}$ of the spin non-degenerate subbands as a function of the total carrier density $n_s$. Linear fits to the experimentally determined values are displayed as dashed lines. (b) Rashba parameters $\alpha$ determined from $n_{\uparrow}$ and $n_{\downarrow}$ according to Eq.(2.16).

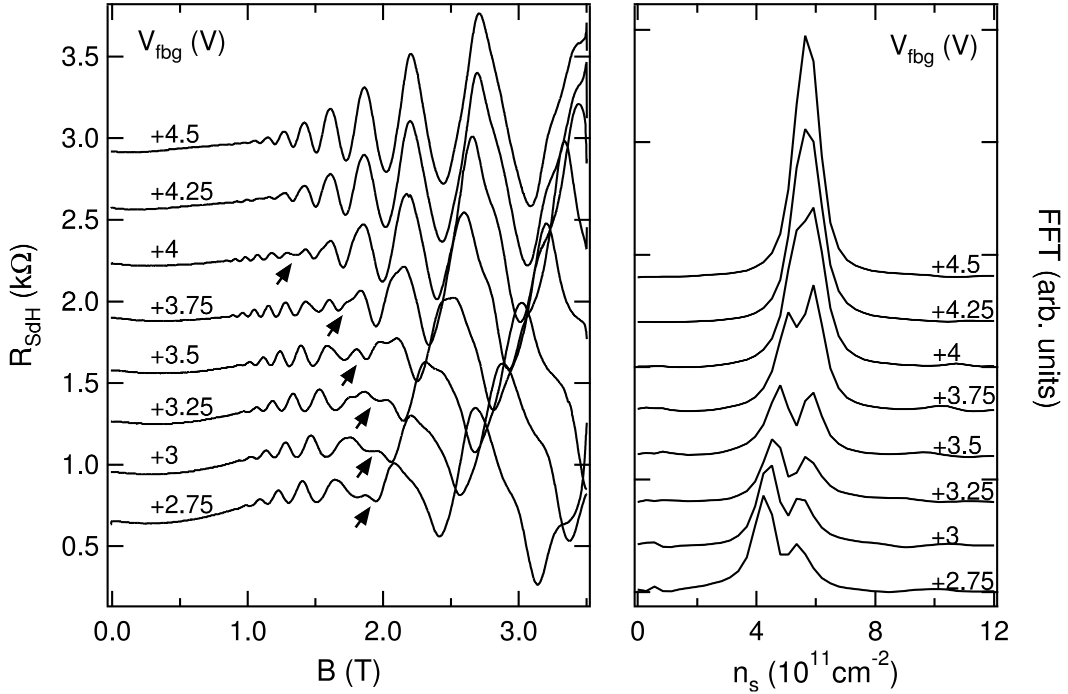


**Fig. 5.11:** Data of a conventional Hall-bar for various values of $V_{fbg}$ at a fixed $V_{fg}$=2.5 V and a temperature of T≃280 mK. Experiments were performed under an AC current bias $I_{bias}$=35 nA at a frequency of 190.1 Hz. Distinct beating patterns are observed for $V_{fbg} \leq 4$ V, and the nodes are marked by arrows. A FFT is used to determine the carrier density distribution for each value of $V_{fbg}$. The resulting distributions are displayed in the right image. For $V_{fbg} \leq 4$ V, the carrier density distributions show two separate peaks, each belonging to one spin non-degenerate subband. The scaling of the x-axis is chosen for spin-degenerate subbands and must thus be halved to yield the carrier densities $n_{\uparrow}$ and $n_{\downarrow}$ of the spin non-degenerate subbands. The SdH traces are offset by 350 Ω. The FFT traces are normalised and offset for clarity.

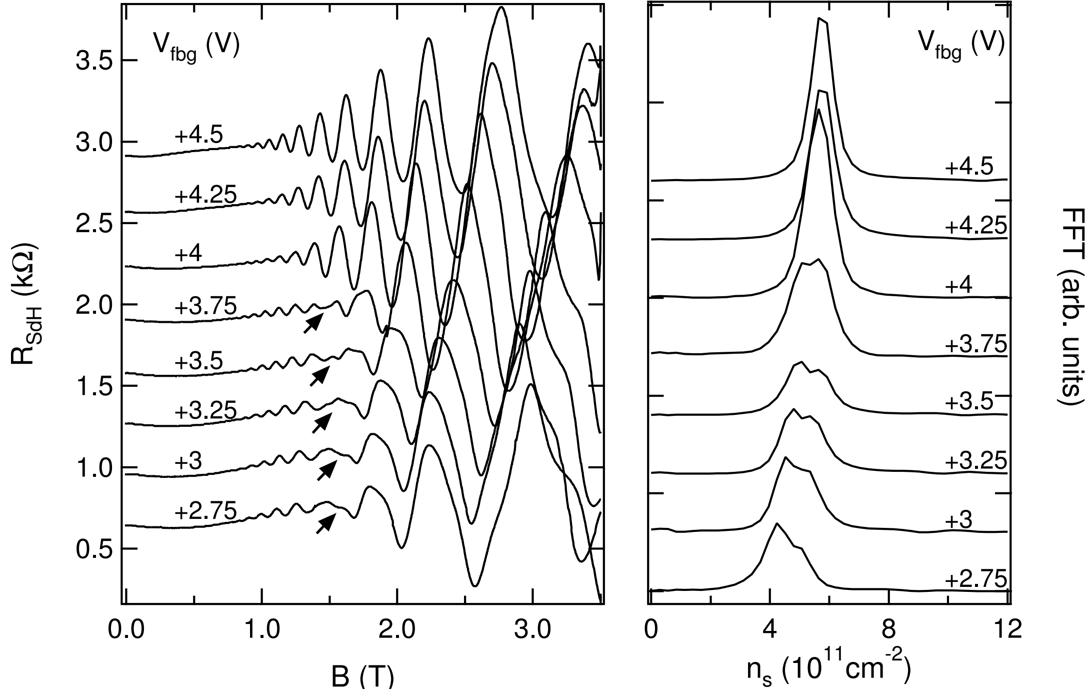


**Fig. 5.12:** Data recorded for a conventional Hall-bar. A fixed front-gate voltage of $V_{fg}$=3 V is applied. All other values of the experiment are the same as those of Fig. 5.11. Distinct beating patterns are observed for $V_{fbg} \leq$3.75 V, and the nodes are marked by arrows. Again, the carrier density distributions determined by FFT displayed on the right side. Two separate peaks of spin non-degenerate subbands are observed in the carrier density distributions for $V_{fbg} \leq$3.75 V. The scaling of the x-axis is selected for spin-degenerate subbands and thus must be halved to correctly yield the carrier densities $n_{\uparrow}$ and $n_{\downarrow}$ of the spin non-degenerate subbands. The SdH traces are offset by 350 Ω. The FFT traces are normalised and offset for clarity.

In the second high-field experiment, the spin-orbit interaction is studied in dependence of a voltage $V_{fbg}$ applied between the front-gate and the back-gate. Measurements are performed on a conventional Hall bar processed in Atsugi at a temperature of 280 mK, applying an AC current bias of 35 nA at a frequency of 190.1 Hz. Both longitudinal magnetoresistance and Hall-voltage across the sample are recorded simultaneously. The magnetoresistance is recorded for a series of voltages $V_{fbg}$ at a fixed voltage $V_{fg}$ applied between front-gate and InAs channel. For $V_{fbg}$=0 V, SdH oscillations are observed when $V_{fg}$ exceeds 2 V. Beating patterns in the SdH oscillations are observed at $V_{fg}$=2.5 V and $V_{fg}$=3 V. Figures 5.11 and 5.12 show the experimental results for front-gate voltages of $V_{fg}$=2.5 V and $V_{fg}$=3 V, respectively. Beating patterns with clear nodes can be seen up to $V_{fbg}$=4 V for $V_{fg}$=2.5 V and up to $V_{fbg}$=3.75 V for $V_{fg}$=3 V. The carrier density distributions displayed on the right sides of Figures 5.11 and 5.12 are determined from the experimental data by FFT. The carrier density distribution exhibits two peaks for all voltages, at which beating patterns can be observed in the SdH oscillations. The two peaks correspond to the carrier densities $n_{\uparrow}$ and $n_{\downarrow}$ of the spin non-degenerate subbands. Exact values of $n_{\uparrow}$ and $n_{\downarrow}$ are determined by fitting Gaussians to the carrier density distributions. The Rashba spin-orbit interaction parameter $\alpha$ is determined from $n_{\uparrow}$ and $n_{\downarrow}$ according to the parabolic approximation Eq.(2.16). Fig. 5.13 shows

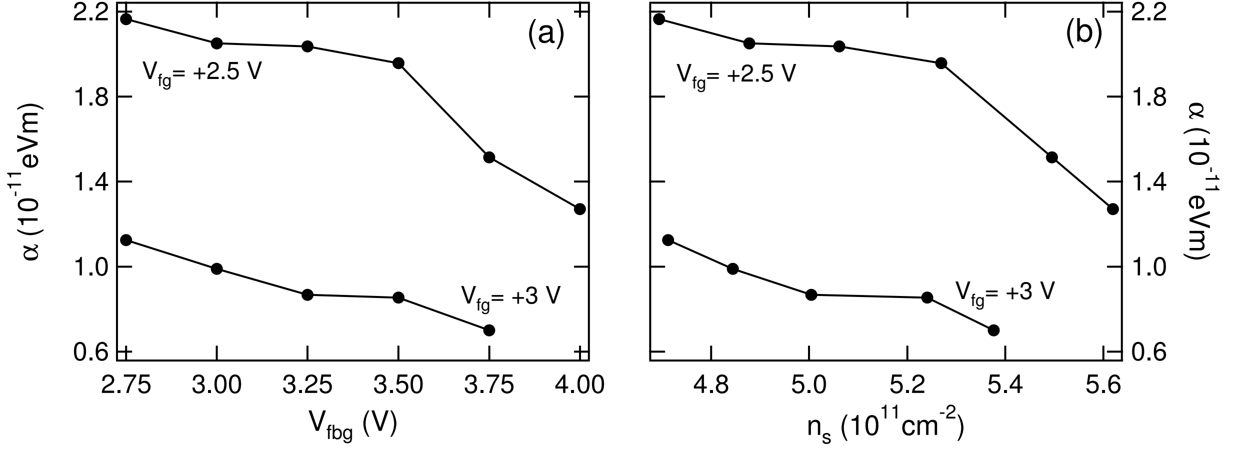


**Fig. 5.13:** Rashba parameters $\alpha$ determined by applying a voltage $V_{fbg}$ between front-gate and back-gate for fixed front gate voltages $V_{fg}$. The results are calculated from the subband carrier densities of the SdH oscillations displayed in Figures 5.11 and 5.12.

the resulting values for $\alpha$, both in dependence of $V_{fbg}$ and in dependence of the carrier density $n_s$. The carrier density $n_s$ is determined independently from Hall-voltages and from the SdH oscillations according to $n_s = n_\uparrow + n_\downarrow$. Both methods yield identical values for $n_s$, which is found to increase linearly with $V_{fbg}$. In Fig. 5.13, one can observe a decrease of $\alpha$ with increasing $V_{fbg}$ for both $V_{fg}$=2.5 V and $V_{fg}$=3 V. Comparing the Rashba parameters obtained for the two front-gate voltages, one finds $\alpha$ at $V_{fg}$=3 V to be approximately half of that at $V_{fg}$=2.5 V.
The carrier density is controlled by $V_{fbg}$ and is found to be almost independent of $V_{fg}$. In contrast, the Rashba parameter is primarily controlled by $V_{fg}$, and only a slight influence of $V_{fbg}$ can be observed. Thus, independent control of the Rashba parameter at a given carrier density can be obtained by fixing $V_{fbg}$ and tuning $\alpha$ by changing $V_{fg}$. The increase of $\alpha$ from $V_{fg}$=+3 V to $V_{fg}$=+2.5 V is found to be over 100%.

## 5.6 Discussion

The dependence of spin-orbit interaction on a voltage $V_{fg}$ between the front-gate and the InAs channel is studied by WAL and by SdH oscillations. With both methods, the Rashba parameter $\alpha$ is successfully obtained for carrier densities ranging from $n_s$=3.5$\cdot$10$^{11}$ cm$^{-2}$ to 7.5$\cdot$10$^{11}$ cm$^{-2}$. Fig. 5.14 shows the resulting values for $\alpha$, along with those obtained from the band-structure simulations presented in Section 5.1. For display purposes, the Rashba parameters determined from SdH oscillations, using the parabolic approximation in Eq. (2.16), are shown one order of magnitude smaller than their actual values.
The values for $\alpha$ determined from SdH oscillations are an order of magnitude larger than both those obtained from WAL and those calculated from band structures. In all three cases, the values of $\alpha$ do not only show a clear decrease of $\alpha$ with increasing $n_s$, but in particular the same qualitative dependence on the carrier density. The Rashba parameters determined from SdH oscillations show a slight deviation for carrier densities above 6$\cdot$10$^{11}$ cm$^{-2}$, at which a strong decrease of $\alpha$

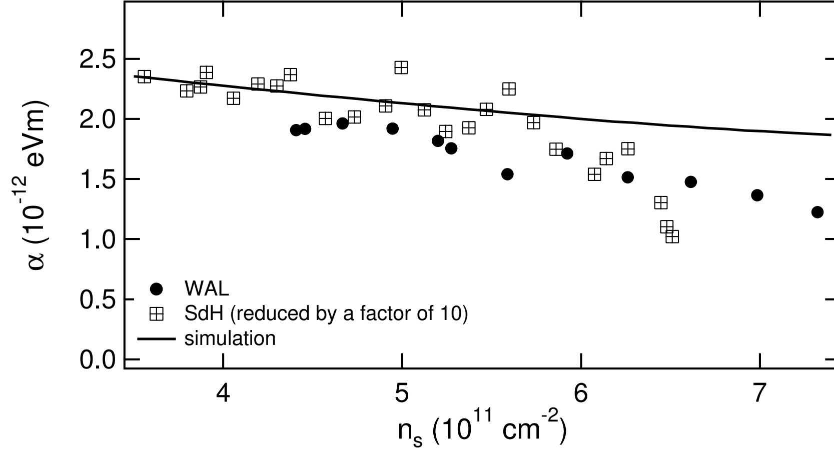


**Fig. 5.14:** Rashba parameters obtained for various values of $V_{fg}$. Results from WAL experiments are depicted as closed markers, results from SdH oscillations as open markers, and results from simulations are displayed as a solid line. For display purposes, the values from the SdH oscillations have been divided by a factor of ten. Both experimental methods and the calculations yield an identical dependence of $\alpha$ on $n_s$. However, the values obtained by SdH oscillations are increased over those obtained by the other two methods by an order of magnitude.

is observed: at these high carrier densities the subband carrier densities $n_\uparrow$ and $n_\downarrow$ overlap in the carrier density distribution, making their exact values and thus $\alpha$ difficult to determine.
Quantitatively, the values determined from WAL are found to be reduced a little over the calculated values. These slight deviations are caused by unknown values in the band-structure calculations: to accurately determine the band structure, the position of the Fermi energy must be known at both the InAs channel region and at the sample surface. Below the channel, the Fermi energy is pinned to the donator levels of the carrier supply layer. This approximates the experimental circumstances, in which the front gate voltage $V_{fg}$ is biased against the InAs channel. At the sample surface, the Fermi energy of the simulations is positioned relative to the conduction band according to $E - E_F = -e \cdot V_{fg}$ ($e$: elementary charge). A change of the pinning of the Fermi energy affects the electric field $\mathscr{E}_z$ across the channel (and thus $\alpha_f$) and results in a shift in the electron probability $|\Psi|^2$. A different $|\Psi|^2$ results in an altered boundary contribution $\alpha_b$, as discussed above. Varying the pinning affects both the field and the boundary contribution, and thus the total Rashba parameter $\alpha_{tot} = \alpha_f + \alpha_b$. Estimates show that the differing values of $\alpha$ obtained from WAL and from band-structure calculations can be explained by the chosen pinning of the Fermi energy.
The increase of the values for $\alpha$ determined from SdH oscillations by an order of magnitude over those from WAL and those calculated from the band structures is not easily explicable. Errors arising from data analysis can be ruled out through repeated diligent analysis and qualitative comparison with other experiments. Furthermore, the values of $\alpha$ determined from SdH oscillations are of the same order of magnitude as those obtained from SdH oscillations in similar samples by Grundler [Gru00]. To date, the discrepancy between the results determined by WAL in low magnetic fields and those determined from SdH oscillations in high magnetic fields cannot be explained. The fact that this discrepancy is present in fields as low as a few Tesla is particularly puzzling. The strength of the magnetic field alone may not be sufficient to assess the influence of

a magnetic field on the spin-orbit interaction. Possibly, the strength must be considered in terms of $\mu \cdot B$ instead.
As magnetoconductance experiments on the InAs-HEMTs show distinct WAL, spin-dephasing must be governed by D'yakonov-Perel (DP) scattering at near-zero magnetic fields [Kna96]. However, the DP theory predicts decrease of $\alpha$ with increasing magnetic field. This was also shown in recent experiments by Meijer *et. al.* [Mei04]. The increase of $\alpha$ with increasing B observed in the experiments of this chapter, would require another scattering mechanism to become dominant in the InAs-HEMTs at higher magnetic fields. When Eliott-Yaffett scattering dominates, $\alpha$ increases with increasing magnetic field, as shown in reference [Kik98]. Further experiments are required to determine the influence of external magnetic fields on the Rashba parameter $\alpha$. Measurements of WAL in a static magnetic field $B$ applied parallel to the 2DEG, such as in Reference [Mei04], could be used to determine the strength of $\alpha$ over a wide range of magnetic fields.
Both WAL and SdH oscillations are recorded in dependence of a voltage $V_{fbg}$, applied between front-gate and back-gate of the InAs-HEMT. When $V_{fbg}$ is applied, WAL can be observed when the InAs remains floating, and SdH oscillations can be observed when a voltage $V_{fg}$ is applied between the front-gate and the InAs channel. Due to this, the results of the two experiments cannot be compared. But, in both cases regions of $V_{fbg}$ (and $V_{fg}$) are found, in which the Rashba parameter $\alpha$ is tunable independent of the carrier density $n_s$. In WAL experiments, $\alpha$ can be tuned by about 17% at a carrier density of $n_s$=4.45$\cdot 10^{11}$ cm$^{-2}$, in SdH oscillation experiments $\alpha$ can be tuned by about 100% at carrier densities ranging from 4.7$\cdot 10^{11}$ cm$^{-2}$ to 5.4$\cdot 10^{11}$ cm$^{-2}$.
The key parameter in spintronic devices is the spin precession angle $\Delta\theta$. For transport through a 2DEG of length L, the difference $\Delta\theta(L)$ of spin-precession angles for spin-orbit interactions of $\alpha_{max}$ and $\alpha_{min}$ can be calculated with Eq.(2.6). The mean free path of an electron can be approximated as $\langle L \rangle = v_F \tau_e$, with the Fermi velocity $v_F$ and the elastic scattering time $\tau_e$ [Dat95]. For the InAs-HEMTs with a mobility of $\mu$=170.000 cm$^2$/Vs and a carrier density of $n_s$=4.45$\cdot 10^{11}$ cm$^{-2}$, one obtains a mean free path of $\langle L \rangle \simeq$1.9 $\mu$m. Over the length of 1.9 $\mu$m, $\Delta\theta$ can be estimated to 31°, using the values for $\alpha_{max}$ and $\alpha_{min}$ determined from WAL experiments. The difference in precession angle of $\Delta\theta$=31° should be easily observed in spin-transport devices such as proposed in reference [Dat90]. In the case of Rashba parameters determined from SdH oscillations, a full 360° precession of the electron spin already occurs after 738 nm for $V_{fg}$=+3 V and $n_s$=5.0$\cdot 10^{11}$ cm$^{-2}$. As $\alpha$ is more than doubled when $V_{fg}$ is reduced to +2.5 V, the difference in precession angle $\Delta\theta$ can be tuned between 0° and 360°.

# 6 InAlAs/InGaAs heterostructures

Heterostructures with an InAlAs/InGaAs quantum well are suitable to study the influence of boundaries on spin-orbit interaction: both InGaAs and InAlAs can be lattice matched to InP, facilitating the growth of InGaAs/InAlAs quantum wells with and without an intermediate InP layer at an interface. In this chapter, the design of the heterostructures used as well as the sample geometries are introduced. Also, simulations and experiments to determine the strength of spin-orbit interaction are presented. The chapter closes with an overview of the results.
The InAlAs/InGaAs heterostructures presented in this chapter were grown at NTT Advanced Technology in Japan. All processing and all experiments on these structures were performed within the scope of a trainee period in the spintronics research group of Dr. J. Nitta at the Basic Research Labs of the Nippon Telegraph & Telephone corporation (NTT-BRL) in Atsugi, Japan.

## 6.1 Material system

The heterostructures used in this chapter's experiments are grown by metal-organic chemical vapour deposition (MOCVD). The channels are made of $In_{0.53}Ga_{0.47}As$, the channel boundaries of $In_{0.52}Al_{0.48}As$ or InP. All three materials are lattice matched with a lattice constant of 5.88 Å [Iba99]. The band gaps are 757 meV for $In_{0.53}Ga_{0.47}As$, 1338 meV for $In_{0.52}Al_{0.48}As$, and

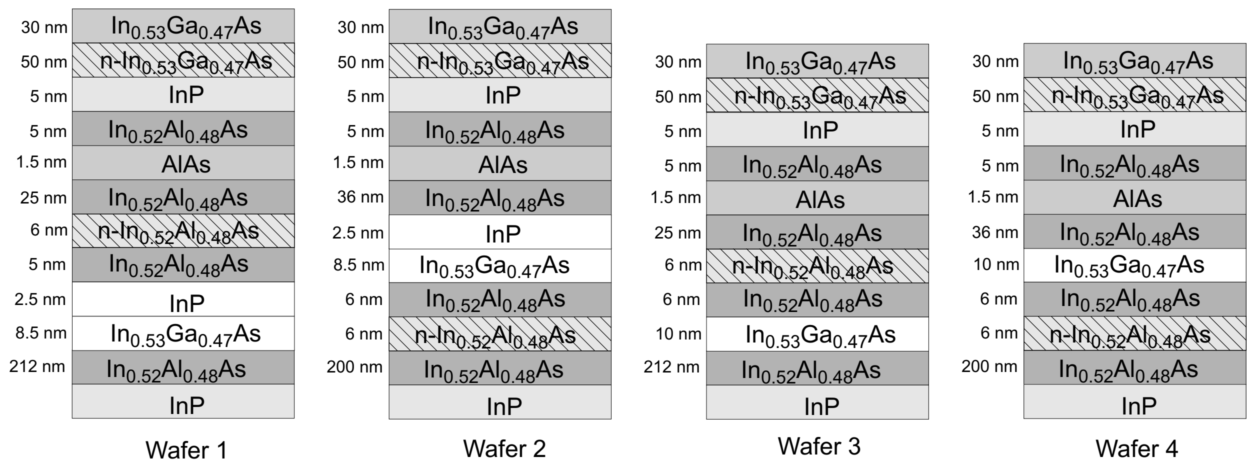


**Fig. 6.1:** Schematics of the four heterostructures with an $In_{0.53}Ga_{0.47}As$ channel. The channel areas are marked in white and the doped layers are hatched. The carrier supplying layers are positioned above the channel for Wafer 1 and Wafer 3, and below the channel for Wafer 2 and Wafer 4. Wafer 1 and Wafer 2 feature an intermediate InP layer at the upper channel boundary. During sample processing, the three topmost layers are removed.

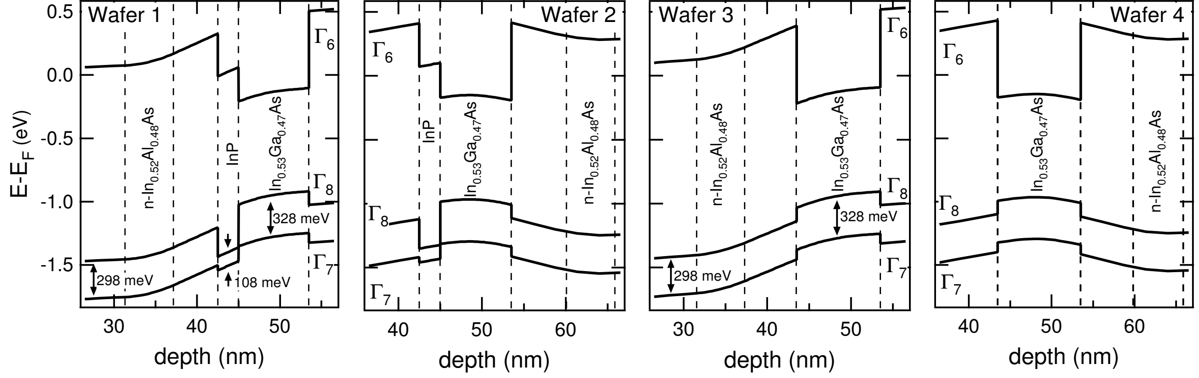


**Fig. 6.2:** Band structures of the heterostructures with an $In_{0.53}Ga_{0.47}As$ channel. All bands are displayed as relative energies with respect to the Fermi energy $E_F$, and versus the depth below the sample surface. The four separate images display results of simulations for Wafer 1 to Wafer 4, from left to right. The $\Gamma_6$ conduction band, the $\Gamma_8$ valence band and the $\Gamma_7$ spin split-off band are shown for the channel region. The relevant materials, and in the leftmost figure the spin split-off energies, are denoted. Simulations were performed with nextnano[3] [Vog].

1384 meV for InP, and the respective spin split-off energies of the valence band are 328 meV, 298 meV, and 108 meV (all at T=0). A 2DEG is formed in the quantum well, the effective electron mass of which is determined to be $m^* = 0.041 \cdot m_e$ [Kog02]. Spin-orbit interaction in InGaAs/InAlAs quantum wells is found to be dominated by SIA so that BIA can be neglected [Sch98]. Two constituents of SIA can be distinguished, as was shown in Section 2.1.2: the effect of an electric field across the channel as well as effects of wave-function penetration at the channel boundaries. Four different wafers are grown to study the interplay between these so-called field and boundary contributions. The layer structures of these wafers are shown in Fig. 6.1 and the band structures are displayed in Fig. 6.2. The sign of the field contribution $\alpha_f$ to the Rashba parameter depends only on the sign of the electric field $\mathscr{E}_z = -\frac{d\varphi}{dz} = \frac{1}{e}\frac{dE_{\Gamma_6}}{dz}$ ($\varphi$: electrical potential, $E_{\Gamma_6}$: energy of the conduction band edge) across the channel (cf. Eq.(2.9)). Two samples with different signs of $\mathscr{E}_z$ were designed, one with a carrier supply layer above the channel (Wafer 3) and one with a carrier supply layer below the channel (Wafer 4). Donator doping was used for the carrier supply layers, with concentrations of $2.5{\cdot}10^{18}$ cm$^{-3}$ for layers above the channel and $2.0{\cdot}10^{18}$ cm$^{-3}$ for layers below the channel. Counter-doping with acceptors was performed at the

| | top doping | bottom doping |
|---|---|---|
| InP | Wafer 1 | Wafer 2 |
| no InP | Wafer 3 | Wafer 4 |

| $\alpha_{tot} =$ | $\alpha_f$ | + | $\alpha_b$ |
|---|---|---|---|
| Wafer 1 | + | | + |
| Wafer 2 | - | | + |
| Wafer 3 | + | | (+) |
| Wafer 4 | - | | (-) |

**Table 6.1:** Overview of the wafers with an $In_{0.53}Ga_{0.47}As$ channel. The left table clarifies the features of each wafer. The right table lists the signs of the field and the boundary contributions $\alpha_f$ and $\alpha_b$ to the total Rashba parameter $\alpha_{tot}$. Brackets mark negligible contributions.

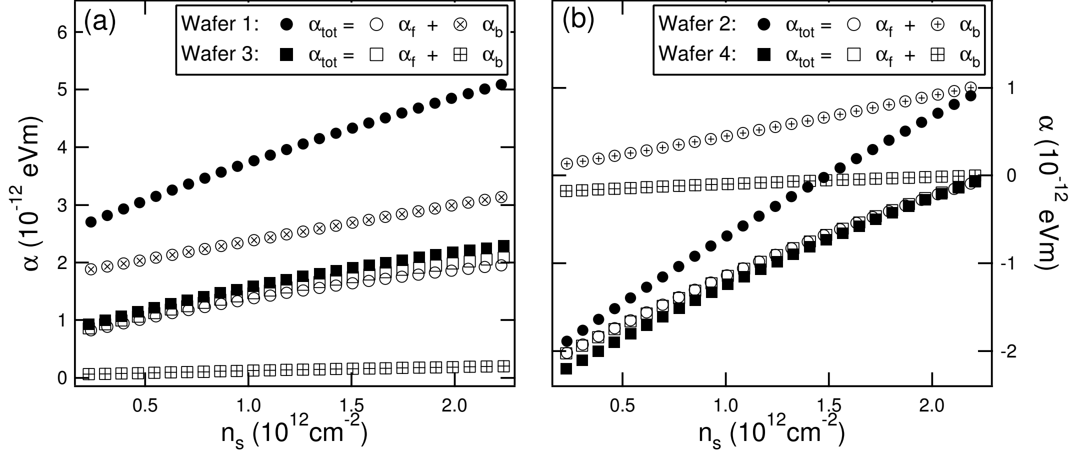


**Fig. 6.3:** Rashba parameters in dependence of the carrier density as calculated from simulated band structures. The values for the field and boundary contributions $\alpha_f$ and $\alpha_b$ are depicted as well as the total Rashba parameter $\alpha_{tot}$. (a) results for the two wafers with doping layers above the channel; (b) results for the two wafers with doping layers below the channel. The values for $\alpha$ were calculated according to Eq.(2.9) and Eq.(2.10). The band-structure calculations were performed using nextnano$^3$ [Vog].

$In_{0.52}Al_{0.48}As$/substrate interface. The doping concentrations differ so as to obtain similar carrier densities of the 2DEG in not-gated samples. As can be seen from the simulated band structures, $\mathscr{E}_z$ points in direction of the substrate for Wafer 3 and in direction of the sample surface for Wafer 4. Thus, for the quantum well structure used, the field contribution to the Rashba parameter is expected to be positive for wafers with a carrier supply layer above the channel and negative for wafers with a carrier supply layer below the channel.

Two more samples were designed, using the two basic designs presented in the last paragraph. These feature an intermediate InP layer at the upper InGaAs/InAlAs quantum well boundary. The width of the channel was set to obtain similar carrier densities as in the samples without an InP layer. The boundary contribution $\alpha_b$ to the Rashba parameter is given by Eq.(2.10). This is in general small and of the same sign as the field contribution for symmetric quantum wells with a symmetric material structure, i.e. boundaries of the same material on both sides of the channel. When an InP layer is inserted, an interesting situation arises at the InP/$In_{0.53}Ga_{0.47}As$ interface: the $\Gamma_8$ valence band energy in InP is lower than the $\Gamma_7$ spin split-off band energy in $In_{0.53}Ga_{0.47}As$. Therefore, $\alpha_b$ is greatly enhanced when an InP layer is inserted at one channel boundary. In addition, the sign of $\alpha_b$ is determined by the position of the InP layer, being positive for an InP layer positioned above the channel and negative for an InP layer positioned below the channel. Thus, the intermediate InP layer at the upper channel boundary should lead to an enhanced positive contribution to the total Rashba parameter $\alpha_{tot}$. Table 6.1 gives an overview of both the key structural features of the wafers used and the expected signs of $\alpha_f$ and $\alpha_b$. Transport experiments only yield the absolute value of $\alpha_{tot}$, and not the sign. Insertion of an InP layer at the upper channel boundary should thus increase the absolute value of $\alpha_{tot}$ for structures with a carrier supply layer above the channel and reduce it for structures with a carrier supply layer below the channel. Therefore, $\alpha_{tot}$ in Wafer 1 is expected to be increased with respect to Wafer 3 and $\alpha_{tot}$ in Wafer 2 is expected to

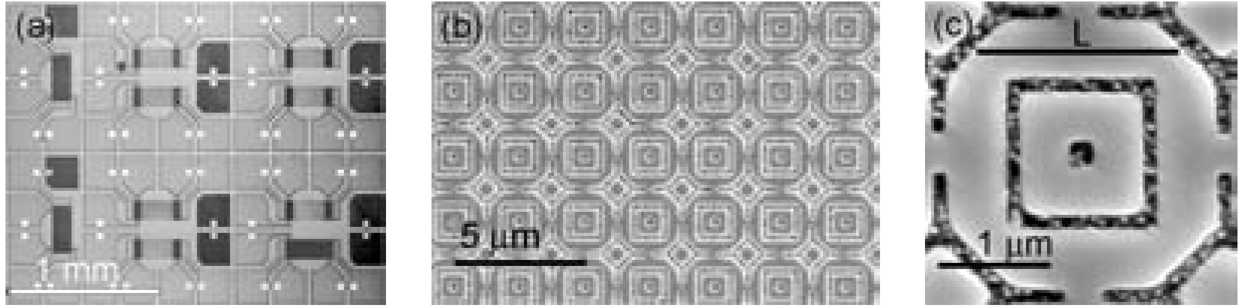


**Fig. 6.4:** SEM images of an interferometer sample: (a) Overview of a quarter of the sample. At the left, two Hall-bars (two vertically aligned dark grey rectangles) can be identified. The seven arrays of interferometers of different side lengths L (horizontally aligned light grey rectangles) are positioned to the right of the Hall-bars. (b) Section of an interferometer array. (c) Image of an individual interferometer. The side length L is marked.

be decreased with respect to Wafer 4.

The band structures of the four wafers were calculated for various surface-gate voltages which directly correspond to the carrier density, using the self-consistent Schrödinger-Poisson solver *nextnano*$^3$ [Vog]. The field and boundary contributions to $\alpha_{tot}$, determined according to Equations (2.9) and (2.10), are displayed in Figure 6.3. The results are displayed separately for wafers with the carrier supply layer above and below the channel. To increase the carrier density, a positive voltage is applied to the gate, thus increasing the potential at the sample surface. Therefore $\alpha_f$ increases with increasing carrier density for the top-doped wafers and decreases for the bottom-doped wafers. The values of $\alpha_f$ are found to be virtually identical for the corresponding wafers with and without an intermediate InP layer. In the case of the back-doped samples, $\alpha_b$ is not only increased by insertion of an InP layer at the upper channel boundary, but also changes sign. Thus, an inserted InP layer at the upper boundary actually increases the total Rashba parameter $\alpha_{tot}$ for samples with a carrier-supply layer above the channel and decreases $\alpha_{tot}$ for samples with a carrier supply layer below the channel.

## 6.2 Sample geometries

Hall-bars are used to measure WAL, and microstructured interferometers are used for the measurements of AAS oscillations. To ensure consistent results for both WAL and AAS experiments, Hall-bar and interferometer geometries must be implemented on an identical 2DEG. Both sample geometries are processed in parallel, using one piece of semiconductor heterostructure. First, selective wet chemical etching is used to remove the three topmost layers of the wafers (marked by hatches in Fig. 6.1). These layers were incorporated to pin the Fermi energy above the channel in future experiments. After removal of the top layers, patterning of the interferometers is performed by electron-beam lithography and subsequent RIE etching. Seven arrays with different interferometer lengths are made, each of these structured a total of four times at different dosages of electron-beam exposure. After this the Hall-bars, contact leads, and mesas are defined by wet chemical etching, thus setting the interferometers free from the surrounding 2DEG. Gates are placed above

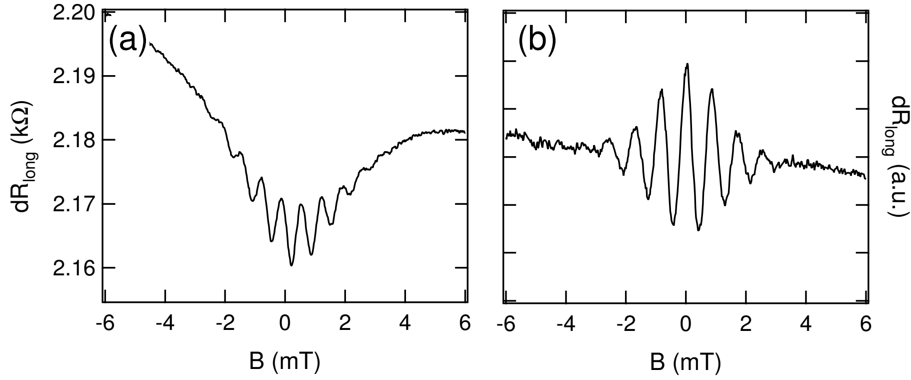


**Fig. 6.5:** Exemplary AAS oscillations. (a) Raw data before FFT filtering: a strong background magnetoresistance can be observed. (b) Data after FFT high-pass filtering.

the Hall-bars and interferometers, insulated from the semiconductor by a 115 nm thick $SiO_2$ oxide. Unnecessary $SiO_2$ is removed by RIE etching. Finally, contact to the semiconductor is made by deposition of AuGeNi and subsequent annealing at 275 °C. A section of a completed sample can be seen in Fig. 6.4(a). The Hall-bars have a length of 250 $\mu$m and a width of 125 $\mu$m. The individual structures in the square-loop interferometer arrays feature side lengths from 1.2 $\mu$m to 1.8 $\mu$m. A section of an array of interferometers as well as a single interferometer are displayed in Fig. 6.4(b,c).

## 6.3 Experiments

Three different kinds of experiments are performed to determine the strength of the spin-orbit interaction in the $In_{0.52}Al_{0.48}As/In_{0.53}Ga_{0.47}As$ heterostructures: measurements of WAL, SdH oscillations, and AAS oscillations. WAL is suitable to determine the Rashba parameter $\alpha$ at low electron mobilities, AAS oscillations require high electron mobilities to ensure ballistic transport, and SdH can only be observed for higher carrier densities and higher mobilities. The Hall mobilities of the samples used were determined to range from 20.000 $cm^2/Vs$ to 100.000 $cm^2/Vs$, depending on the gate voltage.
Transport experiments are performed with an AC-bias current[1] of approximately 35 nA, modulated at a frequency of 190.1 Hz. Both the Hall-bars and the interferometer arrays feature contacts to detect a voltage perpendicular to the direction of current. These contacts are used to determine the carrier density for each measurement[2]. The carrier density, rather than the gate voltage, is used as a scale to enable comparison between samples.
SdH oscillations were observed for magnetic fields above approximately 1.5 T. Neither did the oscillations exhibit beating patterns in any of the four wafers, nor was spin-splitting of the carrier density distribution calculated by Fourier transform found. Thus, no value for $\alpha$ could be deter-

[1]To account for non-ideal current sources as well as variations in the sample resistance, the bias current is monitored by means of a lock-in amplifier.

[2]The carrier density $n_s$ is determined according to following equation [Dat95]: $n_s = \frac{I/|e|}{dV_H/dB_\perp}$, with $I$: bias current, $e$: elementary charge, $V_H$: Hall voltage, $B_\perp$ magnetic field perpendicular to the 2DEG plane.

mined from the SdH oscillations. Previous experiments showed, that the spin-orbit interaction can be nonzero, even if the SdH oscillations show no beating patterns [Kog02]. In that case, the strength of the spin-orbit interaction can be determined from experiments in low magnetic fields. Therefore, in the following, the focus will be on such low-field measurements of WAL and AAS oscillations. Both WAL and AAS oscillations were studied for various structures on each of the four heterostructures presented above. WAL was observed for Wafer 1 and Wafer 4, and weak localisation for Wafer 2. AAS oscillations were observed for all four wafers.

Analysis of WAL is performed as follows: recorded magnetoconductance is fit according to the theory of Iordanski, Lyanda-Geller, and Pikus described in Eq.(2.20). To obtain objective results, the 'curve fit' procedure of the IGOR Pro data analysis package is used, whereby the ILP theory is implemented by means of an XOP (cf. Appendix B). Curve fitting yields the characteristic spin-orbit field $H_{so}$, from which the Rashba parameter $\alpha$ is determined according to Eq.(2.24).

Experimentally recorded AAS oscillations show background magnetoresistance. Before analysis can be performed, this background is removed by frequency-selective filtering: a high-pass filter in terms of the magnetic field $B$ is implemented by means of a Fast Fourier Transform (FFT). Fig. 6.5 shows exemplary raw AAS oscillations as well as data, from which the zero- and low frequency components in $B$ have been removed by FFT filter.

To determine the Rashba parameter $\alpha$ from AAS oscillations, measurements at various strengths of spin-orbit interaction are required. In the InGaAs/InAlAs heterostructures investigated, the strength of spin-orbit interaction can be tuned by a gate voltage [Lin05]. Therefore, AAS oscillations are recorded at various gate voltages. The amplitudes of the oscillations are determined for each gate voltage and, ideally, an oscillatory dependence is found. The angle of spin precession $\Delta\theta$ along each side of the interferometer can now be obtained as a function of the gate voltage: the experimentally determined gate voltage dependent AAS oscillation amplitudes are compared to the calculated spin precession angle $\Delta\theta$ dependent oscillation amplitudes, which are described in Fig. 2.7 and Eq.(2.26). The Rashba parameter is then determined from $\Delta\theta$ according to Eq.(2.6). The required points of reference for $\alpha$ are obtained from the analysis of WAL.

In the following, the experimental results on each of the four wafers are presented individually. For each wafer, the WAL experiments are shown first, followed by the AAS oscillations. The results on all four wafers are summarized and discussed at the end of the section. The values of the magnetic field have been shifted by 4.2 mT for all of the following experiments to account for the hysteresis of the superconducting magnet used.

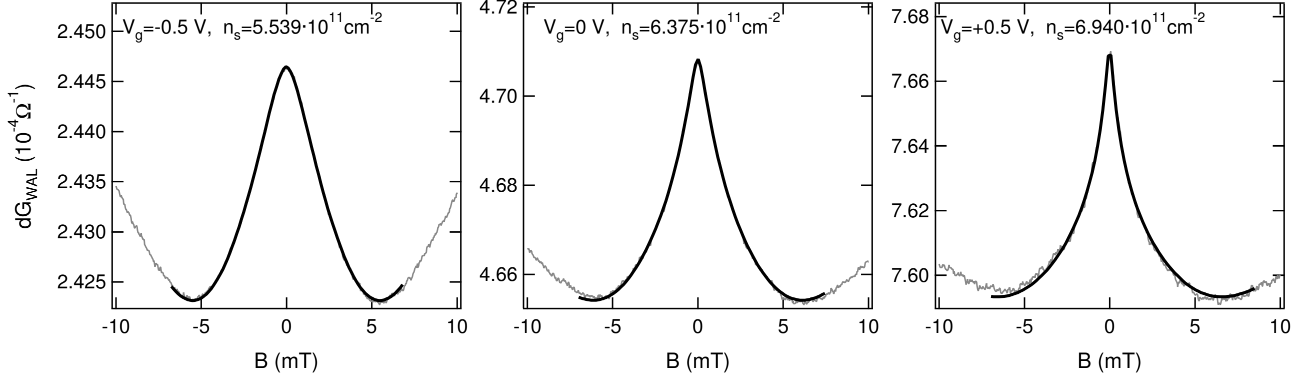


**Fig. 6.6:** Low-field magnetoconductances recorded on Wafer 1 for three gate voltages. Pronounced WAL is observed. The best fits with ILP theory are shown as solid lines. The carrier densities were determined from Hall voltages recorded simultaneously with WAL.

## Wafer 1

In Wafer 1, WAL could be observed at gate voltages from -0.75 V to 1.25 V, which correspond to carrier densities between $5.1 \cdot 10^{11}$ cm$^{-2}$ and $7.7 \cdot 10^{11}$ cm$^{-2}$. Magnetoconductances recorded at three gate voltages as well as fits with ILP theory are displayed in Figure 6.6. The values for the Rashba parameter $\alpha$ resulting from the fits as well as the carrier densities determined by Hall probes are displayed in Table 6.2. The fit parameter $H_{so}$, which is decisive in determining $\alpha$, is also given. An increase of the Rashba parameter with increasing carrier density is observed.
AAS oscillations could be observed in interferometers of a side length of 1.8 $\mu$m for gate voltages between 1 V and 9.25 V. These gate voltages correspond to carrier densities between $1.1 \cdot 10^{12}$ cm$^{-2}$ and $2.2 \cdot 10^{12}$ cm$^{-2}$. A set of recorded AAS traces for various gate voltages is displayed in Fig. 6.7. The resulting oscillation amplitude is normalised and displayed as a function of the carrier density in Fig. 6.8. The amplitude of the oscillation is found to increase steadily up to a carrier density of $n_s \sim 1.8 \cdot 10^{12}$ cm$^{-2}$, at which saturation occurs. A reliable value for the Rashba parameter cannot be determined from the AAS amplitudes, as at least half a period of oscillation is required.

| $V_g$ (V) | $n_s$ (cm$^{-2}$) | $H_{so}$ (mT) | $\alpha$ (eVm) |
|---|---|---|---|
| -0.75 | $5.11 \cdot 10^{12}$ | 4.42 | $4.82 \cdot 10^{-12}$ |
| -0.5 | $5.54 \cdot 10^{12}$ | 4.80 | $5.02 \cdot 10^{-12}$ |
| 0 | $6.37 \cdot 10^{12}$ | 5.22 | $5.24 \cdot 10^{-12}$ |
| 0.5 | $6.94 \cdot 10^{12}$ | 5.59 | $5.41 \cdot 10^{-12}$ |
| 1.25 | $7.71 \cdot 10^{12}$ | 5.88 | $5.56 \cdot 10^{-12}$ |

**Table 6.2:** Results of WAL experiments on Wafer 1. The carrier density $n_s$ is obtained from the Hall voltage, the characteristic spin-orbit interaction field $H_{so}$ from fits to the experimental data of Fig.6.6 according to ILP theory, and $\alpha$ from $H_{so}$ given by Eq. 2.24.

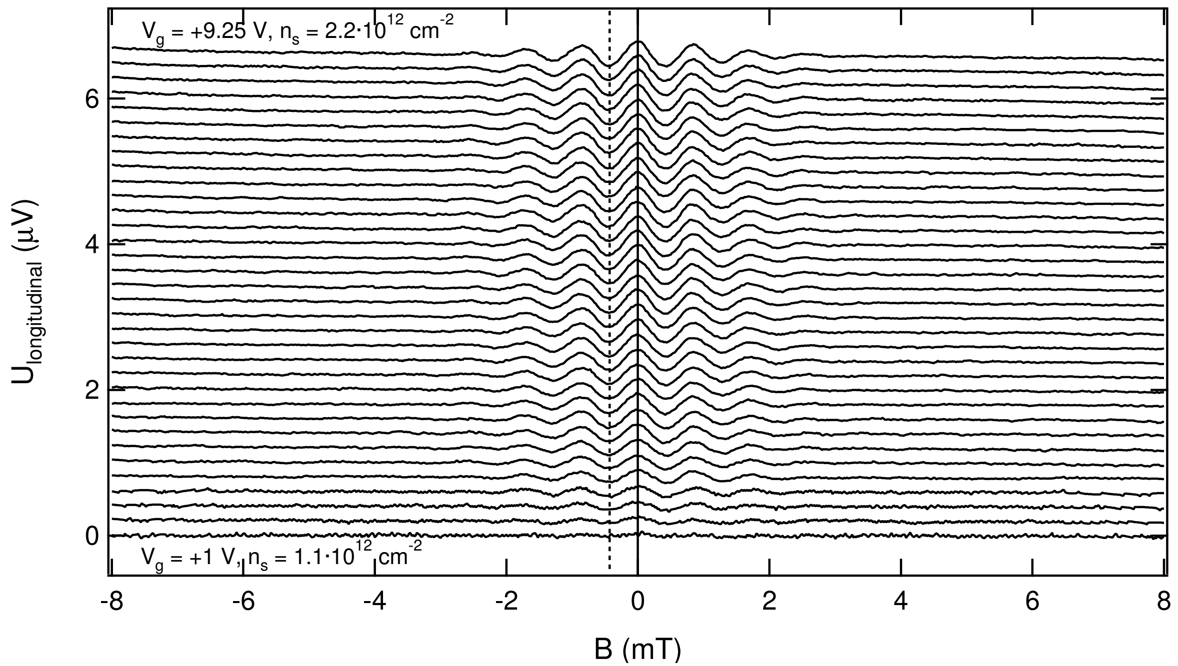


**Fig. 6.7:** Overview of AAS oscillations recorded on Wafer 1. All traces were recorded within a single cooling cycle. Each trace corresponds to single gate voltage, i.e. a carrier density. The gate voltage was increased in steps of 0.25 V between each trace, starting from 1 V at the bottom trace. The interferometers used have a side length 1.8 $\mu$m. As a guide to the eye, a solid line marks the center maximum and a dashed line first minimum at lower magnetic fields. All traces have been FFT filtered and are offset for clarity.

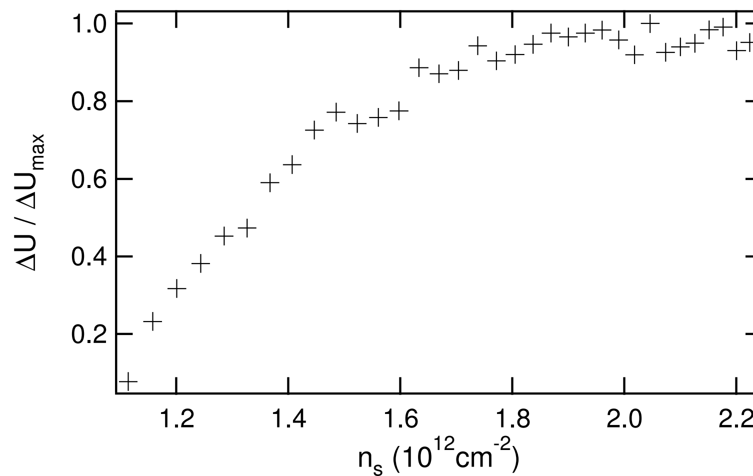


**Fig. 6.8:** Normalised amplitude of the AAS oscillations recorded on Wafer 1 as displayed in Fig. 6.7. The amplitude is determined as difference between the center maximum and the first minimum at lower magnetic fields and displayed in dependence of the carrier density. An increase in amplitude can be observed for carrier densities up to $1.8 \cdot 10^{12}$ cm$^{-2}$, at which saturation occurs.

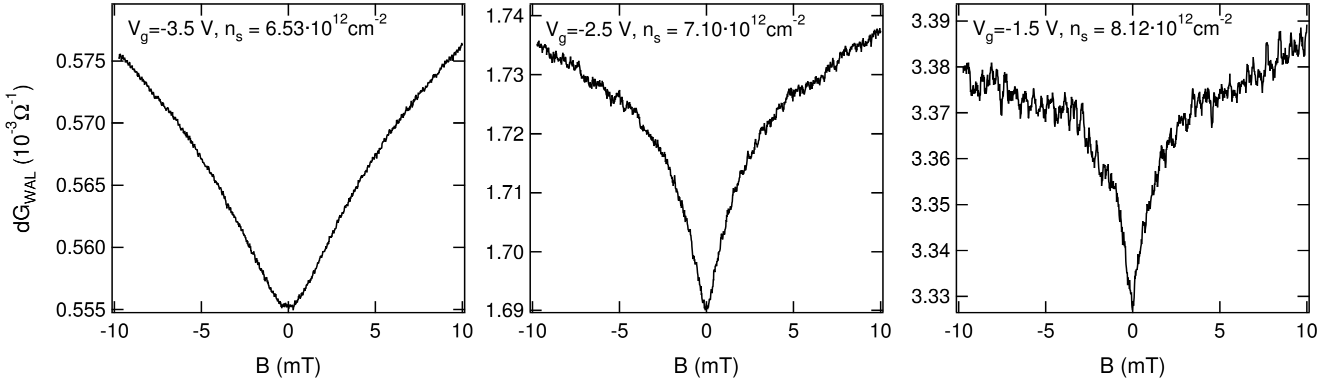


**Fig. 6.9:** Low-field magnetoconductances recorded on Wafer 2 for three gate voltages. Distinct weak localisation is observed, but no weak antilocalisation. Thus no fits are performed. The carrier densities were determined from Hall voltages recorded at the same time as the weak localisation.

## Wafer 2

In Wafer 2, WAL experiments were performed for gate voltages between -3.5 V and 0, which correspond to carrier densities between $6.5 \cdot 10^{12}$ cm$^{-2}$ and $9.1 \cdot 10^{12}$ cm$^{-2}$. For gate voltages of -3 V and above, weak localisation was observed. WAL was not observed at any gate voltage so that fitting could not be performed, and no value for the Rashba parameter $\alpha$ determined. Recorded magnetoconductances for three different gate voltages are displayed in Figure 6.9.
AAS oscillations could be observed in interferometers of 1.5 $\mu$m side length for various gate voltages between 1 V an 20 V. These gate voltages correspond to carrier densities ranging from $1.5 \cdot 10^{12}$ cm$^{-2}$ to $2.5 \cdot 10^{12}$ cm$^{-2}$. A set of AAS traces recorded for various gate voltages is displayed in Fig. 6.10. The resulting oscillation amplitude is normalised and displayed as a function of the carrier density in Fig. 6.11. The AAS amplitude shows oscillatory dependence on the carrier density. However, no sign change of the amplitude can be observed so that no Rashba parameter can be ascertained. Previous experiments predicted the Rashba parameter in Wafer 2 to be very small or near-zero ($\alpha < 10^{-12}$ eVm) for the carrier densities studied. This is a possible cause of the abnormal carrier density dependence of the AAS amplitude.

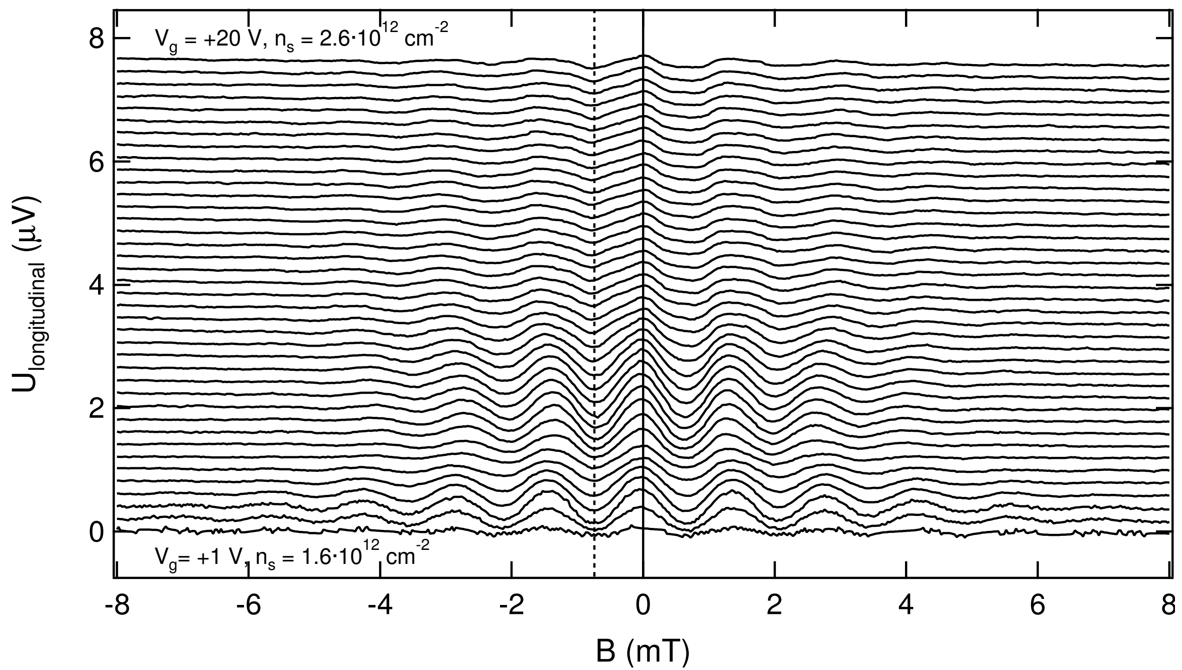


**Fig. 6.10:** Overview of AAS oscillations recorded on Wafer 2. All traces were recorded within a single cooling cycle. Each trace corresponds to a single gate voltage, i.e. a carrier density. The gate voltage was increased in steps of 500 mV between each trace, starting from 1 V at the bottom trace. The interferometers used have a side length 1.5 $\mu$m. As a guide to the eye, a solid line marks the center maximum and a dashed line the first minimum at lower magnetic fields. All traces have been FFT filtered and are offset for clarity.

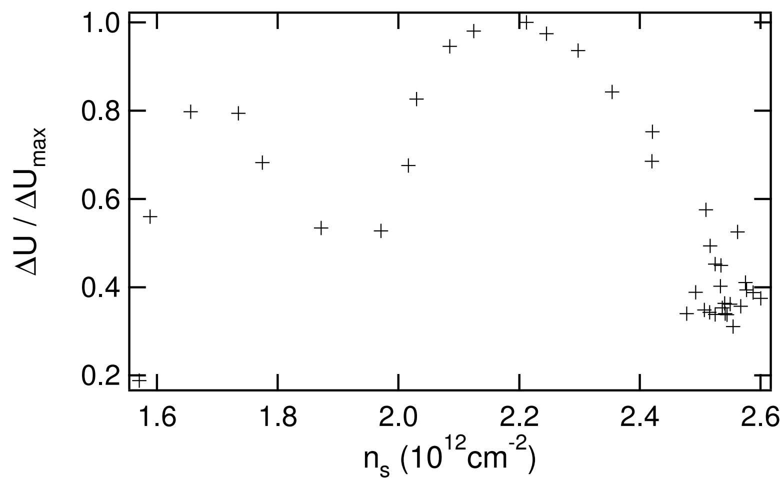


**Fig. 6.11:** Normalised amplitude of the AAS oscillations recorded on Wafer 2 as displayed in Fig. 6.10. The amplitude is determined as difference between the center maximum and the first minimum at lower magnetic fields and displayed in dependence of the carrier density. An oscillation in amplitude can be observed, however no sign changes. Thus the significance of the oscillation is unclear.

### Wafer 3

Low-field magnetoconductance experiments were performed on Hall-bars on Wafer 3 for gate voltages from -2.25 V to +1 V which correspond to carrier densities between $3.9 \cdot 10^{11}$ cm$^{-2}$ and $9.1 \cdot 10^{11}$ cm$^{-2}$. Neither weak localisation nor weak antilocalisation could be observed.
AAS oscillations could be observed in interferometers of 1.5 $\mu$m side length for various gate voltages between 0 and 15 V. These gate voltages correspond to carrier densities ranging from $7.8 \cdot 10^{11}$ cm$^{-2}$ to $1.8 \cdot 10^{12}$ cm$^{-2}$. A set of AAS traces recorded for various gate voltages is displayed in Fig. 6.12. The resulting oscillation amplitude is normalised and displayed as a function of the carrier density on the left side of Fig. 6.13. An oscillation of the center amplitude is found, whereby saturation occurs for carrier densities above $1.4 \cdot 10^{12}$ cm$^{-2}$. WAL results from previous experiments by Lin *et al.* [Lin05] are used as points of reference. This is deemed acceptable as the WAL results of previous experiments agree well with the results gathered in this thesis for all other wafers. With these points of reference the Rashba parameter is calculated from the AAS oscillation amplitude. The precession angles and corresponding Rashba parameters are presented as a function of the carrier density in the table on the right side of Fig. 6.13.

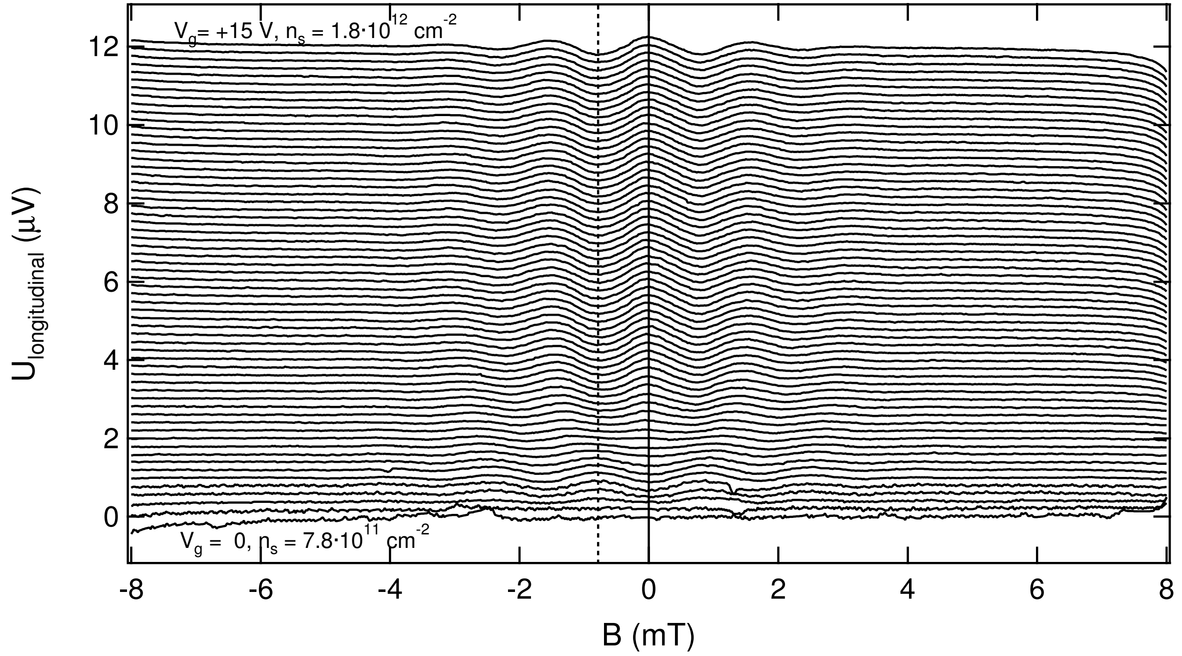


**Fig. 6.12:** Overview of AAS oscillations recorded on Wafer 3. All traces were recorded within a single cooling cycle. Each trace corresponds to a single gate voltage, i.e. carrier density. The gate voltage was increased in steps of 250 mV between each trace, starting from 0 at the bottom trace. The interferometers used have a side length 1.5 $\mu$m. As a guide to the eye, a solid line marks the center extremum and a dashed line the first extremum at lower magnetic fields. All traces have been FFT filtered and are offset for clarity.

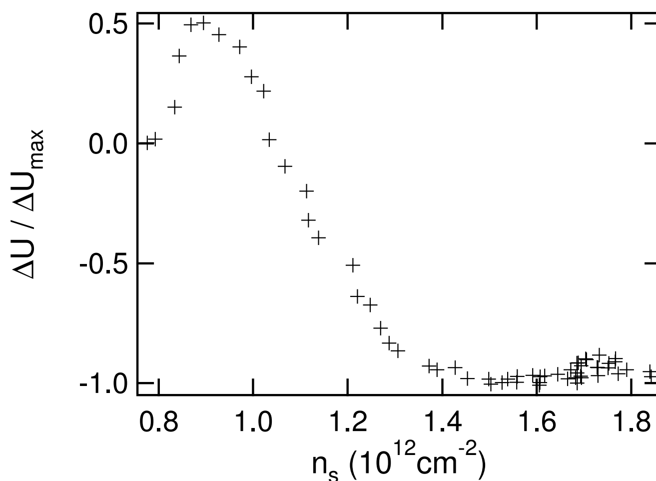


| $n_s$ (cm$^{-2}$) | $\Delta\theta$ | $\alpha$ (eVm) |
|---|---|---|
| 0.88·10$^{12}$ | $\pi$ | 1.95·10$^{12}$ |
| 1.04·10$^{12}$ | 1.178 $\pi$ | 2.29·10$^{12}$ |
| 1.45·10$^{12}$ | 1.3768 $\pi$ | 2.68·10$^{12}$ |

**Fig. 6.13: left:** Normalised amplitude of the AAS oscillations recorded on Wafer 3 as displayed in Fig. 6.12. The amplitude is determined as difference between the center extremum and the first extremum at lower magnetic fields and displayed in dependence of the carrier density. A three-quarter oscillation of the amplitude can be observed. The amplitude saturates for carrier densities above 1.4·10$^{12}$ cm$^{-2}$. **right:** Spin precession angles $\Delta\theta$ and Rashba parameters $\alpha$ determined by AAS oscillations in Wafer 3. The precession angles are calculated for a path length of 1.5 $\mu$m.

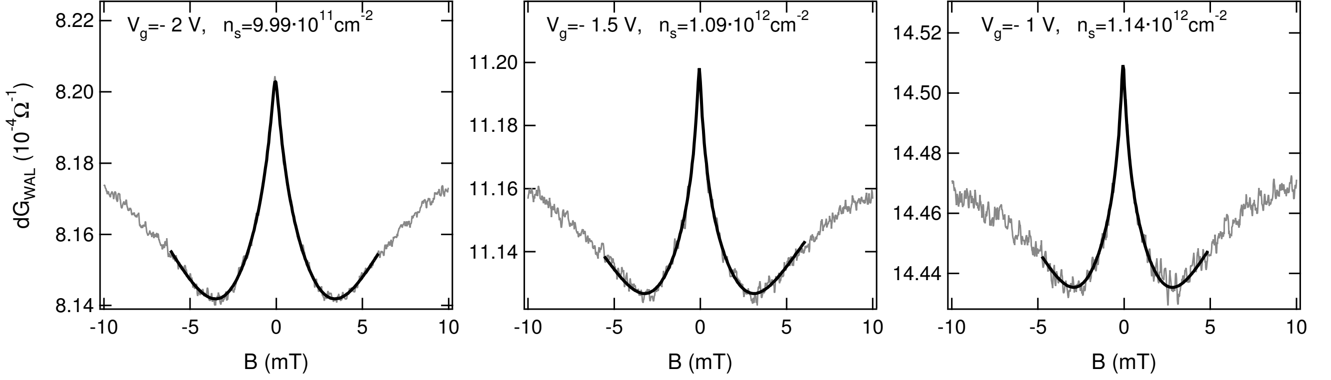


**Fig. 6.14:** Low-field magnetoconductances recorded on Wafer 4 for three gate voltages. Pronounced WAL is observed. The best fits with ILP theory are shown as solid lines. The carrier densities were determined from Hall voltages recorded simultaneously with WAL.

## Wafer 4

In Wafer 4, WAL could be observed at gate voltages from -1 V to -0.5 V which correspond to carrier densities between $1.0 \cdot 10^{12}$ cm$^{-2}$ and $1.2 \cdot 10^{12}$ cm$^{-2}$. Magnetoconductances recorded at three gate voltages as well as fits with ILP theory are displayed in Figure 6.14. The values for the Rashba parameter $\alpha$ resulting from the fits as well as the carrier densities determined by Hall probes are displayed in Table 6.3. The fit parameter $H_{so}$, which is decisive in determining $\alpha$, is also given. A decrease of $\alpha$ with increasing carrier density is observed.

AAS oscillations could be observed in interferometers of a side length of 1.6 $\mu$m for gate voltages between 2.5 V and 10 V. These gate voltages correspond to carrier densities between $1.55 \cdot 10^{12}$ cm$^{-2}$ and $2.42 \cdot 10^{12}$ cm$^{-2}$. A set of recorded AAS traces for various gate voltages is displayed in Fig. 6.15. The resulting oscillation amplitude is normalised and displayed as a function of the carrier density on the left side of the Fig. 6.16. An almost perfect oscillation of the amplitude in dependence of the carrier density is observed. Reliable Rashba parameters can be determined from this. The resulting values are displayed on the right side of Fig. 6.16.

| $V_g$ (V) | $n_s$ (cm$^{-2}$) | $H_{so}$ (mT) | $\alpha$ (eVm) |
|---|---|---|---|
| -2 | $9.99 \cdot 10^{12}$ | 2.95 | $3.93 \cdot 10^{-12}$ |
| -1.5 | $10.88 \cdot 10^{12}$ | 2.69 | $3.76 \cdot 10^{-12}$ |
| -1 | $11.41 \cdot 10^{12}$ | 2.43 | $3.57 \cdot 10^{-12}$ |
| -0.5 | $12.15 \cdot 10^{12}$ | 2.22 | $3.41 \cdot 10^{-12}$ |

**Table 6.3:** Results of WAL experiments on Wafer 4. The carrier density $n_s$ is obtained from the Hall voltage, the characteristic spin-orbit interaction field $H_{so}$ from fits to the experimental data of Fig.6.14 according to ILP theory, and $\alpha$ from $H_{so}$ as given by Eq. 2.24.

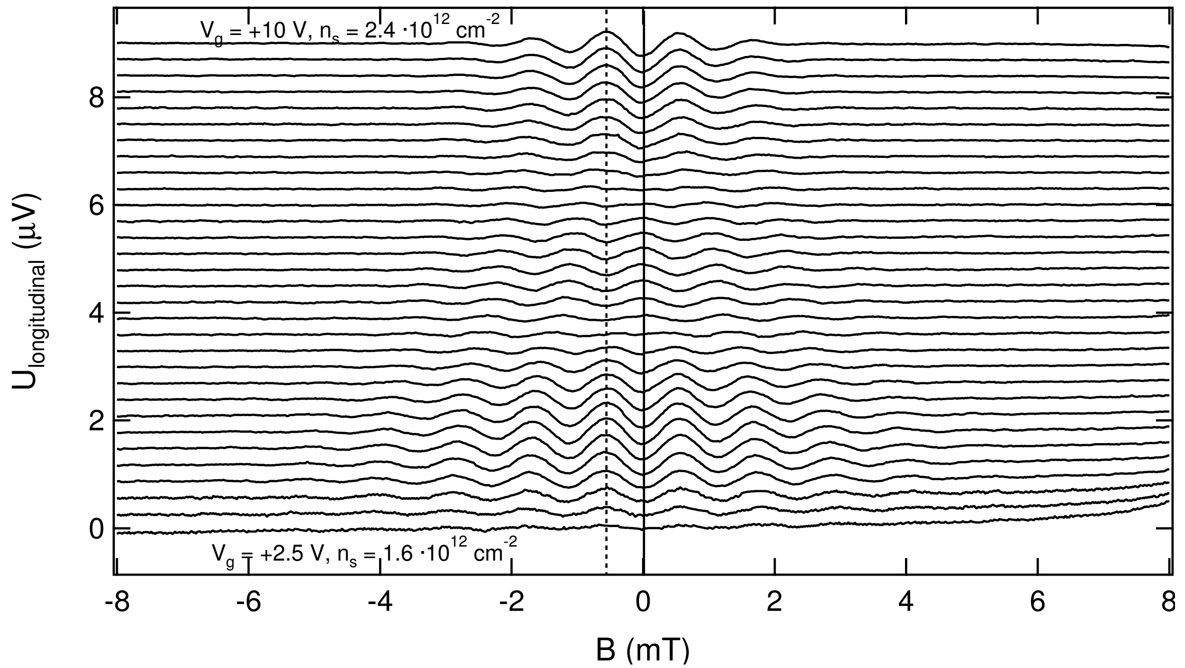


**Fig. 6.15:** Overview of AAS oscillations recorded on Wafer 4. All traces were recorded within a single cooling cycle. Each trace corresponds to single gate voltage, i.e. carrier density. The gate voltage was increased in steps of 250 mV between each trace, starting from 2.5 V at the bottom trace. The interferometers used have a side length 1.6 $\mu$m. As a guide to the eye, a solid line marks the center extremum and a dashed line the first extremum at lower magnetic fields. All traces have been FFT filtered and are offset for clarity.

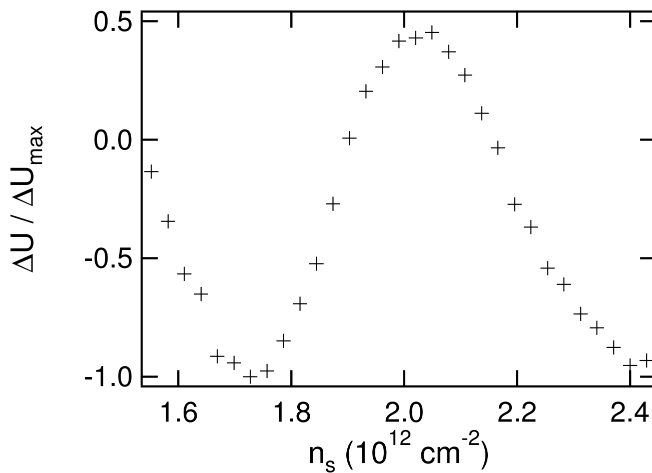


| $n_s$ (cm$^{-2}$) | $\Delta\theta$ | $\alpha$ (eVm) |
|---|---|---|
| $1.5 \cdot 10^{12}$ | $1.576\ \pi$ | $2.88 \cdot 10^{-12}$ |
| $1.725 \cdot 10^{12}$ | $1.364\ \pi$ | $2.49 \cdot 10^{-12}$ |
| $1.912 \cdot 10^{12}$ | $1.178\ \pi$ | $2.15 \cdot 10^{-12}$ |
| $2.0 \cdot 10^{12}$ | $\pi$ | $1.83 \cdot 10^{-12}$ |
| $2.162 \cdot 10^{12}$ | $0.822\ \pi$ | $1.50 \cdot 10^{-12}$ |
| $2.4 \cdot 10^{12}$ | $0.636\ \pi$ | $1.16 \cdot 10^{-12}$ |

**Fig. 6.16: left:** Normalised amplitude of the AAS oscillations recorded on Wafer 4 as displayed in Fig. 6.15. The amplitude is determined as difference between the center extremum and the first extremum at lower magnetic fields and displayed in dependence of the carrier density. Almost perfect oscillatory behavior of the amplitude is observed. **right:** Spin precession angles $\Delta\theta$ and Rashba parameters $\alpha$ determined by AAS oscillations in Wafer 4. The precession angles are calculated for a path length of 1.6 $\mu$m.

## Discussion

Both WAL and AAS oscillations are observed in the heterostructures with an InGaAs/InAlAs quantum well. The strength of the Rashba parameter $\alpha$ is determined for various carrier densities: analysis of WAL yields $\alpha$ for Wafer 1 and Wafer 4, and analysis of AAS oscillations yields $\alpha$ for Wafer 3 and Wafer 4. An overview of the experimentally obtained Rashba parameters is displayed in Fig. 6.17 as a function of the carrier density. In addition, the absolute values of the Rashba parameters calculated from simulated band structures, as described in Section 6.1, are displayed as solid lines. The absolute values are sufficient for comparison with the experimental results, as experiments yield only the magnitude of the Rashba parameter, but not the sign. The results of WAL experiments by Lin *et al.* [Lin05] on the same wafers are also displayed in Fig. 6.17. Qualitatively, the experimental and theoretical results show the same dependence of $\alpha$ on the carrier density: samples with a doping layer above the channel (Wafer 1 and Wafer 3) show an increase of $\alpha$ with increasing carrier density, and samples with a doping layer below the channel (Wafer 2 and Wafer 4) show a decrease of $\alpha$ with increasing carrier density. For doping layers above the channel, the insertion of an intermediate InP layer at the upper channel boundary increases the strength of the Rashba parameter as both field and boundary contribution to $\alpha$ are of the same sign: the Rashba parameter of the wafer with an inserted InP layer (Wafer 1) is enhanced compared to the wafer without an InP layer (Wafer 3). For doping layers below the channel, an intermediate InP layer at the upper channel boundary decreases $\alpha$, as the field and boundary contributions are of opposite sign and partially compensate each other: the Rashba parameter of the wafer with an inserted InP layer (Wafer 2) is reduced compared to the wafer without an InP layer (Wafer 4).

Quantitatively, the experimentally determined Rashba parameters are enhanced over the calculated ones for all wafers except for Wafer 2. The values for $\alpha$ in Wafer 1 and Wafer 4 are significantly larger than the theoretical predictions. Because of this, the differences in $\alpha$ induced by inserting an intermediate InP layer at the upper quantum well boundary are roughly doubled in the case of samples with a doping layer above the channel (Wafer 1/Wafer 3) and roughly tripled in the case of samples with a doping layer below the channel (Wafer 2/Wafer 4). This can only be explained by considering both the field and the boundary contribution. The field contribution $\alpha_f$ is virtually independent of the presence of an intermediate InP layer at a quantum well boundary. In fact, it only depends on the position of the carrier-supply layer, i.e. if this layer is positioned above or below the channel. As the boundary contribution $\alpha_b$ can be neglected for symmetric quantum wells, the enhanced value of $\alpha$ in samples without an InP layer (Wafer 3 and Wafer 4) must be due to an enhanced value of $\alpha_f$.

Insertion of an InP layer mainly affects the boundary contribution, but not the field contribution. Therefore, the increased difference in $\alpha$, that is observed when an InP layer is inserted at the upper channel boundary, can be ascribed to an increased boundary contribution.

Such a joint amplification of $\alpha_f$ and $\alpha_b$ is brought forth by different choices of the Fermi energy pinning in the band-structure calculations: to accurately determine the band structure, the position of the Fermi energy must be known both at the InP substrate/$In_{0.52}Al_{0.48}As$ buffer layer interface and at the sample surface. Because of the counter doping with acceptors, the Fermi energy was set to correspond to the upper valence band energy at the buffer/substrate interface. However, the

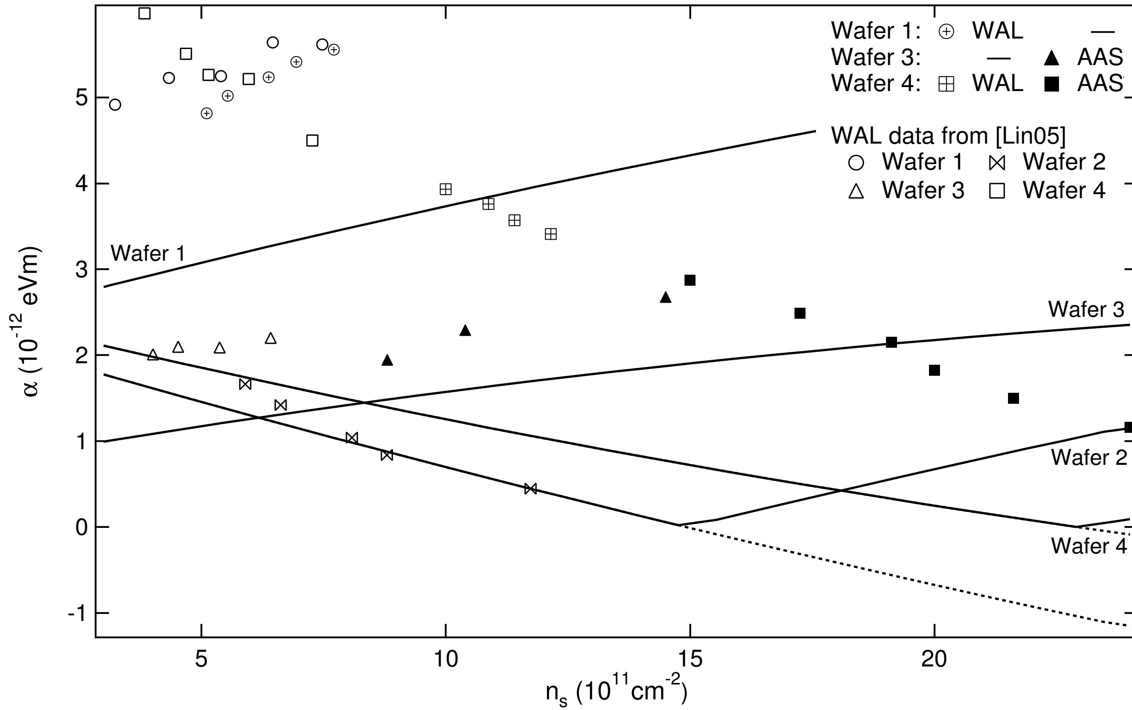


**Fig. 6.17:** Overview of the experimentally and theoretically determined Rashba parameters. Closed symbols represent results of experiments performed within this thesis, open symbols are from experiments performed on the same wafers by Lin *et al.* [Lin05]. The absolute values of the Rashba parameters calculated from simulated band structures as described in Section 6.1 are depicted as solid lines. Dashed lines continue the calculated values for Wafer 2 and Wafer 4 through zero.

exact position of the Fermi energy at the sample surface is not known. Changing the pinning of the Fermi energy at the sample surface not only changes the electric field $\mathscr{E}_z$ across the channel and thus the associated $\alpha_f$, but also shifts the charge distribution and thus the corresponding electron wave function $\Psi$ across the channel. The changed shape of $\Psi$ affects the boundary contribution, as each boundary at position $z_i$ is weighted by $|\Psi(z_i)|^2$. Different choices of pinning also explain the variations between the simulation results presented here and those presented in reference [Lin05]. Further experiments and calculations with a defined Fermi energy at the sample surface are necessary to obtain quantitative agreement of the values for $\alpha$. The same wafers used in the experiments presented here may be used, however the three topmost layers of the wafers should not be removed. The three topmost layers contain a heavily n-doped layer, which fixes the Fermi energy to the lower conduction band edge at the sample surface.

The experiments of this chapter clearly show the interplay between the field and the boundary contribution to the Rashba parameter in InAlAs/InGaAs quantum wells. It is shown that the field contribution dominates in symmetric quantum wells (Wafer 3 and Wafer 4), and that the sign of $\alpha$ is then set by the direction of the electric field $\mathscr{E}_z$ across the channel. In quantum wells with an intermediate InP layer at the upper quantum well boundary (Wafer 1 and Wafer 2), the boundary contribution if found to be significant. It can be additive or subtractive to the field

contribution, depending on the direction of $\mathscr{E}_z$. Moreover, it was shown that the analysis of AAS oscillations is a powerful tool to determine $\alpha$ in the regime of ballistic transport at high mobilities and high carrier densities. Together with WAL analysis this allows for investigation of spin-orbit interaction in low magnetic fields over a very wide range of mobilities and carrier densities. In this regard, the results on Wafer 4 prove to be especially interesting, as the Rashba parameter could be ascertained for carrier densities from $4{\cdot}10^{11}$ cm$^{-2}$ to $2.5{\cdot}10^{12}$ cm$^{-2}$ by experiments in low magnetic fields (including the results of Lin *et. al* ). The results show consistency over the entire range of carrier density, confirming the potential of WAL and AAS to determine the strength of spin-orbit interaction.

# 7 Outlook and conclusions

In this thesis, low-temperature magnetotransport experiments were used to study spin-orbit interaction in narrow-band III-V semiconductors. The strength of the Rashba parameter $\alpha$ was determined by means of three different experimental techniques: the established method of Shubnikov-de Haas (SdH) oscillations recorded in high applied magnetic fields, and weak antilocalisation (WAL) as well as Al'tshuler-Aronov-Spivak (AAS) oscillations in near-zero external magnetic fields. Three different material systems were studied: inversion layers on p-type InAs single crystals, heterostructures with InAs/$In_{0.75}Al_{0.25}As$ quantum wells, and heterostructures with $In_{0.53}Ga_{0.47}As/In_{0.52}Al_{0.48}$ quantum wells.

To study the influence of external magnetic fields, spin-orbit interaction in the inversion layers and in the InAs/$In_{0.75}Al_{0.25}As$ quantum wells was determined from SdH oscillations and by WAL for the same range of carrier densities. In addition, the Rashba parameter $\alpha$ was acquired from simulated band-structures. For both samples, the values of $\alpha$ determined from WAL are found to agree well with the theoretical values. However, the results obtained from SdH oscillations in high magnetic fields disagree: these are increased over the Rashba parameters obtained in low magnetic fields by WAL. In the inversion layers, the increase of $\alpha$ in high magnetic fields is only slight. However, the two experimental techniques yield results of opposite dependence on the carrier density. In the quantum wells, the Rashba parameters obtained in high magnetic fields are increased over those in low fields by about an order of magnitude. But, both show identical dependence on the carrier density. The stronger effect of an applied magnetic field on $\alpha$ in the quantum wells is surprising. An external magnetic field should influence the electron spin primarily via the Zeeman effect, which depends on the strength of the field and on the $g$-factor. But, the magnetic field applied to measure SdH oscillations was almost three times larger for the inversion layers than for the quantum wells. Also, the electron $g$-factor of crystalline p-type InAs is more than double that of the heterostructures [Möl03], making the Zeeman contribution in the inversion layers about six times of that in the quantum wells. Possibly, the field strength and $g$-factor do not suffice in assessing the influence of a magnetic field. Instead, the strength of the quantum effects caused by the magnetic field in terms of the field-mobility product $\mu \cdot B$ may need to be considered.

Independent control of spin-orbit interaction and carrier density is achieved in InAs/$In_{0.75}Al_{0.25}As$ heterostructures with an ingrown back-gate. Samples were studied by magnetotransport experiments, while voltages were applied to the back-gate and to a front-gate above the quantum well. When a voltage $V_{fbg}$ was applied between front-gate and back-gate, distinct WAL was observed when the quantum well remained floating, and SdH oscillations were recorded when an additional voltage $V_{fg}$ was applied between front-gate and quantum-well. By varying $V_{fbg}$, the Rashba parameter was changed without affecting the carrier density. A relative change in $\alpha$ of 17% at a carrier density of $4.45 \cdot 10^{11}$ cm$^{-2}$ was observed by using WAL as means of detection. Using SdH

oscillations to determine $\alpha$, relative changes of over 100% were observed, while the carrier density could be tuned almost independently between $4.7{\cdot}10^{11}$ cm$^{-2}$ and $5.4{\cdot}10^{11}$ cm$^{-2}$. The key parameter of spin transport in spin devices is the spin-precession angle. The mean free path of the conduction electrons in the quantum wells is about 1.9 $\mu$m, so that the differences in spin precession angle effected by the changes in $\alpha$ can be estimated to 31° and to over 360° for the results from WAL and SdH, respectively.

The interplay of the field and boundary contributions to the Rashba parameter were studied in $In_{0.53}Ga_{0.47}As/In_{0.52}Al_{0.48}$ quantum wells. Four samples were grown, implementing all possible combinations of positive or negative electric fields across the quantum well and symmetric or asymmetric channel boundaries. The sign of the electric field was fixed by the position of the doping layer, and the symmetry of the channel boundaries was broken by insertion of an InP layer at the upper $In_{0.53}Ga_{0.47}As/In_{0.52}Al_{0.48}$ interface. Using low magnetic-field techniques, the spin-orbit interaction was quantified over a wide range of carrier densities: in the regime of diffusive transport, values of $\alpha$ were obtained from WAL, while they were obtained from AAS oscillations in the regime of higher mobilities at higher carrier densities. Independence of the field and boundary contributions is ascertained by comparing the results of all four samples. The field contribution depends solely on the electric field across the channel. The boundary contribution is found to be positive and greatly enhanced in presence of the InP layer. Depending on the sign of the electric field, additive or subtractive behaviour of the field and boundary contributions are observed.

Questions and challenges that arose during the work presented here encourage further study of spin-orbit interaction in narrow-gap III-V semiconductors. The advances made provide the insight necessary to design further experiments and first devices. Further investigation, both in experiment and in theory, is necessary to fully understand the effects of an external magnetic field on the strength of spin-orbit interactions. To study this experimentally, methods to quantify the Rashba parameter over a wide range of magnetic field strengths must be developed. The back-gated InAs-based heterostructures are most interesting, and hold many possibilities for further research: independent tuning of spin-orbit interaction and carrier density is the prerequisite for many spin-devices, and also obviates effects caused by changes in carrier density.

# A Process parameters

| p-type InAs bulk samples | | | |
|---|---|---|---|
| | **process** | **product / machine** | **parameters** |
| **cleaning** | mech. polish | 1 $\mu$m $Al_2O_3$ solution | 5 cm blob, lvl. 2.9, 25 min |
| | 1st rinse | Tetrahydrofuran | appx. 60°C, 10 min, repeat 1× |
| | 2nd rinse | Isopropanol | spray and blow-dry |
| | chem. polish | 0.0025% Br in Methanol | 25 min |
| | 1st rinse | Methanol | spray and blow-dry |
| | 2nd rinse | Tetrahydrofuran | appx. 60°C, 10 min, repeat 1× |
| | 3rd rinse | Isopropanol | spray and blow-dry |
| **electrodes** | spin coat | Shipley S1813 | ca. 3 drps, 4000 rpm, 60 s, ramp 100 |
| | bake | hotplate | 100°C, 3 min |
| | optical lithography | Karl Suss Maskaligner MJB3 | $Cl_2$, 50 mW/cm$^2$, 6-8 s |
| | develop | Microposit MF319 | 60 s |
| | stop | $H_2O$ | 30 s |
| | barrel | Technics Plasma 100-E | 180 W, 1 Torr $O_2$, 30 s |
| | deposition | Balzers-Pfeiffer PLS500 | 35/10 nm Al/Au, $p \leq 5 \cdot 10^{-8}$mbar |
| | lift-off | Acetone | 12 hrs |
| | rinse | Isopropanol | spray and blow-dry |
| **gate oxide** | PECVD | Oxford Plasmalab 80+ | 450 sccm $SiH_4/N_2$ + 710 sccm $N_2O$, 1 Torr, 150° C, 20W, 7 Min. |
| **gate** | spin coat | Shipley S1813 | ca. 3 drps, 4000 rpm, 60 s, ramp 100 |
| | bake | hotplate | 100°C, 3 min |
| | optical lithography | Karl Suss Maskaligner MJB3 | $Cl_2$, 50 mW/cm$^2$, 6-8 s |
| | develop | Microposit MF319 | 60 s |
| | stop | $H_2O$ | 30 s |
| | deposition | Balzers-Pfeiffer PLS500 | 35/10 nm Al/Au, $p \leq 2 \cdot 10^{-7}$mbar |
| | lift-off | Acetone | 90 min |
| | rinse | Isopropanol | spray and blow-dry |
| **oxide etch** | spin coat | Shipley S1813 | ca. 3 drps, 4000 rpm, 60 s, ramp 100 |
| | bake | hotplate | 100°C, 3 min |
| | optical lithography | Karl Suss Maskaligner MJB3 | $Cl_2$, 50 mW/cm$^2$, 6-8 s |
| | develop | Microposit MF319 | 60 s |
| | stop | $H_2O$ | 30 s |
| | etch | HF 5% | 20 s |
| | stop | $H_2O$ | 1 min |
| | rinse | Acetone, Isopropanol | spray and blow-dry |

| InAs Heterostructures (processed in Hamburg) | | | |
|---|---|---|---|
| | **process** | **product / machine** | **parameters** |
| **backgate contact** | spin coat | Shipley S1813 | ca. 3 drps, 6000 rpm, 60 s, ramp 100 |
| | bake | hotplate | 100°C, 3 min |
| | optical lithography | Karl Suss Maskaligner MJB3 | $Cl_2$, 50 mW/cm$^2$, 6-8 s |
| | develop | Microposit MF319 | 60 s |
| | stop | $H_2O$ | 30 s |
| | barrel | Technics Plasma 100-E | 180 W, 1 Torr $O_2$, 30 s |
| | etch | $H_3PO_4$:$H_2O_2$:$H_2O$, 1:10:100 | 5 min 20 s, cont. stir |
| | deposition | Balzers-Pfeiffer PLS500 | 25/5/25 nm AuGe/Ni/AuGe |
| | lift-off | warm Acetone | 5 min |
| | anneal | oven-room annealer | 380°C, 2 min |
| | rinse | Isopropanol | spray and blow-dry |
| **mesa etch** | spin coat | Shipley S1813 | ca. 3 drps, 6000 rpm, 60 s, ramp 100 |
| | bake | hotplate | 100°C, 3 min |
| | optical lithography | Karl Suss Maskaligner MJB3 | $Cl_2$, 50 mW/cm$^2$, 6-8 s |
| | develop | Microposit MF319 | 60 s |
| | stop | $H_2O$ | 30 s |
| | barrel | Technics Plasma 100-E | 180 W, 1 Torr $O_2$, 30 s |
| | etch | $H_3PO_4$:$H_2O_2$:$H_2O$, 1:10:100 | 30 s, cont. stir |
| | rinse | Acetone, Isopropanol | spray and blow-dry |
| **gate oxide** | PECVD | Oxford Plasmalab 80+ | 450 sccm $SiH_4/N_2$ + 710 sccm $N_2O$, 1 Torr, 280° C, 20W, 7 Min. |
| **gate** | spin coat | Shipley S1813 | ca. 3 drps, 6000 rpm, 60 s, ramp 100 |
| | bake | hotplate | 100°C, 3 min |
| | optical lithography | Karl Suss Maskaligner MJB3 | $Cl_2$, 50 mW/cm$^2$, 6-8 s |
| | develop | Microposit MF319 | 60 s |
| | stop | $H_2O$ | 30 s |
| | deposition | Balzers-Pfeiffer PLS500 | 25/25 nm Al/Au, $p \leq 2 \cdot 10^{-7}$mbar |
| | lift-off | warm Acetone | 5 min |
| | rinse | Isopropanol | spray and blow-dry |
| **oxide etch** | spin coat | Shipley S1813 | ca. 3 drps, 6000 rpm, 60 s, ramp 100 |
| | bake | hotplate | 100°C, 3 min |
| | optical lithography | Karl Suss Maskaligner MJB3 | $Cl_2$, 50 mW/cm$^2$, 6-8 s |
| | develop | Microposit MF319 | 60 s |
| | stop | $H_2O$ | 30 s |
| | barrel | Technics Plasma 100-E | 180 W, 1 Torr $O_2$, 30 s |
| | etch | HF 5% | 20 s |
| | stop | $H_2O$ | 1 min |
| | rinse | Acetone, Isopropanol | spray and blow-dry |

| | process | product / machine | parameters |
|---|---|---|---|
| **bondpads** | spin coat | Shipley S1813 | ca. 3 drps, 6000 rpm, 60 s, ramp 100 |
| | bake | hotplate | 100°C, 3 min |
| | optical lithography | Karl Suss Maskaligner MJB3 | $Cl_2$, 50 mW/cm$^2$, 6-8 s |
| | develop | Microposit MF319 | 60 s |
| | stop | $H_2O$ | 30 s |
| | deposition | Balzers-Pfeiffer PLS500 | 25/5/25 nm AuGe/Ni/AuGe |
| | lift-off | warm Acetone | 5 min |
| | anneal | oven-room annealer | 380°C, 2 min |
| | rinse | Acetone, Isopropanol | spray and blow-dry |

**InAs Heterostructures (processed in Atsugi)**

| | process | product / machine | parameters |
|---|---|---|---|
| **backgate contact** | spin coat | Shipley S1813 | ca. 3 drps, 500/4000 rpm, 5/50 s |
| | bake | hotplate | 100°C, 3 min |
| | optical lithography | Mikasa Maskaligner MA-10 | 20 s |
| | develop | Shipley 352:$H_2O$ 1:5 | 50 s |
| | stop | $H_2O$ | 60 s |
| | clean | Argon RF-sputter | 10 W, $5{\cdot}10^{-3}$ Torr, 1 min |
| | etch | $C_6H_8O_7$ (20%):$H_2O_2$(30%), 20:1 | 7 min 30 s |
| | rinse | Ethanol | spray and blow-dry |
| | spin coat | Shipley S1813 | ca. 3 drps, 500/4000 rpm, 5/50 s |
| | bake | hotplate | 100°C, 3 min |
| | optical lithography | Mikasa MA-10 Maskaligner | 20 s |
| | develop | Shipley 352:$H_2O$ 1:5 | 50 s |
| | clean | Argon RF-sputter | 10 W, $5{\cdot}10^{-3}$ Torr, 1 min |
| | deposition | Neva | 120/120 nm AuGeNi/Au |
| | lift-off | Acetone, ultrasonic | 5 min |
| | anneal | Ulvac RHL-P610CN | 400°C, 1 min |
| | rinse | Ethanol | spray and blow-dry |
| **mesa etch** | spin coat | Shipley S1813 | ca. 3 drps, 500/4000 rpm, 5/50 s |
| | bake | hotplate | 100°C, 3 min |
| | optical lithography | Mikasa Maskaligner MA-10 | 20 s |
| | develop | Shipley 352:$H_2O$ 1:5 | 50 s |
| | stop | $H_2O$ | 60 s |
| | etch | Anelva L-510R-E, $BCl_3$ | 4 min |
| | profile | Tencor $\alpha$-step | |
| | rinse | Acetone, Ethanol | spray and blow-dry |

| | process | product / machine | parameters |
|---|---|---|---|
| **bondpads** | spin coat | Shipley S1813 | ca. 3 drps, 500/4000 rpm, 5/50 s |
| | bake | hotplate | 100°C, 3 min |
| | optical lithography | Mikasa Maskaligner MA-10 | 20 s |
| | develop | Shipley 352:$H_2O$ 1:5 | 50 s |
| | stop | $H_2O$ | 60 s |
| | clean | Argon RF-sputter | 10 W, $5{\cdot}10^{-3}$ Torr, 1 min |
| | deposition | Neva | 60/60 nm AuGeNi/Au |
| | lift-off | Acetone, ultrasonic | 5 min |
| | anneal | Ulvac RHL-P610CN | 275°C, 1 min |
| | rinse | Ethanol | spray and blow-dry |
| **gate oxide** | ECR-CVD | Aftex 6000 ECR | 50 min /115 nm |
| **gate** | spin coat | Shipley S1813 | ca. 3 drps, 500/4000 rpm, 5/50 s |
| | bake | hotplate | 100°C, 3 min |
| | optical lithography | Mikasa Maskaligner MA-10 | 20 s |
| | develop | Shipley 352:$H_2O$ 1:5 | 50 s |
| | stop | $H_2O$ | 60 s |
| | clean | Argon RF-sputter | 10 W, $5{\cdot}10^{-3}$ Torr, 3min |
| | deposition | Neva | 30/60 nm AuGeNi/Au |
| | lift-off | Acetone, ultrasonic | 5 min |
| | rinse | Ethanol | spray and blow-dry |
| **oxide etch** | spin coat | Shipley S1813 | ca. 3 drps, 500/4000 rpm, 5/50 s |
| | bake | hotplate | 100°C, 3 min |
| | optical lithography | Mikasa Maskaligner MA-10 | 20 s |
| | develop | Shipley 352:$H_2O$ 1:5 | 50 s |
| | stop | $H_2O$ | 60 s |
| | clean | Ozone stripper | 20°C, 1 min |
| | etch | $SiO_2$ Samco RIE-10NR | $CHF_3$, 9 min |
| | rinse | Ethanol | spray and blow-dry |

| **Electron-beam lithography JEOL JBX6000FS** | |
|---|---|
| **parameters** | **value** |
| beam current | 100 pA |
| chip size | 4000 × 5000 $\mu$m$^2$ |
| resist sensitivity | 140-210 $\mu$C/cm$^2$ |
| dose | optimised |

| InGaAs Heterostructures (processed in Atsugi) | | | |
|---|---|---|---|
| | **process** | **product / machine** | **parameters** |
| **pre-etch** | pre clean | Aceton, Semico 23, $H_2O$ | 2/2/1 min ultrasonic |
| | etch I | $C_6H_8O_7$ (20%):$H_2O_2$(30%), 20:1 | 2 min |
| | stop | $H_2O$ | 60 s |
| | etch II | HCl:$H_3PO_4$:$CH_3COOH$:$H_2O$, 1:1:2.5:1 | 1 min |
| | stop | $H_2O$ | 60 s |
| **markers** | spin coat | Shipley S1813 | ca. 3 drps, 500/4000 rpm, 5/50 s |
| | bake | hotplate | 100°C, 3 min |
| | optical lithography | Mikasa Maskaligner MA-10 | 20 s |
| | develop | Shipley 352:$H_2O$ 1:5 | 50 s |
| | stop | $H_2O$ | 60 s |
| | clean | Argon RF-sputter | 10 W, $5 \cdot 10^{-3}$ Torr, 3 min |
| | deposition | Neva | 180 nm AuGeNi |
| | lift-off | Acetone, ultrasonic | 5 min |
| | rinse | Ethanol | spray and blow-dry |
| **nano** | spin coat | NTT-AT $\Phi$-MAC | ca. 3 drps, 500/6000 rpm, 5/50 s |
| | bake | oven | 170°C, 50 min |
| | e-beam lithograhy | Jeol JBX-6000FS | see previous table |
| | develop | MIBK:ECH, 2:1 | 60 s |
| | stop | ECH | 60 s |
| | postbake | hotplate | 115 °C, 5 min |
| | etch | Anelva L-510R-E, $BCl_3$ | 4 min |
| | profile | Tencor $\alpha$-step | |
| | rinse | Acetone, Ethanol | spray and blow-dry |
| **mesa** | spin coat | Shipley S1813 | ca. 3 drps, 500/4000 rpm, 5/50 s |
| | bake | hotplate | 100°C, 3 min |
| | optical lithography | Mikasa Maskaligner MA-10 | 20 s |
| | develop | Shipley 352:$H_2O$ 1:5 | 50 s |
| | stop | $H_2O$ | 60 s |
| | clean | Argon RF-sputter | 10 W, $5 \cdot 10^{-3}$ Torr, 3min |
| | etch I | $C_6H_8O_7$ (20%):$H_2O_2$(30%), 20:1 | 1 min |
| | stop | $H_2O$ | 60 s |
| | etch II | HCl:$H_3PO_4$:$CH_3COOH$:$H_2O$, 1:1:2.5:1 | 1 min |
| | stop | $H_2O$ | 60 s |
| | lift-off | Acetone, ultrasonic | 5 min |
| | rinse | Ethanol | spray and blow-dry |

| | process | product / machine | parameters |
|---|---|---|---|
| **bondpads** | spin coat | Shipley S1813 | ca. 3 drps, 500/4000 rpm, 5/50 s |
| | bake | hotplate | 100°C, 3 min |
| | optical lithography | Mikasa Maskaligner MA-10 | 20 s |
| | develop | Shipley 352:$H_2O$ 1:5 | 50 s |
| | stop | $H_2O$ | 60 s |
| | clean | Argon RF-sputter | 10 W, $5{\cdot}10^{-3}$ Torr, 3 min |
| | deposition | Neva | 120/120 nm AuGeNi/Au |
| | lift-off | Acetone, ultrasonic | 5 min |
| | anneal | Ulvac RHL-P610CN | 275 °C, 1 min |
| | rinse | Ethanol | spray and blow-dry |
| **gate oxide** | ECR-CVD | Aftex 6000 ECR | 50 min /115 nm |
| **gate** | spin coat | Shipley S1813 | ca. 3 drps, 500/4000 rpm, 5/50 s |
| | bake | hotplate | 100°C, 3 min |
| | optical lithography | Mikasa Maskaligner MA-10 | 20 s |
| | develop | Shipley 352:$H_2O$ 1:5 | 50 s |
| | stop | $H_2O$ | 60 s |
| | clean | Argon RF-sputter | 10 W, $5{\cdot}10^{-3}$ Torr, 3 min |
| | deposition | Neva | 30/60 nm AuGeNi/Au |
| | lift-off | Acetone, ultrasonic | 5 min |
| | rinse | Ethanol | spray and blow-dry |
| **oxide etch** | spin coat | Shipley S1813 | ca. 3 drps, 500/4000 rpm, 5/50 s |
| | bake | hotplate | 100°C, 3 min |
| | optical lithography | Mikasa Maskaligner MA-10 | 20 s |
| | develop | Shipley 352:$H_2O$ 1:5 | 50 s |
| | stop | $H_2O$ | 60 s |
| | etch | SiO2 Samco RIE-10NR | $CHF_3$, 10 min |
| | rinse | Acetone, Ethanol | spray and blow-dry |

# B Fit software

Weak localisation recorded in low-field experiments is analysed according to the theory developed by Iordanskii, Lyanda-Geller, and Pikus (ILP) [Ior94]. To obtain objective and reproducible results, curve fitting is performed using the *FuncFit* function of the IGOR Pro 4.0 data analysis package. This minimizes $\chi^2 = \sum_i \left(\frac{y-y_i}{\sigma_i}\right)^2$ where $y$ is a fitted value for a given point, $y_i$ is the measured data value for the point and $\sigma_i$ is an estimate of the standard deviation for $y_i$. To perform this analysis, ILP theory must be included in the IGOR Pro 4.0 package. For reasons of speed, this is done with C code implemented via a so-called XOP. The relevant C code is presented here, whereby the standard XOP framework was omitted. It can easily be obtained from the XOP toolkit [Wav].

```
/* **********************************
 * *       global constants         **
 * ********************************** */
const double qe=1.60217733e-19;
const double Pi=3.14159265;
const double h=6.6260755e-34;
const double h\_bar=1.05457266e-34;
const double PsiFuncPrecision=1e-7;
const double SumFuncPrecision=1e-7;
const double pre\_factor=-6.165735924e-6;

/**********************************************************
 **The function PsiFunc() returns the psi-function value of**
 **the double value passed to it as an argument          **
 **********************************************************/
double PsiFunc(const double x, const double precision)
{
    register double sm = 0;
    register double lastsum;
    register double n = 1;

    do
    {
        lastsum = sm;
        sm += (x-1) / (n*(n+x-1));
        n++;
    } while(fabs(lastsum-sm) >= precision);
    return sm;
}


/**********************************************************
 ** The function AFunc() returns the value for a_n        **
 **********************************************************/
double AFunc(const double n,const double b_phi,const double b_s)
{
    return (n + 0.5 + b_phi + b_s);
}


/**********************************************************
 **********************************************************
 ** CorrLocFunc - WAL function according to Iordanski,    **
 ** Lyanda-Geller, Pikus for terms linear in k. Free      **
 ** parameters: Bphi, Bso, precision                      **
 **********************************************************
 **********************************************************/

/**********************************************************
 ** The function CorrSumFunc returns the sum in ILP theory **
 **********************************************************/
double CorrSumFunc(const double b_phi, const double b_s, const
                                              double precision)
{
    register double sm = 0;
    register double addvalue = 0;
    register double aN, aNp, aNm;
    register double a0 = AFunc(0, b_phi, b_s);
    register double n = 1;

    do
    {
        sm += addvalue;
        aN=a0+n;
        aNp=aN+1;
        aNm=aN-1;
        addvalue = (3/n) - (-1 + 3*aN*aN + (-2 - 4*n + 2*aN)
           *b_s)/((aN+b_s)*(aNm)*(aNp)-2*b_s*(aN*(2*n+1)-1));
        n++;
    } while(fabs(addvalue) >= precision);
    return sm;
}

/**********************************************************
 **The function CorrFFunc returns F function in ILP theory **
 **********************************************************/
double CorrFFunc(const double b_tr, const double b_phi, const
                           double b_s, const double precision)
{
    const double a0 = AFunc(0, b_phi, b_s);
    const double a1 = AFunc(1,b_phi, b_s);

    const double FirstTerms = PsiFunc(0.5+b_phi,PsiFuncPrecision)
          + 1/a0 +(2*a0+1+b_s)/(a1*(a0+b_s)-2*b_s)+2*log(b_tr);
    double Total = FirstTerms - CorrSumFunc(b_phi, b_s, precision);

    return (Total);
}

/**********************************************************
 **               main calling function                  **
 **********************************************************/
static int CorrLocFunc(
                        struct {
                                double Prec;
                                double B;
                                double B_s;
                                double B_phi;
                                double B_tr;
                                double result;
                                }* p
                        )
{
    p->result = pre_factor*(CorrFFunc(p->B_tr/p->B, p->B_phi/p->B,
                                         p->B_s/p->B, p->Prec));
    return 0;
}
```

# C Contributions and publications

## Conference Contributions

- Christopher Schierholz, Reinhard Kürsten, Guido Meier, Toru Matsuyama und Ulrich Merkt.
  *Schwache Lokalisierung und Antilokalisierung in p-Typ InAs Inversionsschichten*
  DPG-Frühjahrstagung
  Regensburg, Germany (2002).
- Christopher Schierholz, Reinhard Kürsten, Guido Meier, Toru Matsuyama and Ulrich Merkt.
  *Weak Localisation and Antilocalisation in the 2D Electron System on p-Type InAs*
  $275^{\text{th}}$ WE-Heraeus Seminar on "Hardware Concepts for Quantum Computing"
  Bad Honnef, Germany (2002).
- Christopher Schierholz, Reinhard Kürsten, Guido Meier, Toru Matsuyama and Ulrich Merkt.
  *Weak Localisation and Antilocalisation in the 2D electron system on p-Type InAs*
  NTT Summer Camp
  Hakone, Japan (2002).
- Christoph de Beer, Christopher Schierholz, Guido Meier, Toru Matsuyama und Ulrich Merkt.
  *Schwache Lokalisierung in zweidimensionalen InAs Elektronensystemen*
  DPG-Frühjahrstagung
  Dresden, Germany (2003).
- Christopher Schierholz, Guido Meier, Toru Matsuyama and Ulrich Merkt.
  *Weak Localization and Spin Splitting in Inversion Layers on p-type InAs*
  MS+S 2004
  Atsugi, Japan (2004).
- Christopher Schierholz, Toru Matsuyama, Ulrich Merkt, and Guido Meier.
  *Weak Localization and Spin Splitting in Inversion Layers on p-type InAs*
  DPG-Frühjahrstagung
  Berlin, Germany (2005).
- Sebastian von Oehsen, Christopher Schierholz, Guido Meier, Toru Matsuyama, and Ulrich Merkt.
  *Spin-Orbit Interaction in two- and one-dimensional InAs Heterostructures*
  DPG-Frühjahrstagung
  Berlin, Germany (2005).

## Publications

- Ch. Schierholz, R. Kürsten, G. Meier, T. Matsuyama, and U. Merkt.
  *Weak Localization and Antilocalization in the Two-Dimensional Electron System on p-Type InAs*
  phys. stat. sol. (b) **233**, 436 (2002).

- G. Meier, C. Pels, C. Schierholz, M. Steiner, and T. Matsuyama.
  *Tunable Magnetoresistance in InAs/Ferromagnet Hybrid Devices*
  Phase Transitions **76**, 459 (2003).

- Ch. Schierholz, T. Matsuyama, U. Merkt, and G. Meier.
  *Weak Localisation and Spin Splitting in Inversion Layers on p-type InAs*
  Phys. Rev. B **70**, 233311 (2004).

## Invited talk

- Ch. Schierholz
  *Transportmessungen zur Bestimmung der Spin-Bahn Wechselwirkung in InAs Systemen*
  Walter Schottky Institut, TU München, Germany (Nov. 2003).

# Bibliography

[Aha67] Y. Aharonov and L. Susskind. *Observability of the sign change of spinors under 2π rotations*. Phys. Rev. **158**, 1237 (1967).

[Al'81] B.L. Al'tshuler, A.G. Aronov, and B.Z. Spivak. *The Aaronov-Bohm effect in disordered conductors*. JETP Lett. **33**, 94 (1981).

[And82] T. Ando, A.B. Fowler, and F. Stern. *Electronic properties of two-dimensional systems*. Rev. Mod. Phys. **54**, 437 (1982).

[Aws02] D.D. Awschalom, M.E. Flatté, and N. Samarth. *Spintronics*. Scientific American 53 (June 2002).

[Baa04] P. Baars. *Transport and Microwave Properties of Nanostructured InAs/Nb Hybrid Devices*. Dissertation, Universität Hamburg, 2004. ISBN 3-86537-010-1.

[Bai88] M.N. Baibich, J.M. Broto, A. Fert, F. Nguyen Van Dau, F. Petroff, P. Etienne, G. Creuzet, A. Friederich, and J. Chazelas. *Giant Magnetoresistance of (001)Fe/(001)Cr Magnetic Superlattices*. Phys. Rev. Lett. **61**, 2472 (1988).

[Bal00] P. Ball. *Meet the spin doctors*. Nature **404**, 918 (2000).

[Ber84] G. Bergmann. *Weak localisation in thin films*. Phys. Rep. **107**, 1 (1984).

[Bin89] G. Binasch, P. Grünberg, F. Saurenbach, and W. Zinn. *Enhanced magnetoresistance in layered magnetic structures with antiferromagnetic interlayer exchange*. Phys. Rev. B **39**, 4828 (1989).

[Car88] M. Cardona, N.E. Christensen, and G. Fasol. *Relativistic band structure and spin-orbit splitting of zinc-blende-type semiconductors*. Phys. Rev. B **38**, 1806 (1988).

[Che93] G.L. Chen, J. Han, T.T. Huan, S. Datta, and D.B. Janes. *Observation of the interfacial-field-induced weak antilocalization in InAs quantum structures*. Phys. Rev. B **47**, 4084 (1993).

[Cor11] O.M. Corbino. *Elektromagnetische Effekte, die von der Verzerrung herrühren, welche ein Feld an der Bahn der Ionen in Metallen hervorbringt*. Phys. Z. **12**, 561 (1911).

[Ẓ04] I. Ẓutić, J. Fabian, and S. Das Sarma. *Spintronics: Fundamentals and applications*. Rev. Mod. Phys. **76**, 323 (2004).

[dAeS94] E.A. de Andrada e Silva, G.C. La Rocca, and F. Bassani. *Spin-split subbands and magneto-oscillations in III-V asymmetric heterostructures*. Phys. Rev. B **50**, 8523 (1994).

[dAeS97] E.A. de Andrada e Silva, G.C. La Rocca, and F. Bassani. *Spin-orbit splitting of electronic states in semiconductor asymmetric quantum wells*. Phys. Rev. B **55**, 16293 (1997).

[Das90] B. Das, S. Datta, and R. Reifenberger. *Zero-field spin splitting in a two-dimensional electron gas*. Phys. Rev. B **41**, 8278 (1990).

[Dat90] S. Datta and B. Das. *Electronic analog of the electro-optic modulator*. Appl. Phys. Lett. **56**, 665 (1990).

[Dat95] S. Datta. *Electron transport in mesoscopic systems*. Cambridge University Press (1995). ISBN 0-521-59943-1.

[dB03] Christoph de Beer. *Spin-Bahn Wechselwirkung in Indiumarsenid Heterostrukturen mit Backgates*. Diploma Thesis, University of Hamburg (2003).

[Dol86] G.J. Dolan, J.C. Licini, and D.J. Bishop. *Quantum Interference Effects in Lithium Ring Arrays*. Phys. Rev. Lett. **56**, 1493 (1986).

[Dre55] G. Dresselhaus. *Spin-orbit coupling effects in zink blende structures*. Phys. Rev. **100**, 580 (1955).

[Dre92] P.D. Dresselhaus, C.M.A. Papavassiliou, R.G. Wheeler, and R.N. Sacks. *Observation of spin precession in GaAs inversion layers using antilocalisation*. Phys. Rev. Lett. **68**, 106 (1992).

[Eng96] G. Engels. *Untersuchungen zur Spinaufspaltung zweidimensionaler Elektronengase in InGaAs/InP Heterostrukturen*. Dissertation, RWTH Aachen, ISSN 0944-2952, 1996.

[Eng97] G. Engels, J. Lange, Th. Schäpers, and H. Lüth. *Experimental and theoretical approach to spin splitting in modulation-doped* $In_xGa_{1-x}/InP$ *quantum wells for* $B \rightarrow 0$. Phys. Rev. B **55**, R1958 (1997).

[Fab99] J. Fabian and S. Das Sarma. *Spin relaxation of conduction electrons*. J. Vac. Sci. Technol. B **17**, 1708 (1999).

[Fie99] R. Fiederling, M. Keim, G. Reuscher, W. Ossau, G. Schmidt, A. Waag, and L.W. Molenkamp. *Injection and detection of a spin-polarized current in a light-emitting diode*. Nature **402**, 787 (1999).

[Gan03] S.D. Ganichev and W. Prettl. *Spin photocurrents in quantum wells*. J. Phys. C **15**, R935 (2003).

[Gan04] S.D. Ganichev, V.V. Bel'kov, L.E. Golub, E.L. Ivchenko, P. Schneider, S. Giglberger, J. Eroms, J. De Boeck, G. Borghs, W. Wegscheider, D. Weiss, and W. Prettl. *Experimental Separation of Rashba and Dresselhaus Spin Splittings in Semiconductor Quantum Wells*. Phys. Rev. Lett. **92**, 256601 (2004).

[Gru00] D. Grundler. *Large Rashba Splitting in InAs Quantum Wells due to Electron Wave Function Penetration into the Barrier Layers*. Phys. Rev. Lett. **84**, 6074 (2000).

[Ham99] P.R. Hammar, B.R. Bennett, M.J. Yang, and M. Johnson. *Observation of spin injection at a ferromagnet-semiconductor interface*. Phys. Rev. Lett. **83**, 203 (1999).

[Ham02] P.R. Hammar and M. Johnson. *Detection of spin-polarized electrons injected into a two-dimensional electron gas*. Phys. Rev. Lett. **88**, 66806 (2002).

[Han02] A.T. Hanbicki, B.T. Jonker, G. Itskos, G. Kioseoglou, and A. Petrou. *Efficient electrical spin injection from a magnetic metal/tunnel barrier contact into a semiconductor*. Appl. Phys. Lett. **80**, 1240 (2002).

[Hik80] S. Hikami, A.I. Larkin, and Y. Nagaoka. *Spin-orbit interaction and magnetoresistance in the two dimensional random system*. Prog. Theor. Phys. **63**, 707 (1980).

[Hu99] C.-M. Hu, J. Nitta, T. Akazaki, H. Takayanagi, J. Osaka, P. Pfeffer, and W. Zawadzki. *Zero-field spin splitting in an inverted* $In_0.53Ga_0.47As/In_0.52Al_0.48As$ *heterostructure: Band nonparabolicity influence and the subband dependence*. Phys. Rev. B **60**, 7736 (1999).

[Hu01] C.-M. Hu, J. Nitta, A. Jensen, J.B. Hansen, and H. Takayanagi. *Spin-polarized transport in a two-dimensional electron gas with interdigital-ferromagnetic contacts*. Phys. Rev. B **63**, 125333 (2001).

[Hu03] C.-M. Hu, C. Zehnder, Ch. Heyn, and D. Heitmann. *THz collective spin-flip excitation of a two-dimensional electron system*. Phys. Rev. B **67**, 201302 (2003).

[Iba99] H. Ibach and H. Lüth. *Festkörperphysik, 5. Auflage*. Springer (1999).

[Ior94] S.V. Iordanskii, Yu.B. Lyanda-Geller, and G.E. Pikus. *Weak localisation in quantum wells with spin-orbit interaction*. JETP Lett. **60**, 206 (1994).

[Kik98] J.M. Kikkawa and D.D. Awschalom. *Resonant spin amplification in n-type GaAs*. Phys. Rev. Lett. **80**, 4313 (1998).

[Kna96] W. Knap et al. *Weak antilocalization and spin precession in quantum wells*. Phys. Rev. B **53**, 3912 (1996).

[Kog02] T. Koga, J. Nitta, T. Akazaki, and H. Takayanagi. *Rashba Spin-Orbit Coupling Probed by the Weak Antilocalization Analysis in InAlAs/InGaAs/InAlAs Quantum Wells as a Function of Quantum Well Asymmetry*. Phys. Rev. Lett. **89**, 0468011 (2002).

[Kog04] T. Koga, J. Nitta, and M. v. Veenhuizen. *Ballistic Spin Interferometer using the Rashba effect*. Phys. Rev. B **70**, 161302 (2004).

[Kür02] Reinhard Kürsten. *Josephson Feldeffekttransistoren auf p-Typ InAs*. Dissertation, Universität Hamburg (2002). ISBN 3-89873-388-2.

[Kre98] O. Krebs, D. Rondi, J.L. Gentner, L. Goldstein, and P. Voisin. *Inversion Asymmetry in Heterostructures of Zinc-Blende Semiconductors: Interface and External Potential versus Bulk Effects*. Phys. Rev. Lett. **80**, 5770 (1998).

[Lam01] S. Lamari. *Rashba effect in inversion layers on p-type InAs MOSFET's*. Phys. Rev. B **64**, 245340 (2001).

[Löh04] Stephan Löhr. *Modulierte zweidimensionale Elektronengase und Spin-Bahn Wechselwirkung in InAs und GaAs Heterostrukturen*. Dissertation, Universität Hamburg, 2004. ISBN 3-86537-199-X.

[Lin05] Y. Lin, T. Koga, and J. Nitta. *Effect of an InP/$In_{0.53}Ga_{0.47}As$ interface on spin-orbit interaction in $In_{0.52}Al_{0.48}As$/$In_{0.53}Ga_{0.47}As$ heterostructures*. Phys. Rev. B **71**, 045328 (2005).

[Lom88] G. Lommer, F. Malcher, and U. Rössler. *Spin Splitting in Semiconductor Heterostructures for $B \to 0$*. Phys. Rev. Lett. **60**, 728 (1988).

[Luo88] J. Luo, H. Munekata, F.F. Fang, and P.J. Stiles. *Observation of the zero-field spin splitting of the ground electron subband in GaSb-InAs-GaSb quantum wells*. Phys. Rev. B **38**, 10142 (1988).

[Luo90] J. Luo, H. Munekata, F.F. Fang, and P.J. Stiles. *Effects of inversion asymmetry on electron energy band structures in GaSb/InAs/GaSb quantum wells*. Phys. Rev. B **41**, 7685 (1990).

[Mat94] T. Matsuyama. *Präparation und Charakterisierung von Nb/InAs(2DEG)/Nb-Kontakten, Dissertation, Universität Hamburg*. Shaker-Verlag, Aachen (1994).

[Mat00] T. Matsuyama, R. Kürsten, C. Meißner, and U. Merkt. *Rashba spin splitting in inversion layers on p-type bulk InAs*. Phys. Rev. B **61**, 15588 (2000).

[Mei02] G. Meier, T. Matsuyama, and U. Merkt. *Field-effect in InAs/Permalloy Hybrid Transistors*. Phys. Rev. B **65**, 125327 (2002).

[Mei04] F.E. Meijer, A.F. Morpurgo, M. Klapwijk, T. Koga, and J. Nitta. *Competition between spin-orbit interaction and Zeeman coupling in Rashba two-dimensional electron gases*. Phys. Rev. B **70**, 201307 (2004).

[Mer87] U. Merkt and S. Oelting. *Simple description of nonparabolic two-dimensional subbands*. Phys. Rev. B **35**, 2460 (1987).

[Min04] G.M. Minkov, A.V. Germanenko, O.E. Rut, A.A. Sherstobitov, L.E. Golub, B.N. Zvonkov, and M. Willander. *Weak antilocalization in quantum wells in tilted magnetic fields*. Phys. Rev. B **70**, 155323 (2004).

[Miy95] T. Miyazaki and N. Tezuka. *Giant magentic tunneling effect in Fe/Al2O3/Fe junction*. JMMM **139**, L231 (1995).

[Möl03] C.H. Möller, Ch. Heyn, and D. Grundler. *Spin splitting in narrow InAs quantum wells with $In_{0.75}Ga_{0.25}As$ barrier layers*. Appl. Phys. Lett. **83**, 2181 (2003).

[Moo65] Gordon Moore. *The experts look ahead: cramming more components onto integrated circuits*. Electronics **38**, Issue 8 (1965).

[Moo95] J.S. Moodera, L.R. Kinder, T.M. Wong, and R. Meservey. *Large magnetoresistance at room temperature in ferromagnetic thin film tunnel junctions*. Phys. Rev. Lett. **74**, 3273 (1995).

[Neh95] Jasper Nehls. *Feldeffekt an Inversionsschichten auf p-Typ InAs und an InAs/GaSb Quantentöpfen, Dissertation, Universität Hamburg*. Shaker-Verlag, Aachen (1995). ISBN 3-82651-441-6.

[Nit97] J. Nitta, T. Akazaki, H. Takayanagi, and T. Enoki. *Gate control of spin-orbit interaction in an inverted $In_{0.53}Ga_{0.47}As/In_{0.52}Al_{0.48}As$ heterostructure*. Phys. Rev. Lett. **78**, 1335 (1997).

[Nit99] J. Nitta, F.E. Meijer, and H. Takayanagi. *Spin-interference device*. Appl. Phys. Lett. **75**, 695 (1999).

[Nit02] J. Nitta, T. Koga, and H. Takayanagi. *Interference of Aharonov-Bohm ring structures affected by spin-orbit interaction*. Physica E **12**, 753 (2002).

[Ohn99] Y. Ohno, D.K. Young, B. Beschoten, F. Matsukura, H. Ohno, and D.D. Awschalom. *Electrical spin injection in a ferromagnetic semiconductor heterostructure*. Nature **402**, 790 (1999).

[Ole01] J.T. Olesberg, W.H. Lau, M.E. Flatté, C. Yu, E. Altunkaya, E.M. Shaw, T.C. Hasenberg, and Thomas F. Boggess. *Interface contributions to spin relaxation in a short-period InAs/GaSb superlattice*. Phys. Rev. B **64**, 201301 (2001).

[Pel03] Christian Pels. *Ferromagnetic Electrodes for Spin-Polarized Transport*. Dissertation, Universität Hamburg, 2003. ISBN 3-86537-072-1.

[Pik95] F.G. Pikus and G.E. Pikus. *Conduction band splitting and negative magnetoresistance in $A_3B_5$ heterostructures*. Phys. Rev. B **51**, 16928 (1995).

[Pri95] G. Prinz. *Spin-Polarized Transport*. Physics Today **48**, 58 (1995).

[Ram96] P. Ramvall, N. Carlsson, P. Omling, L. Samuelson, W. Seifert, M. Stolze, and Q. Wang. *$Ga_{0.25}In_{0.75}As$/InP quantum wells with extremely high and anisotropic two-dimensional electron gas mobilities*. Appl. Phys. Lett. **68**, 1111 (1996).

[Ras60] E.I. Rashba. Fiz. Tver. Tela (Sovjet Physics - solid state) **2**, 1224 (1960).

[Ras84] E.I. Rashba and Yu A. Bychkov. *Oscillatory effects and the magnetic susceptibility of carriers in inversion layers*. J. Phys. C **17**, 6039 (1984).

[Ras00] E.I. Rashba. *Theory of electrical spin injection: Tunnel contacts as a solution of the conductivity mismatch problem*. Phys. Rev. B **62**, R16267 (2000).

[Ric00] A. Richter, M. Koch, T. Matsuyama, Ch. Heyn, and U. Merkt. *Transport properties of modulation-doped InAs-inserted-channel $In_{0.75}Al_{0.25}As/In_{0.75}Ga_{0.25}As$ structures grown on GaAs substrates*. Appl. Phys. Lett. **77**, 3227 (2000).

[Rös89] U. Rössler, F. Malcher, and G. Lommer. *High magnetic fields in semiconductor physics II*, Vol. 87 of *Springer Series in Solid-State Sciences*, S. 376–385. Springer, Berlin, 1989.

[Sch90] F. Schwabl. *Quantenmechanik, 2.Auflage*. Springer (1990).

[Sch91] T. Schweizer, K. Köhler, W. Rothemund, and P. Ganser. *Highly anisotropic electron mobilities of GaAs/$In_{0.2}Ga_{0.8}As/Al_{0.3}Ga_{0.7}As$ inverted high electron mobility transistor structures*. Appl. Phys. Lett. **59**, 2736 (1991).

[Sch98] Th. Schäpers, G. Engels, J. Lange, Th. Klocke, M. Hollfelder, and H. Lüth. *Effect of the heterointerface on the spin splitting in modulation doped $In_xGa_{1-x}As$/InP quantum wells for $B \longrightarrow 0$*. J. Appl. Phys. **83**, 4324 (1998).

[Sch01] Christopher Schierholz. *Spinpolarisierter Transport in p-Typ Indiumarsenid*. Diploma Thesis, University of Hamburg (2001).

[Sch02] Ch. Schierholz, R. Kürsten, G. Meier, T. Matsuyama, and U. Merkt. *Weak Localisation and Antilocalisation in the Two-Dimensional Electron System on p-Type InAs*. phys. stat. sol. B **233**, 436 (2002).

[Sch04] Ch. Schierholz, T. Matsuyama, U. Merkt, and G. Meier. *Weak Localisation and Spin Splitting in Inversion Layers on p-Type InAs*. Phys. Rev. B **70** (2004).

[Shu30] L. Shubnikov and W.J. de Haas. *A new phenomenon in the change of resistance in a magnetic field of single crystals of bismuth*. Nature **126**, 500 (1930).

[Sys] Stanford Research Systems. SR830 Lock-In Amplifier - Operating Manual.

[Tim87] G. Timp, A.M. Chang, J.E. Cunningham, T.Y. Chang, P. Mankiewich, R. Behringer, and R.E. Howard. *Observation of the Aharonov-Bohm Effect for $\omega_c \tau < 1$*. Phys. Rev. Lett. **58**, 2814 (1987).

[vdW03] W.G. v. d. Wiel, Yu.V. Nazarov, S. De Franceschi, T. Fujisawa, J.M. Elzerman, E.W.G.M. Huizelingand, S. Tarucha, and L.P. Kouwenhoven. *Electromagnetic Aharonov-Bohm effect in a two-dimensional electron gas ring*. Phys. Rev. B **67**, 033307 (2003).

[Ver97] L. Vervoort, R. Ferreira, and P. Voisin. *Effects of interface asymmetry on hole subband degeneracies and spin-relaxation rates in quantum wells*. Phys. Rev. B **56**, 12744 (1997).

[Vog] P. Vogl et al. *nextnano3 - a simulation tool for 3D quantum nanodevices*. http://www.wsi.tum.de/nextnano3.

[Wav] WaveMetrics. *XOP-toolkit for IGOR Pro*.

[Win01] R. Winkler. *private communication*. (2001).

[Win04] R. Winkler. *Spin orientation and spin precession in inversion-asymmetric quasi-two-dimensional electron systems*. Phys. Rev. B **69**, 045317 (2004).

[Wol01] S.A. Wolf et al. *Spintronics: A Spin-Based Electronics Vision for the Future*. Science **294**, 1488 (2001).

[Zee97] P. Zeeman. Phil. Mag. **43**, 226 (1897).

[Zhu01] H.J. Zhu, M. Ramsteiner, H. Kostial, M. Wassermeier, H.-P. Schönherr, and K.H. Ploog. *Room-temperature spin injection from Fe into GaAs*. Phys. Rev. Lett. **87**, 016601 (2001).

# Acknowledgments

I would never have been able to complete this thesis without the effort of many people. I am very grateful for the assistance and support I received over the past three years. I wish to express my gratitude to all of the following:

* Prof. Dr. Ulrich Merkt for making this thesis possible, as well as for his constant guidance and encouragement.
* 新田 教授 (Prof. Dr. Junsaku Nitta) for giving me the possibility to work in his group at the NTT basic research laboratories and for his care in all respects during my stay in Japan. I also wish to thank him for being the second referee of this thesis.
* Prof. Dr. Detlef Heitmann for being the second referee of my disputation.
* Dr. habil. Guido Meier for his continuous support and excitement, for many good discussions, and for his pragmatic view of things.
* 松山 博士 (Dr. Toru Matsuyama) for his wonderful explanations and the patience to repeat them as many times as necessary for me to grasp the entire topic. 'Thank you' as well for many enthusiastic discussions, in which he widened my view past mere facts and emphasised the importance of 'the philosophy' that underlies everything.
* Prof. Dr. Yiping Lin for introducing me to processing and experiments at the NTT basic research labs, as well as for patient answers to my many questions.
* 高柳 教授 (Prof. Dr. Hideaki Takayanagi) for enabling my stay at the NTT basic research labs.
* 'My' diploma student Dipl.-Phys. Christoph de Beer, for a good collaboration and for surviving me as his supervisor - and, of course, for his novel technique of wafer cleavage.
* Dr. Christian Heyn and Dipl.-Ing. Sandra Schnüll for growing the InAs-HEMT with an ingrown backgate.
* Dipl.-Phys. Ditmar Schuster and Dipl.-Ing. Tobias Däbritz for their support with the $^3$He-$^4$He dilution cryostat, with experimental setups in general, and for their down-to-earth views of things.
* Dr. Leonid Golub for his introduction to the 'correct' analysis of weak antilocalisation.
* Dr. Roland Winkler and Dr. Saadi Lamari for providing calculated data of the p-type InAs single crystals.
* the 'Munich-guys' - Dipl.-Phys. Hans Hübl, Dr. Sebastian Gönnenwein, Dr. Tobias Graf, and Priv.-Doz. Dr. Martin Brandt for many interesting discussions as well as for a really good time in Bad Honnef and Munich.

∗ Alexander Thieme for his support in computing. I'm still impressed that re-defining one variable can accelerate a program by a factor of 200.

∗ Dipl.-Phys. René Eiselt for providing loads of 'behind the scenes' maintenance and for keeping our lab so shipshape, that I couldn't find a thing. Thanks too for the many cakes!

∗ Dr. Marcus Steiner for help and advice concerning my stay in Japan, for painful badminton sessions, and for our mutual belief in the potential of the spin-transistor.

∗ Dr. Christian Pels for his good nature, patience, moral support and many late-skates.

∗ Dipl.-Phys. Alexander van Staa for good music, good vibrations, and a great time in Scheeßel.

∗ Dipl.-Phys. Jan Scholtyssek for joint work with organic solvents and for finding the right moment to demonstrate his interruptible power supply. Many thanks to for help with 'long-distance printing'.

∗ Dr. Andreas Richter, Dr. Miriam Barthelmess, Dr. Peter Baars, Dr. Mark Ebel, Dr. Malte Kurfiss, Dr. Ralf Rauer, Dipl.-Phys. Sebastian von Oehsen, Dipl.-Phys. Christian Busch, Dipl.-Phys. Simon Albrecht, Dipl.-Phys. Christine Johnas, Dipl.-Phys. Christian Uhrich, Dipl.-Phys. Gerd Neuber, Dipl.-Phys. Markus Bolte, Dipl.-Päd. Malte Lieske, Jann Kruse, Mahdi Mahajeri, Gesche Nahrwold, and Leif Humbert for innumerous lab and non-lab conversations, games of dart, lunches, beers, etc.

∗ Dipl.-Phys. Nicolas Thillosen, Jeff Liu, Dipl.-Phys. Frank Deppe, Dr. Katsushi Hashimoto, Dr. Taro Eichler, Dr. Alexander Kasper, Dr. Serge Camou, Dr. Wilfred van der Wiel, Norio Kumada, Toshiyuki Kobayashi, Dr. Jan Johannsen, Dr. Tobias Bergsten, Dr. Kei Takahara, and Yayoi Narumi for many lunchtime and non-lunchtime conversations on and off physics at and away from the NTT basic research labs.

∗ Wolfgang Hatje, Klaus Ahrens, Jerzy Gancarz, and Thomas Finger as well as the staff of the electrical and mechanical workshops for design and maintenance of equipment. And a very big thank you for supplying vast amounts of liquid Helium (more than 5000 liters in the last three years).

∗ The secretaries Petra Roth, Heidrun Dold, Etsuko Maruyama, and Izumi Fukaya for all their effort.

∗ Groups N, H, W, and DS at the Institute of Applied Physics in Hamburg as well as the 物ピ (Spintronics) Group at the NTT basic research laboratories for their support and many good parties.

∗ The German Ministry of Research and Education (BMBF) for financial support via the "Verbundprojekt" 13N8283.

∗ last, but certainly not least, Joyce, my parents and my grandmother, and my friends for their love, patience and unlimited support at all times.